國立臺灣大學理學院大氣科學系

博士論文

Department of Atmospheric Sciences
College of Science
National Taiwan University
Doctoral Dissertation

多重尺度交互作用對於複雜地形午後雷暴極端降雨之影響

Multiscale Interactions Contributing to Orographic Extreme Rainfall in Afternoon Thunderstorms over Complex Terrain

繆炯恩

Jyong-En Miao

指導教授：楊明仁 博士、Kristen L. Rasmussen, Ph.D.

Advisors: Ming-Jen Yang, Ph.D., Kristen L. Rasmussen, Ph.D.

中華民國 114 年 7 月

July 2025

doi:10.6342/NTU202504233

Acknowledgments

終於走到這裡，完成了人生的一個階段性目標。首先，我要感謝我的指導教授楊明仁老師，感謝老師對獨立思考與研究能力的培養，並推薦我前往美國科羅拉多州立大學（CSU）進行訪問研究，拓展了我的學術視野。我也特別感謝共同指導教授 Prof. Kristen Rasmussen，每週與她的討論總讓我獲益良多。感謝她對我研究的支持，並鼓勵我參加 AMS 年會，讓我有機會在國際學術場合分享研究成果。誠摯感謝本論文的口試委員：郭鴻基老師、陳正平老師、游政谷老師、林沛練老師和 Prof. Michael Bell，感謝您們撥冗審閱我的論文並提出寶貴建議，協助我更加完善本研究。此外，也要感謝周仲島老師在早期對我研究方向的啟發與鼓勵。

我要感謝國豐與明昌助教在行政事務上的幫忙。感謝對流與降水實驗室過去與現在的成員。曜竹與日軒，懷念我們在疫情前攜手完成 TAHOPE 各項事務的日子；尚恩與九令在資料與設備管理上的協助；惠琪與鏡芸學姊在行政上的支援。也感謝昌鴻，與你聊天總能幫助我釋放壓力。Shout out to 其他實驗室的夥伴們：Tsubaki、宇泓和柏言，加油，接下來就換你們畢業了。

I am especially grateful to Prof. Kristen Rasmussen and Prof. Michael Bell for their guidance and support during my visit to CSU. I would also like to thank all the members of the Rasmussen research group. Special thanks to Hungjui for his encouragement and support. I am also grateful to my office mates: Daniel, Ines, Megan, and Zoe. Your company brought many moments of laughter and warmth to both research and daily life. Thank you to Mitchell for teaching me the rules of American football, and to Lexi for sharing delicious treats. I also appreciate Ivy and other colleagues who provided constructive feedback on my presentations.

doi:10.6342/NTU202504233

I am thankful as well for the friends I met at CSU. To the “CSU travel crew,” thank you—it meant a lot to have you all around while living abroad. I also fondly remember playing pickleball with Saturday Club members Taiga, Yihao, and Ruichen. Thank you to Laurie for introducing me to American culture, which enriched my visiting experience beyond academics.

I sincerely appreciate Dr. Wen-Chau Lee and Dr. Ting-Yu Cha at NCAR for their support and insightful research discussions. I am especially grateful for the opportunity to give a seminar at EOL and engage with NCAR scientists. I also thank the TAHOPE/PRECIP team for their perseverance in collecting observational data during the pandemic, as well as NCAR for providing the computational resources used for WRF simulations.

感謝國科會「千里馬計畫」的經費支持，讓我有機會能夠前往 CSU 進行約一年的訪問研究，開拓視野、深化合作。

最後，我要深深感謝我的家人，感謝你們一路以來的支持與理解，讓我能夠追求夢想。更要感謝我的女友毓萱，在我低潮與焦慮的時刻始終陪伴在旁，是妳的鼓勵與體貼讓我能撐過無數難熬的日子。這段旅程，謝謝妳一路同行。

doi:10.6342/NTU202504233

中文摘要

預測山區雷暴是一項極具挑戰性的工作，這是由於多種大氣過程之間的多尺度交互作用，包含太陽加熱、熱力驅動氣流、冷池作用、雲微物理過程與地形效應等。本論文旨在深化對午後雷暴於弱綜觀與強綜觀環境下，導致地形極端降雨之物理機制的理解。透過先進的雷達觀測與數值模擬，本研究針對兩個在台北盆地造成極端降雨的午後雷暴案例進行分析：一個為弱綜觀環境下的個案（2015 年 6 月 14 日），另一個則為強綜觀環境下的個案（2022 年 5 月 31 日）。

第二章 探討中層相對濕度如何影響弱綜觀午後雷暴的發展。以 2015 年 6 月 14 日個案為例，環境中層乾燥空氣增強了蒸發冷卻效應，使得冷池增強，進而增強低層輻合與垂直舉升。這些條件有利於形成較大的霰粒子與更強的高層潛熱釋放，導致對流系統的範圍與強度提升。對流上升氣流的內部區域受到周圍濕空氣包覆，使整體的逸入作用顯著降低。此外，台北盆地的“盆地限制效應（basin confinement effect）”進一步強化了低層輻合並促進對流發展。

第三章分析 TAHOPE/PRECIP IOP 2（2022 年 5 月 31 日）發生的強綜觀午後雷暴，使用資料包含雙偏極雷達觀測與多都卜勒風場反演。分析結果指出，ZDR 柱增寬、多重胞合併與後續上升氣流加強與強降水之間存在潛在關聯。寬廣的 ZDR 柱（超過 8 公里寬）可能可以作為判斷對流組織與降水劇烈程度的有用指標。

第四章 探討 TAHOPE/PRECIP IOP 2 個案中，濕絕對不穩定層（MAUL）之形成機制，並透過雲解析模式模擬分析其與地形降雨的關聯。模擬結果顯示，地形與西南季風交互作用顯著增強雪山山脈一帶的低層水氣通量輻合，且支持中尺度氣層舉升，進而促成深厚的 MAUL 形成。相較之下，移除地形的模擬中僅產生淺層、氣塊的抬升。MAUL 體積與下一小時降雨強度之間呈現正相關，顯示 MAUL 相關的診斷指標可能具備預測極端降水潛勢的應用潛力。

綜合而言，本研究結果指出，地形對午後雷暴演變的影響高度依賴於其所處的綜觀背景與熱力環境場。本論文強調，若欲改善短延時強降雨的預報與風險評估，應採納跨尺度的分析架構。

doi:10.6342/NTU202504233

關鍵字：午後雷雨、極端降雨、中尺度過程、雲微物理、地形效應

doi:10.6342/NTU202504233

Abstract

Predicting thunderstorms over mountainous regions is challenging due to the multiscale interactions of various atmospheric processes, including solar heating, thermally driven airflow, cold pool, cloud microphysics and topographic effect. This dissertation aims to enhance our understanding of the physical mechanisms leading to orographic extreme rainfall in afternoon thunderstorms (ATSs) under both weak and strong synoptic environments. Using novel radar observations and numerical experiments, this study investigates a weakly-forced ATS case (14 June 2015) and a strongly-forced ATS case (31 May 2022), both of which produced extreme rainfall over the Taipei Basin.

Chapter 2 explores how midlevel relative humidity may influence the evolution of weakly forced ATSs. In the 14 June 2015 case, drier midlevel conditions enhanced evaporative cooling, strengthened cold pool outflows, and promoted more pronounced low-level convergence and vertical lifting. These factors favor the formation of larger graupel particles and stronger latent heating aloft, resulting in broader and more intense convective systems. The inner portion of the updrafts was shielded by surrounding moist air, leading to a notable reduction in bulk entrainment rate. Terrain effects—particularly the "basin confinement" within the Taipei Basin—further contributed to sustained low-level convergence and enhanced convective development.

Chapter 3 investigates the strongly forced ATSs during the TAHOPE/PRECIP IOP 2 using polarimetric radar observations and multi-Doppler wind retrievals. The analysis suggests a potential link between the widening of ZDR columns, multiple cell mergers, and the intensification of updrafts and precipitation. Broad ZDR columns (exceeding 8

doi:10.6342/NTU202504233

km) may serve as useful diagnostics for identifying convective organization and storm severity in complex terrain.

Chapter 4 focuses on the formation of moist absolutely unstable layers (MAULs) in relation to orographic rainfall, based on simulations of the same IOP 2 event. Terrain interactions with southwesterly monsoonal flow enhanced low-level moisture flux convergence along the Snow Mountain Range, supporting mesoscale layer lifting and the development of deep MAULs. In contrast, terrain-removed simulations exhibited shallower, parcel-based ascent with limited instability. A positive correlation was found between MAUL volume and next-hour rainfall, suggesting that MAUL-related diagnostics could be explored further as indicators of extreme precipitation potential.

Together, these findings demonstrate that topographic effects on ATSs are highly sensitive to the background synoptic and thermodynamic environments. The work emphasizes the need for multiscale frameworks to improve forecasting and risk assessment of short-duration extreme rainfall in mountainous regions.

KEYWORDS: Afternoon thunderstorms, Extreme rainfall, Mesoscale processes, Cloud microphysics, Orographic effects

doi:10.6342/NTU202504233

Table of Contents

doi:10.6342/NTU202504233

doi:10.6342/NTU202504233

doi:10.6342/NTU202504233

List of Figures

doi:10.6342/NTU202504233

doi:10.6342/NTU202504233

doi:10.6342/NTU202504233

doi:10.6342/NTU202504233

doi:10.6342/NTU202504233

doi:10.6342/NTU202504233

doi:10.6342/NTU202504233

doi:10.6342/NTU202504233

doi:10.6342/NTU202504233

doi:10.6342/NTU202504233

doi:10.6342/NTU202504233

List of Tables

doi:10.6342/NTU202504233

doi:10.6342/NTU202504233

Chapter 1 Introduction

The Taipei Basin, the most populous and economically significant region in Taiwan, experiences a strong influence from afternoon thunderstorms (ATSs) during the warm season (Chen et al. 2007). The Taipei metropolitan area often faces severe property damage and traffic hazards due to flash flooding and lightning associated with intense ATSs. Additionally, ATSs in Taiwan pose risks to people visiting mountainous areas and streams during the summer. A sudden rise in water level can result in incidents such as being stranded or swept away by fast currents, leading to the loss of human lives. Despite their significant impacts, forecasting ATSs remains challenging for meteorologists (Yang et al. 2024), in part due to our limited understanding of their underlying physical mechanisms and multiscale nature.

Predicting thunderstorms over mountainous regions is challenging due to the multiscale interactions of various atmospheric processes, including solar heating, thermally driven airflow, cloud microphysics, cold pools, and topographic effects (Houze 2012; Xu et al. 2012; Huang et al. 2019; Du et al. 2020; Morrison et al. 2020; Li et al. 2021; Chen et al. 2022). Nonlinear interactions between convective cells may increase the intensity of thunderstorms and the amount of rainfall (Westcott 1984; Tao and Simpson 1989; Glenn and Krueger 2017). Additionally, the terrain of Taiwan modifies the flow patterns and environmental characteristics, leading to variations in the location and intensity of precipitation (Miao and Yang 2020; Miao and Yang 2022; Cornejo et al. 2024). This complexity adds to the challenge of accurately predicting convection initiation, propagation, and intensification. Gaining a deeper understanding of the underlying physical mechanisms responsible for ATSs is essential for enhancing

doi:10.6342/NTU202504233

forecasting capabilities and implementing effective measures for disaster prevention.

Previous studies have focused on the roles of sea breeze and cold pool in the initiation and organization of weakly-forced ATS over Taipei Basin (Jou 1994; Chen et al. 2007; Lin et al. 2011; Jou et al. 2016; Miao and Yang 2018; Kuo and Wu 2019; Miao and Yang 2020; Wu et al. 2021; Chen and Wu 2025). Chen et al. (2007) indicated that sea breezes transport cooler, moist air into the Taipei Basin via the Danshui and Keelung River valleys. This sea air is subsequently warmed by the urbanized Taipei Basin and converges toward the southern mountains. Consequently, ATS is likely intensified by the warm and moist air downwind of the Taipei city. Using idealized simulations, Kuo and Wu (2019) verified the inference of Chen et al. (2007), and suggested that interactions between cold pools and sea breezes might play an important role in the northward propagation of convective system.

Using the high-resolution WRF simulation with the horizontal grid size nested down to 0.5 km, Miao and Yang (2018) proposed two physical mechanisms of cell mergers, highlighting the role of environmental winds, cold pools, and topography in the organization of thunderstorms. The first type of merger was the “rear-end collision” associated with different cell propagation speeds. After the convective cells reached the mature stage, the second type of merger was the “head-on collision” between the precipitation-induced outflows in the opposite direction (Tao and Simpson 1989). Miao and Yang (2020) found the convective cells at the mountain slope merged into the severe thunderstorm complex associated with the deep cold pool that was higher than the level of free convection (LFC) for the air parcels within the sea breeze. When the moist parcels within sea breeze were lifted up to the LFC at the leading edge of cold pool, conditional instability could be released effectively, leading to subsequent development of the ATS system. Furthermore, Miao and Yang (2020) suggested that

doi:10.6342/NTU202504233

evaporative cooling of raindrops played a major role in the northward propagation of cold pool and the production of heavy rainfall within the basin plain.

The thermodynamic environment also affects the storm's evolution and precipitation, but a smaller fraction of the literature has been devoted to the effects of the environmental moisture profile on weakly-forced ATS (Lin et al. 2012; Chen et al. 2016; Tsujino et al. 2021; Miao and Yang 2022). Previous ATS occurrence checklist (Lin et al. 2012; Chen et al. 2016) indicated that midlevel moist air was favorable for thunderstorm development in a weak synoptic environment, but the checklist did not perform well on the extreme rainfall case (14 June 2015) which resulted in urban-scale flooding. Using idealized experiments performed with the initial conditions based on the actual TS/NoTS soundings and with/without the southeasterly environmental flows, Tsujino et al. (2021) found that despite the different thermal profiles, the two simulations without the southeasterly flows show similar rainfall distribution and the evolution of the sea breeze. With the southeasterly winds, the simulation with the NoTS sounding exhibits less rainfall, suggesting both moisture and environmental wind profiles are critical to the ATS organization. The first part of this dissertation (Chapter 3; Miao and Yang 2022) conducted the numerical sensitivity experiments on midlevel (700–500-hPa) moisture and found that a dry layer at middle levels would result in stronger cold pool, more intense convection, more graupel particles, and a much larger area of the potential flooding region. Moreover, Miao and Yang (2022) indicated that Taipei Basin modulated the response of convection intensity to midlevel moisture (details in Chapter 3).

Only a limited number of observational studies have investigated the organization of convection and the associated precipitation processes in ATS systems over the Taipei Basin (e.g., Jung and Jou 2023). The second part of this dissertation focuses on these

doi:10.6342/NTU202504233

mechanisms. In general, the small number of studies stems from the difficulty of obtaining high-quality observations within ATS, especially over complex terrain. Thus, most of our current understanding is based on studies of thunderstorms in the U.S., most notably the Great Plains (e.g., Kumjian and Ryzhkov 2008; Picca and Ryzhkov 2012; Bodine and Rasmussen 2017; Van Den Broeke 2020), where environmental conditions and orographic characteristics differ significantly from those in Taiwan.

Polarimetric radars provide invaluable insights into the microphysics and kinematics of updrafts in convective systems. One key polarimetric feature is the (differential reflectivity) ZDR column, a ZDR-enhanced region extending above the environmental 0°C isotherm in the updraft area of severe storms (Illingworth et al. 1987; Bringi et al. 1997; Loney et al. 2002; Kumjian et al. 2014). It often contains low concentrations of large supercooled raindrops, ice crystals, graupel, and hail undergoing wet growth. Snyder et al. (2015) developed an algorithm that can identify and quantify ZDR columns in operational weather radar data, which could be helpful in evaluating convective storm evolution.

Another strength of polarimetric radars is the capability to detect changes in particle size, shape, orientation, and phase composition during various microphysical processes. Consequently, each microphysical process may leave a distinct polarimetric fingerprint that can be used to identify it (Kumjian et al. 2022). For instance, Kumjian and Ryzhkov (2012) proposed a framework to infer the dominant precipitation processes by examining the vertical gradient of ZH (radar reflectivity) and ZDR within the warm cloud layer. In the tropical DYNAMO/ARM-AMIE dataset of S-Pol observations, most of the convection cases reveal fingerprints for coalescence and evaporation while many stratiform cases reveal fingerprints for breakup, coalescence and evaporation (Kumjian and Prat 2014).

doi:10.6342/NTU202504233

The “Taiwan-Area Heavy rain Observation and Prediction Experiment” (TAHOPE 2022) field campaign was conducted from 25 May to 10 August 2022 to study the key ingredients and processes leading to extreme rainfall over complex terrain in Taiwan. TAHOPE is an international field campaign in collaboration with the Prediction of Rainfall Extremes Campaign In the Pacific (PRECIP 2022) from the U.S., and the Tropical cyclones-Pacific Asian Research Campaign for Improvement of Intensity estimations/forecasts (T-PARCII 2022) from Japan to have synergistic research observations. One of the primary scientific objectives of TAHOPE was to study the initiation, development and cloud-microphysical processes of ATSs that produce extreme precipitation over complex terrain. Complementary objectives from the PRECIP field campaign to study the key ingredients leading to heavy rainfall in a moisture-rich environment using an ingredients-based framework (Doswell et al. 1996) led to the deployment of the National Center for Atmospheric Research (NCAR) S-band dual-polarization Doppler radar (S-Pol) in Hsinchu, Taiwan (Fig. 1.1). These observations provide high-quality plan position indicator (PPI; horizontal scanning strategy) and range height indicator (RHI; vertical cross sections) scans of polarimetric observations in deep convection.

Observations alone are insufficient to identify the precipitation mechanisms addressed in this study. Numerical simulations—especially terrain sensitivity experiments—are necessary to evaluate orographic effects. These can be validated with observations and compared to uncover how orography modifies ATS precipitation, using full kinematic, thermodynamic, and microphysical fields.

Due to the complex terrain of the Taipei Basin, with the presence of Mt. Datun on the northern side and Linkou Plateau on the western side, and the Snow Mountain Range (SMR) on the eastern and southern sides (Fig. 1.2), the Taipei Basin serves as a

doi:10.6342/NTU202504233

natural laboratory for studying orographic control on deep convection. Miao and Yang (2020) investigated how the coastal terrain (i.e., Mt. Datun) impacted the convection development of ATSs under a weak synoptic environment. After removing Mt. Datun, the maximum rainfall decreased by 43%. The presence of Mt. Datun created a channel effect through the Danshui River Valley, intensifying the sea-breeze circulation and enhancing moisture transport. As a result, the modified sea-breeze circulation became more conducive for convection development, leading to a stronger ATS system in Taipei City. Wu et al. (2021) investigated the evolution of a heavy rainfall event on 19 August 2014 in northern Taiwan, and found that terrain confined the location of the heavy rainfall to the Taipei Basin (Miao and Yang 2022).

Previous studies have focused on the ingredients and mechanisms for extreme rainfall produced by weakly-forced ATSs. However, the manner in which mesoscale processes are modified depends on the thermodynamic and kinematic environment in which convection is embedded (Houze 2012, 2014). Given the difference of kinematic and thermodynamic environments between weakly and strongly forced ATS, mesoscale processes may vary accordingly. Rocque and Rasmussen (2022) investigated the impact of topography in different synoptic conditions over the South America and found that the impacts of terrain are different under weak and strong synoptic environment. Since frontal system provides mesoscale forcing mechanism and environment favorable for convection development (Chen et al. 2001) that are expected to affect the type of modification processes that occur. Thus, a comprehensive understanding of the ingredients and mechanisms for extreme rainfall produced by strongly-forced ATS is necessary.

This dissertation seeks to fill gaps in our understanding of the key ingredients and mechanisms driving extreme rainfall in both weakly and strongly forced ATSs, as well

doi:10.6342/NTU202504233

as the ways in which terrain influences the characteristics and development of associated precipitation processes. The strongly-forced ATS in TAHOPE/PRECIP IOP 2 (31 May 2022) serves as a case study and the results will be compared with previous studies on weakly-forced ATS. The goal of this dissertation is thus twofold:

1. A series of numerical simulations with the WRF Model are conducted to investigate the impacts of midlevel moisture content and terrain on the weakly-forced ATS case (14 June 2015). The first objective is to understand the physical processes leading to the intense ATS when a midlevel layer of dry air occurs. One control experiment and four sensitivity experiments using different environmental midlevel relative-humidity profiles are performed. The second objective is to examine how Taiwan terrain modulates the response of ATS to the midlevel moisture content. Three midlevel-moisture sensitivity experiments are conducted with Taiwan terrain totally removed.

2. The initiation, organization, and microphysical processes of the strongly-forced ATS during TAHOPE/PRECIP IOP 2 are investigated utilizing a unique combination of S-Pol radar observations and 3D winds retrieved by SAMURAI-TERRAIN (Cha and Bell 2023). Moreover, WRF simulations and terrain sensitivity experiments of the strongly-forced ATSs during TAHOPE/PRECIP IOP 2 will be employed to investigate the impacts of terrain on ATSs under strong synoptic environment.

This dissertation is organized as follows: Chapter 2 (Miao and Yang 2022) examines the impacts of midlevel moisture on the structure, evolution, and precipitation of the weakly-forced ATS using numerical experiments. Chapter 3 (Miao et al. 2025) employs polarimetric observations from S-Pol radar and multi-Doppler retrieved wind to investigate the initiation, organization, and microphysical processes of the strongly-forced ATS during TAHOPE/PRECIP IOP 2. Chapter 4 uses WRF simulations

doi:10.6342/NTU202504233

and terrain sensitivity experiments to examine the impact of terrain on the deep convection and heavy rainfall during TAHOPE/PRECIP IOP 2. Together, these chapters provide a comprehensive examination of the evolution and organization of ATSs under weak and strong synoptic environment. By elucidating the key ingredients and processes from both the observational and modeling perspective, this dissertation will contribute to understanding physical mechanisms which lead to extreme precipitation over complex terrain and improve our ability to predict severe weather. Chapter 5 summarizes the results of Chapters 2-4, discusses the overall conclusions, and provides areas of future research motivated by the results of this dissertation.

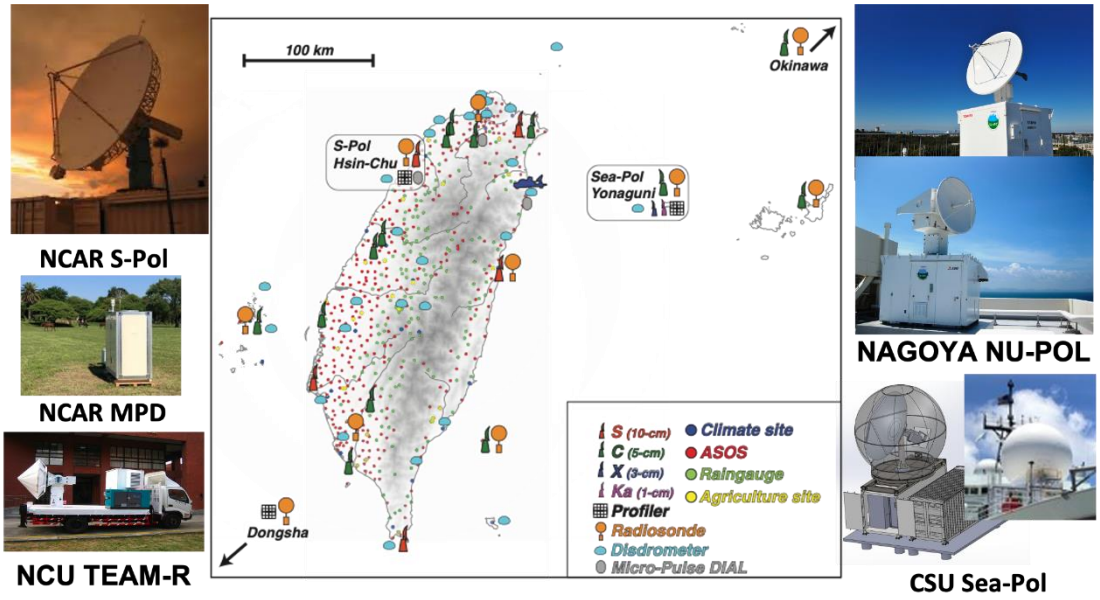

Figure 1.1. The map of observation networks of TAHOPE/PRECIP 2022. Source: http://precip.org/experiment-design/.

doi:10.6342/NTU202504233

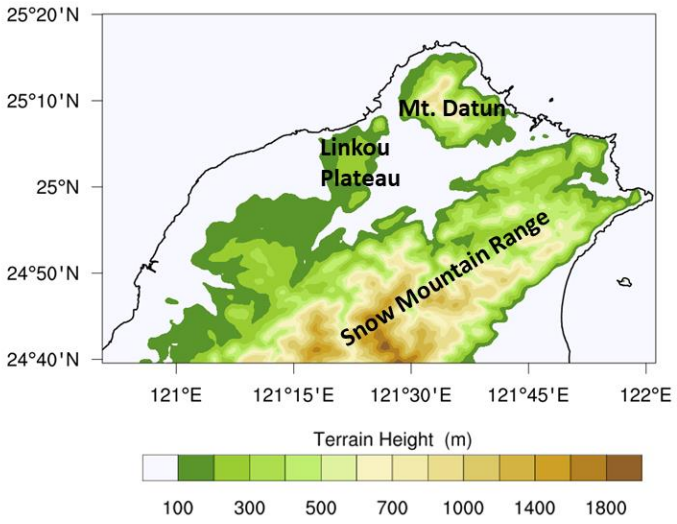

Figure 1.2. Taipei Basin domain with terrain elevations plotted (colored; in units of meter). Mt. Datun, Linkou Plateau and Snow Mountain Range are labeled.

doi:10.6342/NTU202504233

Chapter 2 Environmental and Orographic Control on Weakly-Forced ATSs

2.1 Background

Radar reflectivity climatology showed that thunderstorms in northern Taiwan often occur during 1500–1600 LST (Lin et al. 2011). When sea breeze collides with thunderstorm outflows near foothills south of TB, it can enhance lifting at the collision boundary. Therefore, ATSs are most active along the windward slopes of the mountains in Taiwan rather than at mountain peaks (Johnson and Bresch 1991; Jou 1994; Chen et al. 2001; Chen et al. 2007).

In Jou et al. (2016), observational characteristics of urban flash flood in TB associated with the ATS on 14 June 2015 were documented. They found that urban flooding associated with ATS was closely related to the merger of convective cells. The merger of convective cells produced an enlarged precipitation area and stronger radar echoes extending to much higher altitudes. Enhanced horizontal convergence produced by the sea-breeze circulation and cold-air outflow from earlier developed storms was favorable for cell merger. (Jou et al. 2016; Miao and Yang 2018).

Using the high-resolution WRF simulation with the horizontal grid size nested down to 0.5 km, Miao and Yang (2020; MY20 hereafter) investigated this severe ATS event. It was found that convection at the mountain peak (foothill) was initiated by the upslope wind (sea breeze). The convective cells at the mountain slope merged into the severe thunderstorm complex associated with the deep cold pool, which was higher than the level of free convection (LFC) for the air parcels within the sea breeze. When the

doi:10.6342/NTU202504233

moist parcels within sea breeze were lifted up to the LFC at the leading edge of cold pool, conditional instability could be released effectively, leading to subsequent development of the ATS system. Numerical sensitivity experiments indicated that cloud microphysics and coastal terrain also exerted considerable influences on the rainfall intensity for this ATS system.

However, besides low-level moisture brought by the sea breeze, Banchiao sounding at the TB for this ATS event also had deep dry air at middle levels (see Fig. 2.1c in MY20), which seemed to contradict the ATS occurrence checklist found in previous studies (Lin et al. 2012; Chen et al. 2016). It seems probable that the dry layer at middle levels would produce stronger evaporative cooling and cold pool, greater convergence at gust-front head, stronger convection, and more intense precipitation over the TB. Surprisingly, the sensitivity of ATS evolution and precipitation characteristics to the ambient mid-level moisture is not examined in previous studies on ATSs, which is the main theme of this study.

Although some studies have investigated the influences of mid-level dry air on convection development in the past, the detailed physical mechanisms remain underexplored. Many previous studies indicated that dry mid-level air is conducive to the formation of strong downdrafts (Fawbush and Miller 1954; Foster 1958; Browning and Ludlam 1962; Johns and Doswell 1992). Yang and Houze (1995) found that when the environmental moisture was reduced by half, the mesoscale downdraft was 22% stronger and the squall-line orientation became more upright. Gilmore and Wicker (1998) investigated the response of supercell morphology to the mid-tropospheric dryness. They found that supercells forming in environments with moderate vertical wind shear, large instability, and very dry mid-tropospheric air produced strong low-level outflow. James and Markowski (2010) found that dry air above the cloud base

doi:10.6342/NTU202504233

reduced the intensity of the quasi-linear convective systems and supercells, as measured by updraft mass flux and total condensation and rainfall. Moreover, the impact of dry air was highly sensitive to the environmental CAPE, with the deleterious effects of dry air on convection intensity being much lesser at higher CAPE. For tropical oceanic convection, the existence of environmental dry air above cloud base is considered to be detrimental to convection intensity (Brown and Zhang 1997; Parsons et al. 2000). Takemi et al. (2004) found that moisture profiles at mid-to-upper levels had a strong impact on the vertical development of tropical cumulus clouds. The mid-tropospheric moist layer was favorable for the development of cumulus congestus and cumulonimbus. These studies mostly used an idealized simulation to study convection in a horizontally homogeneous environment (i.e., a single thermodynamic profile). However, environmental heterogeneities can certainly influence convective systems (Richardson et al. 2007). Therefore, a real-case modeling study which represents these heterogeneities in the environment is still needed, especially for the complex terrain near the TB.

Following our previous research (Miao and Yang 2018; MY20) on this ATS system over the TB on 14 June 2015, a series of numerical simulations with the Weather Research and Forecasting (WRF) Model are conducted in this study to investigate the impacts of mid-level moisture content on the convection structure, storm evolution and precipitation intensity. The first objective is to understand the physical processes leading to the intense ATS when a mid-level layer of dry air occurs. One control experiment and four sensitivity experiments using different environmental mid-level relative-humidity profiles are performed. The second objective is to examine how Taiwan terrain modulates the response of ATS to the mid-level moisture content. Three mid-level-moisture sensitivity experiments are conducted with Taiwan terrain totally

doi:10.6342/NTU202504233

removed. The synoptic environment and the ATS occurrence for this severe thunderstorm case are described in section 2.2. Section 2.3 describes the model configuration and experimental design. The main results are presented in section 2.4. The response of ATS to mid-level moisture in the absence of Taiwan terrain is discussed in section 2.5. Discussion and summary are given in section 2.6.

2.2 ATS occurrence criteria revisited

Figure 2.1 displays the synoptic environment for the ATS system over the TB on 0000 UTC 14 June 2015. It is clear from Fig. 2.1a that the southerly wind prevailed over Taiwan ahead of a distant surface front, indicating that the synoptic forcing was weak. Southwesterly flow at 850-hPa level brought warm and moist air (with θ_e>340 K) from the South China Sea to Taiwan (Fig. 2.1b). On the other hand, the southwesterly wind prevailed over Taiwan at 700-hPa and 500-hPa levels (Fig. 2.1c,d). The ridge associated with the subtropical high-pressure system extended over the Bashi Channel and South China Sea (Fig. 2.1d). Meanwhile, the relative humidity (RH) near Taiwan was 40–50% at 700-hPa level and 20–40% at 500-hPa level, implying deep dry air at middle levels.

Backward trajectories over 48 hours were calculated for northern Taiwan (Fig. 2.2a) with the internet-based version of the Hybrid Single Particle Lagrangian Integrated Trajectory (HYSPLIT) model (Stein et al. 2015; Rolph et al. 2017) using the Global Data Assimilation System (GDAS) dataset with 0.5° latitude-longitude resolution. A total of 36 air parcels started from northern Taiwan, with initial heights of 5000 m ASL. The 48-h duration was selected to consider the synoptic-scale evolution appropriately. Figure 2.2 indicates that mid-level dry air parcels originated from the Philippine Sea

doi:10.6342/NTU202504233

and were transported by the anti-cyclonic flow at the vicinity of western North Pacific subtropical high.

The synoptic conditions for this case satisfy the criteria for ATS occurrence (Chen et al. 2016; C16 hereafter) except for the dewpoint depressions at surface (5.0 K in this case but 2.1 K in C16) and 500-hPa level (22.0 K in this case but 8.3 K in C16). Lin et al. (2012) also indicated that a moist mid-level environment was favorable for ATS development. However, there was deep mid-level dry air on this day (Fig. 2.1c,d). The dewpoint depressions at 700-hPa (10.9 K) and 500-hPa levels (22.0 K) were much larger than those in Lin et al. (2012) (9.5 K at 700 hPa and 11.0 K at 500 hPa). We hypothesize that the mid-level dry air between 700 and 500 hPa may play an important role in the development of this severe ATS event. Therefore, one control and four sensitivity experiments are conducted to explore the sensitivity of ATS development to the mid-level RH (see Table 2.1). Moreover, terrain sensitivity experiments are also conducted to examine the orographic effect.

doi:10.6342/NTU202504233

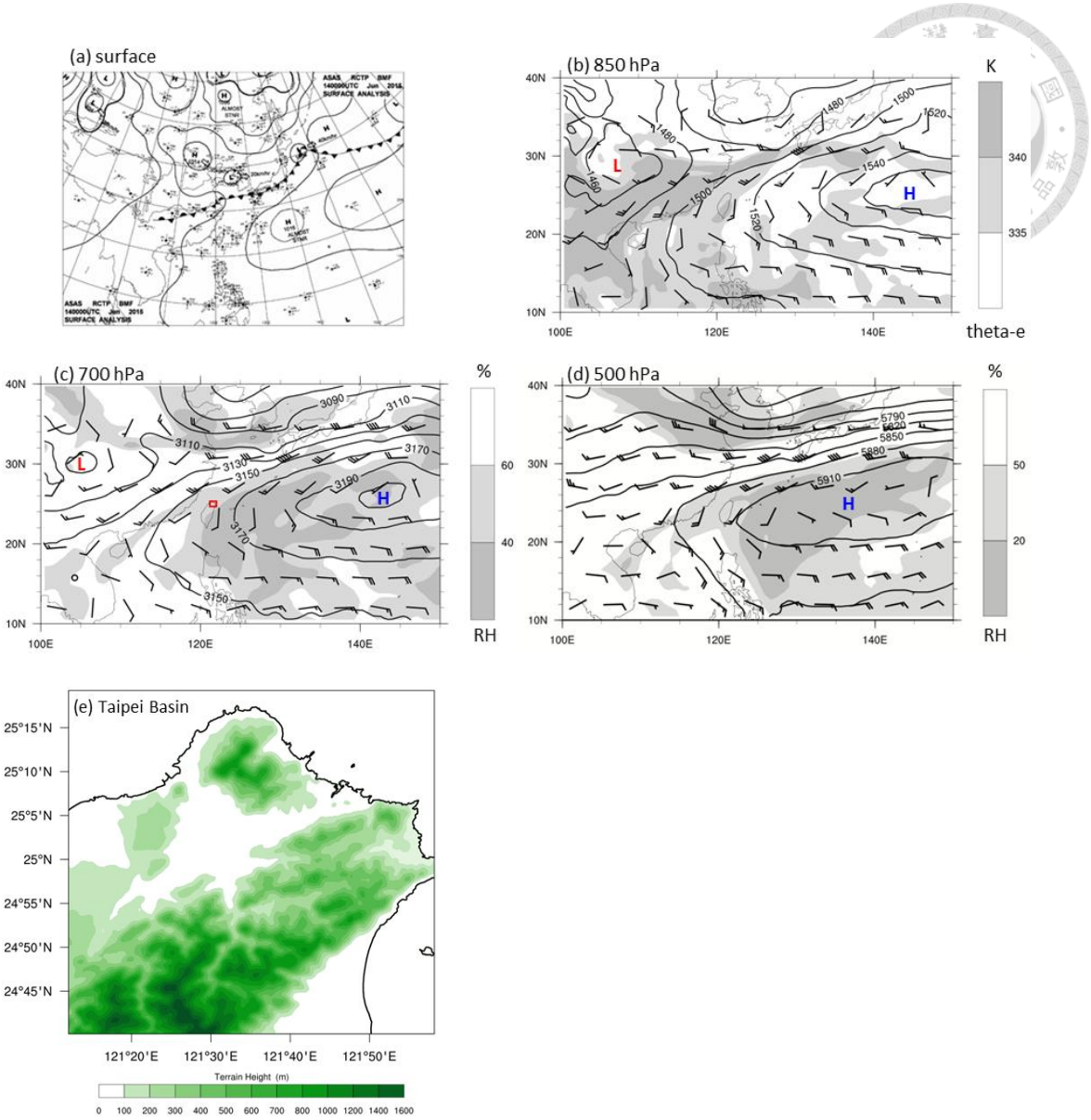

Figure 2.1. Synoptic condition at 0000 UTC (0800 LST) 14 June 2015: (a) CWB surface analysis map; (b) 850-hPa map from the ERA-Interim reanalysis with the geopotential height in contours, equivalent potential temperature in gray shading, and horizontal wind in wind barbs (full barb is 10 kts, and half barb is 5 kts); (c) 700-hPa map with the geopotential height in contours, relative humidity in gray shading, and horizontal wind in wind barbs; (d) same as (c) but for 500 hPa. (e) Taipei Basin domain with terrain elevations plotted (colored; in units of meter). Red box in (c) indicates the domain of Taipei Basin.

doi:10.6342/NTU202504233

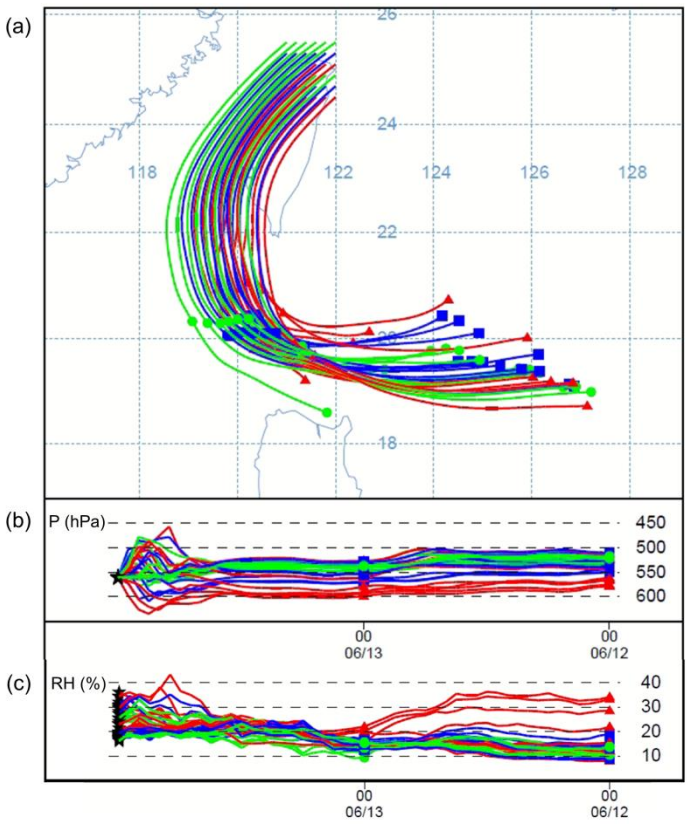

Figure 2.2. Backward trajectory analysis (for 48 hours): (a) horizontal trajectories; (b) pressure along the trajectories; (c) relative humidity along the trajectories. The starting (ending) time of backward trajectories is 00Z 14 June (00Z 12 June) 2015. Trajectories were initialized over northern Taiwan [121°E – 122°E; 24.5°N – 25.5°N] at 5 km ASL for a total of 36 trajectories.

Table 2.1. 700 and 500-hPa dewpoint depressions, 700–500 hPa mean relative humidity, downdraft convective available potential energy (DCAPE) and precipitable water (PW) for the observed and simulated Banchiao sounding at 0800 LST (0000 UTC) 14 June 2015 (t = 12 h). DCAPE values are based upon parcels descending from the 600 hPa. The location of Banchiao sounding station is shown in Fig. 2.2a in Miao and Yang (2020).

Experiment	500/700 hPa T–Td (K)	500–700 hPa mean RH (%)	DCAPE (J kg^{-1})	PW (mm)
OBS	22.0 / 10.9	27%	1518	44.7
DRY20	37.7 / 12.0	19%	1489	41.6
DRY10	27.8 / 10.4	27%	1318	43.6
CNTL	22.9 / 8.9	35%	1166	45.7
WET10	20.4 / 7.6	41%	1046	47.6
WET20	19.0 / 6.4	46%	949	49.4

doi:10.6342/NTU202504233

2.3 Numerical model and experimental design

2.3.1 WRF configuration

In MY20, the authors used the Advanced Research version of WRF to simulate the severe ATS event at TB on 14 June 2015. The simulation was compared with the surface and radar observations to show that the CNTL simulation can reasonably capture the evolution of sea breeze and ATS system over TB (see Figs. 5, 6, 8 in MY20). The simulated sounding was also compared to the one observed to illustrate that the thermodynamic environment was reproduced reasonably well by the CNTL run (see Fig. 4 in MY20). In this study, we use the same model configuration as MY20 to simulate the evolution of ATS, and the configuration is mentioned briefly here. The Advanced Research version of the Weather Research and Forecasting model (WRF-ARW version 3.4.1; Skamarock et al. 2008) is used to simulate this Taipei-basin ATS event from 1200 UTC 13 June to 1200 UTC 14 June 2015, with a forecast period of 24 h. Four nested domains with the horizontal grid sizes of 13.5, 4.5, 1.5 and 0.5 km are used, respectively (see Fig. 3 in MY20). Two-way interaction between inner and outer grids is considered. Fifty-five eta (η) levels are used in the vertical with higher resolution within the planetary boundary layer (eight layers below 1-km height). The model top is at 20 hPa, and the time step for the outermost domain is 5 seconds. The WRF model outputs at interval of 5 minutes are analyzed in this study.

The physical parameterization schemes used in the model include the Kain-Fritsch cumulus parameterization (Kain and Fritsch 1993), the WDM6 microphysics parameterization (Lim and Hong 2010), Rapid Radiative Transfer Model (RRTM) longwave radiation parameterization (Mlawer et al. 1997), Dudhia (1989) shortwave parameterization, and the Yonsei University (YSU) planetary boundary layer (PBL)

doi:10.6342/NTU202504233

parameterization (Hong and Pan 1996). Note that the cumulus scheme is used only in the outermost domain (with a horizontal grid size of 13.5 km), assuming that the grid sizes of other domains (with the grid sizes of 4.5, 1.5 and 0.5 km, respectively) are able to resolve convection explicitly. The initial and boundary conditions are from the ERA-Interim reanalysis dataset, updated every 6 hours with the latitude-longitude resolution at 0.75^{o} (Dee et al. 2011).

2.3.2 Sensitivity experiments on mid-level RH

In addition to the control simulation (CNTL), four numerical experiments are performed to examine the sensitivity of convective structure and evolution to the variations of mid-level RH. Experiments with RH higher (or lower) by 10% and 20% than that of CNTL at middle levels (700–500 hPa) are called the WET10 and WET20 (or DRY10 and DRY20), respectively. We modify the mid-level RH over the entire WRF domain for domain 1-4 (initial condition). The temperature profile is unchanged while the dew point is changed over 700–500 hPa levels. Moreover, the RH is also altered in the boundary condition. Note that if the RH is more (less) than 100% (0%) after adjustment, then it remains 100% (0%) to prevent physically unrealistic conditions in the moisture field. The rest of the model configurations are the same as those in CNTL.

The initial moisture vertical profiles, along with those 12 hours later, are illustrated in Fig. 2.3. For the initial conditions (t = 0 h; see Fig. 2.3a), the mid-level water vapor mixing ratio was increased (decreased) by a maximum of about 2.0 (1.5) g kg^{-1} in WET20 (DRY20) experiment compared to the CNTL. By t = 12 h (Fig. 2.3b), the mid-level dewpoint depressions had increased in all experiments, although the magnitude of the initial mixing ratio perturbations was maintained.

doi:10.6342/NTU202504233

Table 2.1 compares the 500-hPa and 700-hPa dewpoint depressions (T–Td), 700–500 hPa mean RH, downdraft convective available potential energy (DCAPE) and precipitable water (PW) for the Banchiao sounding at t = 12 h. The CNTL simulation reasonably captured the deep dry air at 700–500 hPa. A more detailed comparison of the simulated and observed sounding can be seen in MY20 (see their Fig. 4). Note that the observed sounding shows a decent DCAPE (1518 J kg^{-1}).

In these experiments, the percent increase in PW relative to the CNTL ranges from 4% in WET10 experiment to 8% in WET20 experiment, and the percent decrease in DCAPE relative to the CNTL ranges from 10% in WET10 experiment to 19% in WET20 experiment. On the other hand, the percent decrease in PW relative to the CNTL ranges from 5% in DRY10 experiment to 9% in DRY20 experiment, and the percent increase in DCAPE relative to the CNTL ranges from 13% in DRY10 experiment to 28% in DRY20 experiment.

MY20 indicated that CAPE at Banchiao station increased by a factor of four with abundant moisture transported by the sea breeze from 08 to 12 LST (see their Fig. 10), providing large convective instability for the development of the ATS. To examine the environment where the convection developed, we compared some thermodynamic variables at noon (Table 2.2), about 1 h before the ATS occurred within basin plain. Near-surface temperatures of all experiments are the same except for WET20. WET20 has the lowest near-surface temperature because the 850–800-hPa saturated layer in WET20 reduced solar radiation reaching the land surface. It is clear that CAPE differences between all experiments are quite minor except for WET20. For instance, CAPE in DRY20 is only 3% greater than that in CNTL run, and CAPE in WET10 is 2% less than that in CNTL. Note that CAPE in WET20 is 14% less than that in CNTL, mainly due to the lower near-surface temperature in WET20. Thus, perturbing the

doi:10.6342/NTU202504233

mid-level moisture has a minor influence on CAPE unless there is a saturated layer.

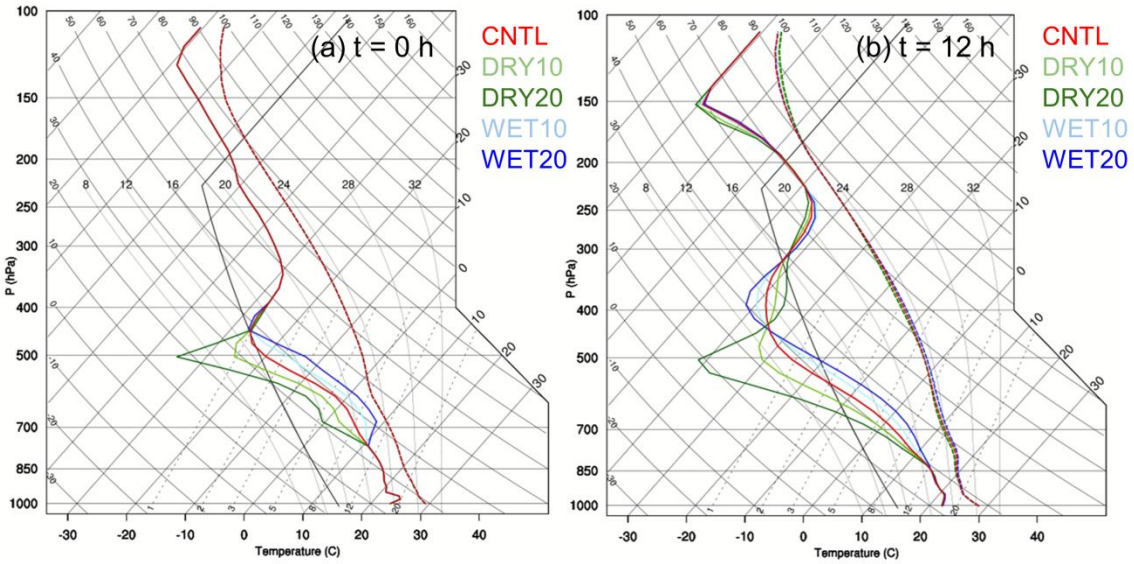

Figure 2.3. Simulated soundings of temperature and dew point from five experiments at Banchiao station at (a) t = 0 h and (b) t = 12 h.

Table 2.2. Temperature and water vapor mixing ratio at 35 m AGL (lowest eta level), CAPE and PW for the simulation experiments at 1205 LST 14 June 2015 (t = 16.08 h). Note that CAPE includes the virtual temperature effect.

Experiment	T_0 (°C)	q_0 (g kg^{-1})	CAPE (J kg^{-1})	PW (mm)
DRY20	32.0	17.4	3597	46.7
DRY10	32.0	17.6	3488	49.3
CNTL	32.0	17.6	3480	51.8
WET10	32.0	17.7	3421	54.6
WET20	31.6	17.8	2976	56.5

2.4 Results

2.4.1 Convection evolution and precipitation

Figure 2.4 displays the storm evolution in column-maximum radar reflectivity for five experiments. Overall, all experiments showed a similar pattern of three distinct

doi:10.6342/NTU202504233

phases in the life cycle of the ATS. The first phase was characterized by the scattered convection over the mountain slope south of TB (Fig. 2.4a-e). The scattered convection over the southern slope gradually merged into the thunderstorm complex during the second phase (Fig. 2.4f-j). Afterwards, the thunderstorm complex propagated to the central basin and produced intense rainfall in the third phase (Fig. 2.4k-o). Note that WET20 experiment showed the earliest convection initiation, followed by WET10, CNTL, DRY10 and DRY20 experiments, indicating a monotonic relation between the timing of convection initiation and mid-level moisture content. However, the ATS was stronger in CNTL, DRY10 and DRY20 experiments (Fig. 2.4f-j).

Previous studies (Kuang and Bretherton 2006; Khairoutdinov and Randall 2006) indicated that the widening of moist convection area could mitigate the detrimental effect of dry-air entrainment. To measure the convection area of the ATS system more objectively, we define the convection size as the maximum connected area of radar reflectivity and updraft intensity within the TB (see the black box with the size of 60 km by 45 km in Fig. 2.4a). Figure 2.5a shows the evolution of convection size in terms of the maximum connected area of column-maximum radar reflectivity greater than 55 dBZ. Overall, the convection size was larger in CNTL, DRY10 and DRY20 experiments, compared to that in WET10 and WET20 experiments, suggesting that the ATS system was wider in drier mid-level environments although DRY10 experiment had a slightly narrower size than CNTL. Figure 2.5b displays the convection size in terms of upper-level (8 km ASL) updraft velocity greater than 3 m s^{-1}. Similarly, the area of upper-level connected updraft was greater in experiments with drier mid-level environments (i.e., the CNTL, DRY10 and DRY20).

Figure 2.6a illustrates the increase of accumulated rainfall over the TB domain during 1200–1500 LST. WET20 experiment had the most accumulated rainfall; CNTL

doi:10.6342/NTU202504233

and WET10 runs featured similar accumulated rainfall; DRY10 and DRY20 had less accumulated rainfall than CNTL. Note that accumulated rainfall in DRY20 surpassed that in DRY10 after 1430 LST, indicating that the relationship between accumulated rainfall and environmental mid-level moisture content was nonlinear. Figure 2.6b displays the time series of the number of TB-domain grid points (N) with rainfall exceeding 40 mm in 30 min (i.e., rainfall intensity greater than 80 mm h^{-1}). The drainage standard of the rainwater sewers in Taipei City is 78.8 mm h^{-1} (Chen and Liu, 2014), indicating that Taipei's urban flooding will occur if the rainfall intensity surpasses the drainage standard. Therefore, Fig. 2.6b shows the sequence of potential flooding area (i.e., grid area × N) in Taipei City. Surprisingly, the total area of the potential flooding region during 1200–1500 LST was largest in DRY20 (N ~ 200 + 160 = 360), 20% more than that in CNTL (N ~ 80 + 220 = 300). DRY10 and WET10 experiments featured similar area of potential flooding region (N ~ 55), 82% less than that in CNTL. WET20 run had the least grid points (N ~ 15) for flooding potential, about 95% less than that in CNTL run. These results suggest that domain accumulated rainfall was not positively related to flooding potential (or rainfall rate). Furthermore, the occurrence of short-duration intense rainfall produced by the ATS system increased markedly with the decreased mid-level moisture. For instance, the area of region with rainfall intensity greater than 80 mm h^{-1} was approximately 95% greater in CNTL than that in the WET20 run, but the PW difference between the CNTL and WET20 was only 3.7 mm or 8% (see Table 2.1).

doi:10.6342/NTU202504233

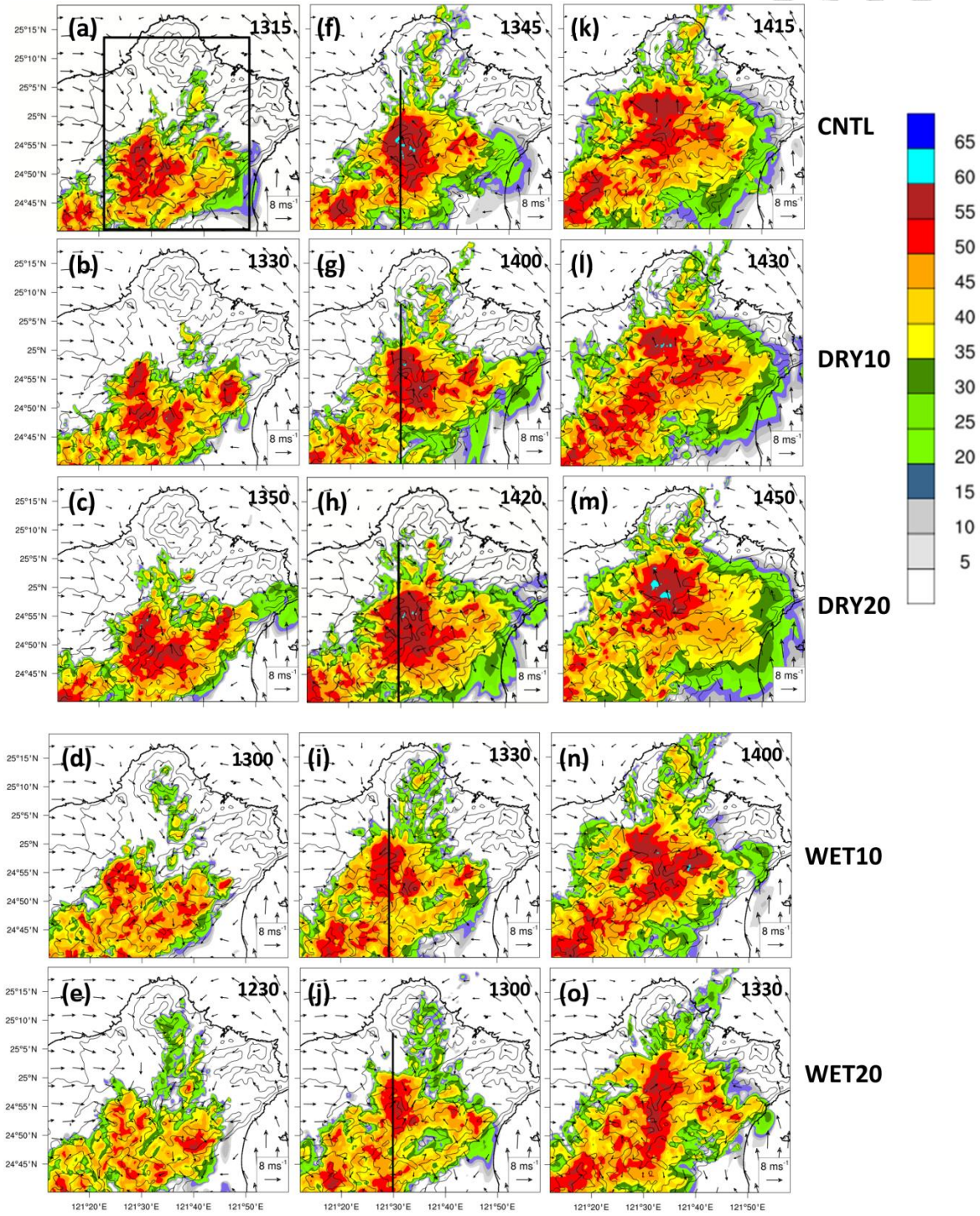

Figure 2.4. Simulated column-maximum radar reflectivity fields (in units of dBZ; colored) for the (a),(f),(k) CNTL, (b),(g),(l) DRY10, (c),(h),(m) DRY20, (d),(i),(n) WET10 and (e),(j),(o) WET20 experiments at (a)–(e) phase 1, (f)–(j) phase 2, and (k)–(o) phase 3. See the text for further explanation. The time in LST is indicated at the upper right corner in each panel. Black box in (a) is the TB domain for the calculations in Fig. 2.5–2.10, 2.15, 2.19–2.21 and Table 2.3. Black lines in (f)–(j) show the location of the vertical cross

doi:10.6342/NTU202504233

sections in Fig. 2.14.

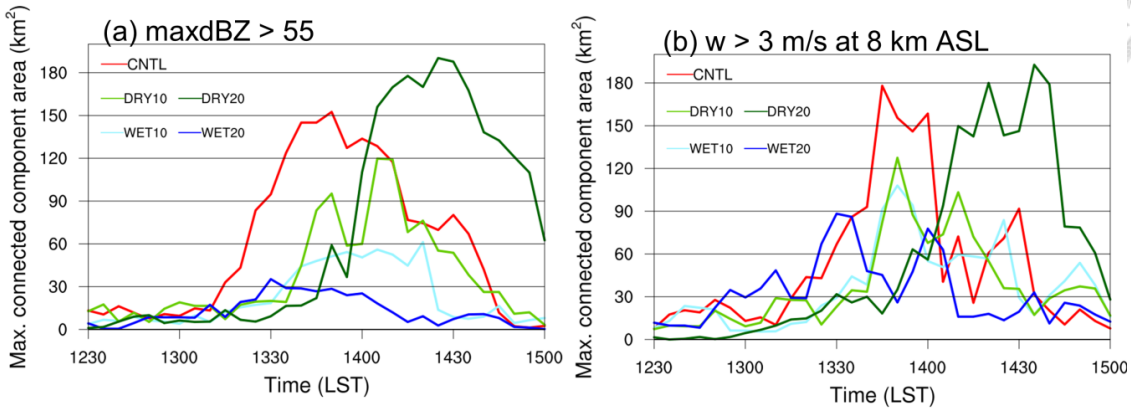

Figure 2.5. Time series of TB-domain maximum connected area (in units of km^2) of (a) column-maximum radar reflectivity greater than 55 dBZ and (b) vertical velocity greater than 3 m s^{-1} at 8 km ASL from the CNTL, DRY10, DRY20, WET10 and WET20 experiments. The TB domain is for the rectangular box in Fig. 4a.

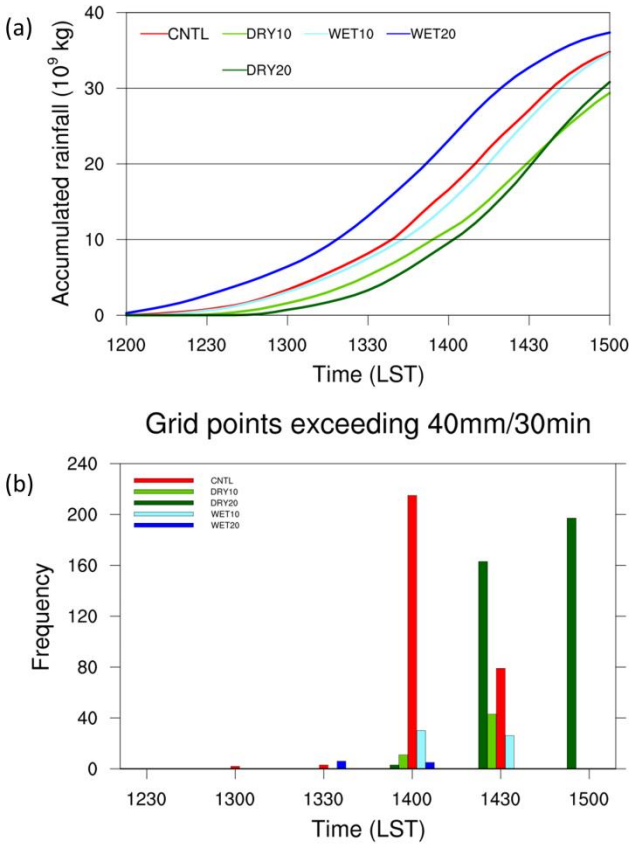

Figure 2.6. (a) Time series of TB domain-summed rainfall accumulation (in units of 10^9

doi:10.6342/NTU202504233

kg) for five experiments. (b) Number of TB-domain grid points with 30-min rainfall exceeding 40 mm (30 min^{-1}) for five experiments.

2.4.2 Evolution of updraft, downdraft and entrainment rate

Following James and Markowski (2010), updraft mass flux M_u and downdraft mass flux M_d are calculated with the formula, respectively,

$$M_u = \rho A_u W_u \quad (2.1)$$

$$M_d = \rho A_d W_d \quad (2.2)$$

where ρ is air density, A_u (A_d) is the area covered by updrafts (downdrafts), and W_u (W_d) is the vertical velocity averaged across all updrafts (downdrafts) in the TB domain. A grid point is defined as an updraft (downdraft) point if the vertical velocity is greater (less) than 0.5 m s^{-1} (–0.5 m s^{-1}) and the sum of the cloud water and cloud ice mixing ratios is greater than 0.01 g kg^{-1}. The local maxima of updraft mass flux were located near 4 km and 11 km ASL (Fig. 2.7), respectively. The 4-km maximum was associated with gust-front lifting, while the 11-km maximum was caused by buoyancy-driven ascent. The updraft mass flux was stronger in CNTL and DRY20 experiments, with the maxima near 10^9 kg s^{-1}. Moreover, the low-level updraft was stronger in CNTL, DRY10 and DRY20 experiments, compared to those in the WET10 and WET20 runs. On the other hand, DRY10 experiment had weaker upper-level updraft mass flux than that in the CNTL, which might be due to narrower convection size (Fig. 2.5) and more dilution by entrainment in DRY10 experiment (Fig. 2.9). Updraft mass flux in WET20 was the weakest among all five simulations.

The downdraft mass flux was stronger in CNTL and DRY20 experiments, with the maximum magnitude of 10^9 kg s^{-1} (Fig. 2.8). These results are consistent with the intense short-duration rainfall in these experiments (Fig. 2.6b). On the other hand, the

doi:10.6342/NTU202504233

downdraft mass fluxes of the DRY10 and WET10 experiments were comparable, whereas the WET20 downdraft mass flux was the weakest among the five experiments. Compared to CNTL, the maximum magnitude of downdraft mass flux in WET20 was weaker by about 30 %. Furthermore, the upper-level (9–15 km ASL) downdraft mass flux in WET20 was significantly weakened because of the reduced updraft mass flux (Fig. 2.7). Interestingly, WET20 experiment had the most accumulated rainfall within the TB (Fig. 2.6a) but the weakest downdraft mass flux and rainfall intensity (Fig. 2.6b). It suggests that the rainfall in WET20 was more spatially and temporarily homogeneous than that in the others.

Following Kurowski et al. (2018), the bulk entrainment rate ε is estimated as

$$\varepsilon = \frac{\frac{\partial \phi_c}{\partial z}}{\phi_e - \phi_c} \quad , \qquad (2.3)$$

where ϕ is moist static energy (MSE), which is approximately conserved during moist adiabatic process. Subscripts c and e denote the value within updrafts and environment, respectively. To emphasize the role of intense updrafts, the updraft MSE (ϕ_c) is calculated as an updraft-mass-flux weighted mean for the updrafts within the TB domain (Hohenegger and Bretherton, 2011). The environmental MSE (ϕ_e) is calculated by averaging all non-updraft grid points within the TB domain.

To elucidate the role of entrainment process, the evolution of TB-domain-mean bulk entrainment rate for all five experiments is shown in Fig. 2.9. During the period of shallow convection development (1200–1300 LST in the CNTL, DRY10 and DRY20), the entrainment rate was the largest (with the maximum value of 6×10^{-4} m^{-1}). With the intensification of updraft mass flux (Fig. 2.7), the entrainment rate was abruptly decreased to approximately 1×10^{-4} m^{-1} in CNTL, DRY10 and DRY20 experiments (see the dash ellipses in Fig. 2.9). The decrease of entrainment rate was associated with the

doi:10.6342/NTU202504233

increasing storm size (Fig. 2.5). In contrast, the entrainment rate did not decrease with the increasing updraft mass flux in WET10 and WET20 experiments. This implies that even in a drier mid-level environment, the entrainment effect could be reduced by wider convection area and thus higher maximum vertical velocity occurred (Fig. 2.10). Note that the entrainment rate began to increase after the increase of downdraft mass flux (Fig. 2.8), which might be due to the narrowing of convection area and the updraft/downdraft interaction.

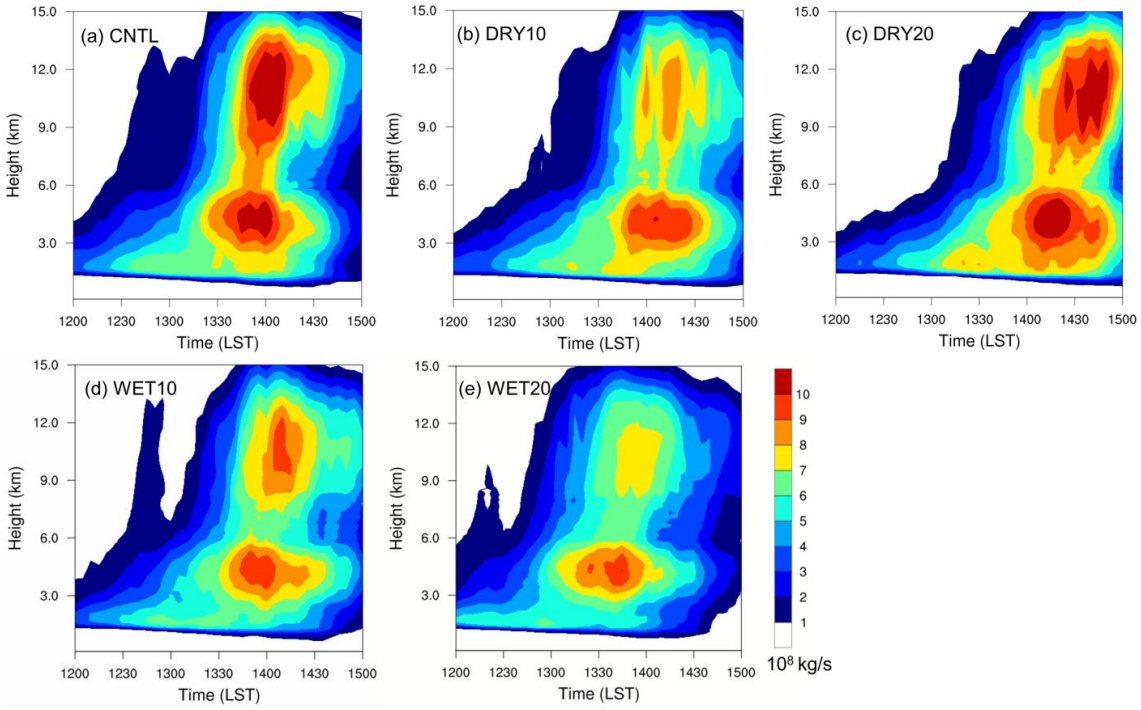

Figure 2.7. TB domain updraft mass flux (in units of 10^8 kg s^{-1}; colored) as a function of time and height for the five experiments.

doi:10.6342/NTU202504233

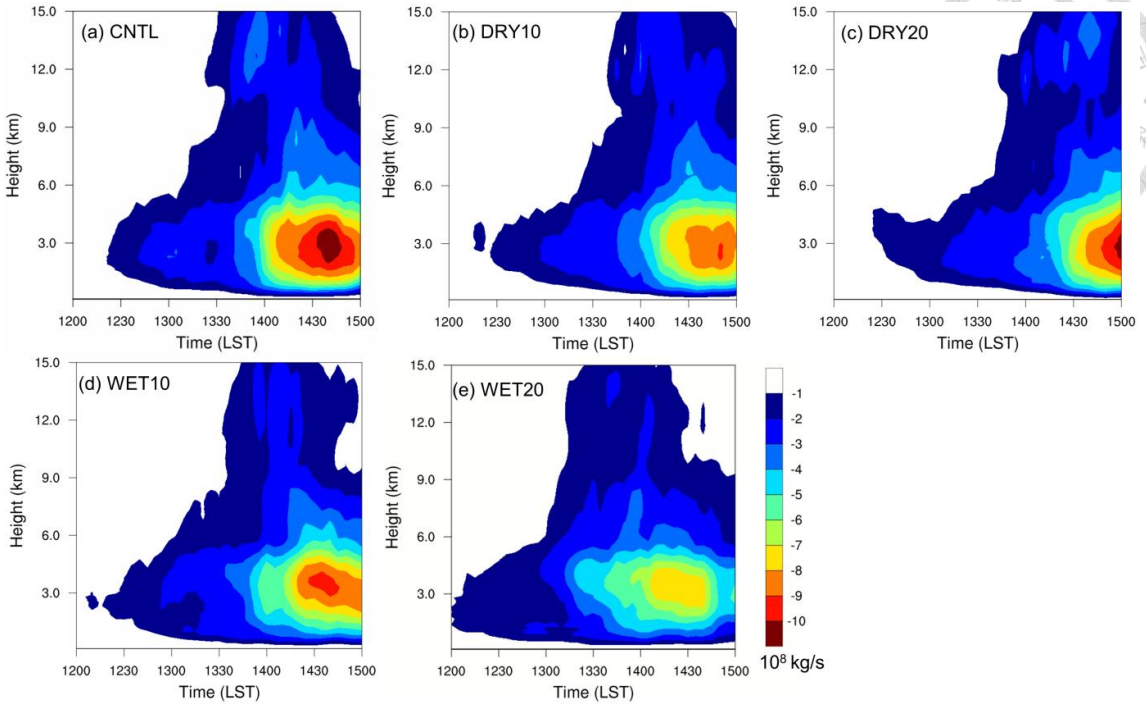

Figure 2.8. TB domain downdraft mass flux (in units of 10^8 kg s^{-1}; colored) as a function of time and height for the five experiments.

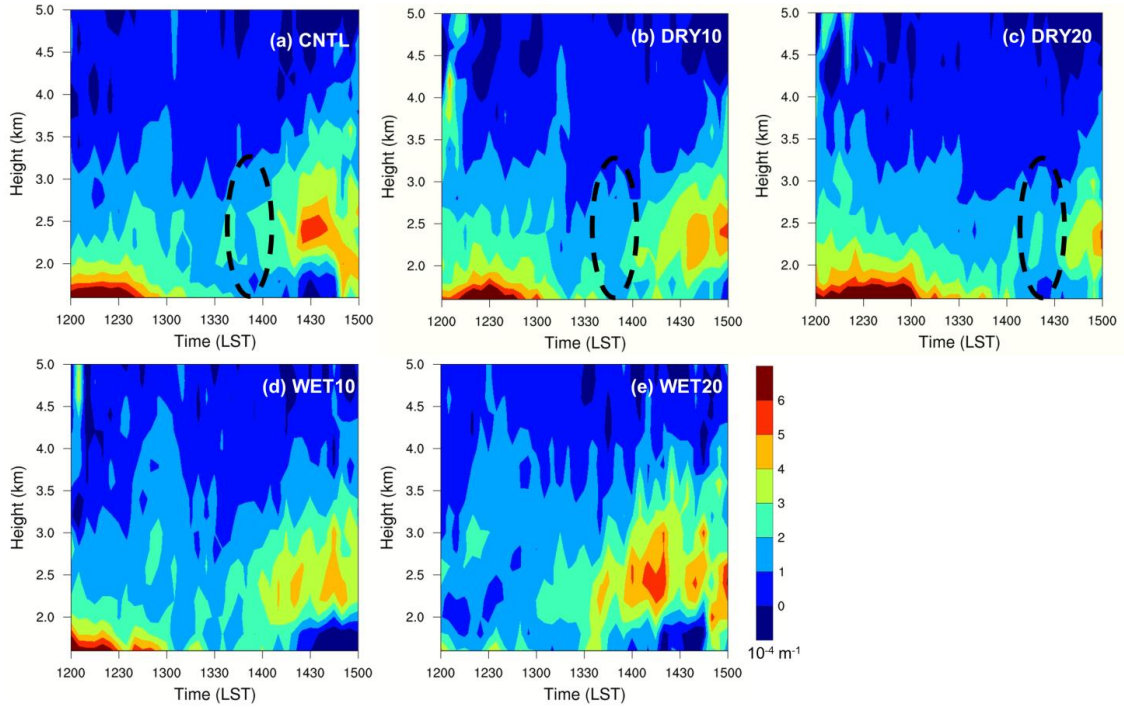

Figure 2.9. TB domain-mean bulk entrainment rate (in units of 10^{-4} m^{-1}; colored) as a function of time and height for the five experiments.

doi:10.6342/NTU202504233

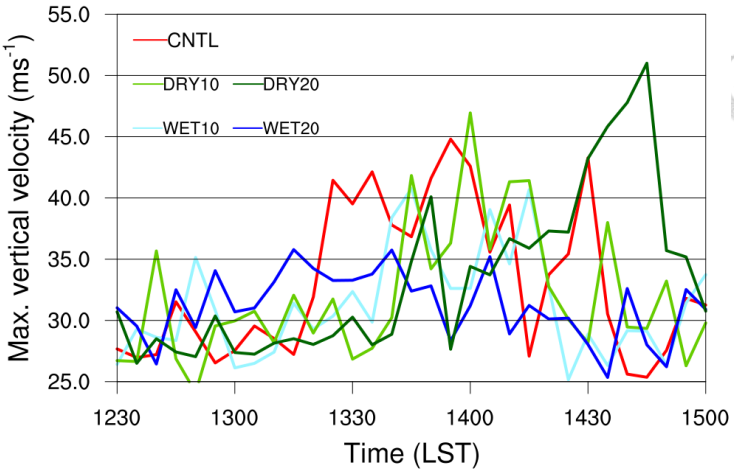

Figure 2.10. Time series of TB domain-maximum vertical velocity (in units of m s^{-1}) for the five experiments.

2.4.3 Cold pool and CAPE consumed

Previous research (e.g., Feng et al. 2015; Moseley et al. 2016) has shown that cold pool dynamics can play a critical role in the transition from shallow to deep convection. Following previous studies (Tompkins 2001; Feng et al. 2015; MY20), buoyancy b is calculated with the formula

$$b = g\frac{\theta_\rho - \overline{\theta_\rho}}{\overline{\theta_\rho}}, \qquad (2.4)$$

where g is the gravitational acceleration, and the overbar indicates the domain mean within the TB area. The density potential temperature θ_ρ (Emanuel 1994) is defined as

$$\theta_\rho = \theta(1 + 0.608q_v - q_l), \qquad (2.5)$$

where θ is the potential temperature, and q_v and q_l are the mixing ratios of water vapor and condensate (including liquid and ice phases), respectively. Cold-pool propagation speed C (Rotunno et al. 1988; Bryan and Parker 2010) is defined as

doi:10.6342/NTU202504233

$$C = \sqrt{-2\int_0^h \quad bdz}, \tag{2.6}$$

where b is the buoyancy in Eq. (2), and h is the depth of cold pool which is defined as the height at which b first exceeds –0.05 m s^{-2}. Note that cold pool intensity is proportional to its propagation speed C, as shown in Fig. 2.11. At first, the cold pools in CNTL, DRY10, and DRY20 were stronger and then merged together. After the cold pools merged, they became much stronger and had a larger connected area with stronger low-level updrafts. In contrast, cold pools in WET10 and WET20 were weaker and more discrete. Feng et al. (2015) suggested that more clouds were triggered at the collision boundary of cold pools, favoring the formation of wider clouds. These wider clouds would reduce the entrainment rate and develop into deep convection in a dry mid-level environment.

Trajectories for air parcels passing through the ATS systems in CNTL, DRY20 and WET20 experiments were used to examine the differences in simulated convective structures. Trajectories were calculated from 5-min model outputs for a total of 200 air parcels originating just north of the gust front before the ATSs propagated into central TB, with initial heights of 400 and 600 m ASL (Fig. 2.12). A perturbation of 200 m was added in the starting vertical level of air parcels to increase the trajectory spread. These 30-min forward trajectories were calculated and plotted using the VAPOR (Visualization and Analysis Platform for atmospheric, Oceanic and solar Research; Clyne and Rast 2005; Clyne et al. 2007) software. Thirty minutes after the release of the near-surface moist air parcels, most of the moist parcels from sea breeze in CNTL and DRY20 experiments were lifted along the leading edge of the deep cold pool (Fig. 2.12). A majority of these parcels in these experiments rose above the melting level (~5 km ASL), with the final heights more than 15 km ASL (Fig. 2.12c,f). Note that these trajectories had overshooting characteristics. In contrast, only a few parcels in WET20 experiment rose above the

doi:10.6342/NTU202504233

shallow cold pool (Fig. 2.12i), whereas many parcels remained trapped at lower levels. Furthermore, 63% and 91% of air parcels rose above the melting level (~5 km ASL) in CNTL and DRY20 experiments, respectively (Fig. 2.13). On the contrary, only 24% of parcels rose above the melting level in WET20 experiment. These results indicate that air parcels within sea-breeze circulation in CNTL and DRY20 runs were ‘‘lifted’’ to much higher levels than those in WET20 run. For this ATS system occurring in an environment with weak synoptic forcing, the percentage of surface-based parcels that rose in deep convection was proportional to the intensity of cold pool.

To shed more light on the effects of cold pool dynamics, the evolution of thermodynamic instability and cold-pool height before and after the simulated ATS systems propagated into the TB is shown in Fig. 2.14. Before the cold pool propagated into the TB, CAPEs over central Taipei reached more than 1500 J kg^{-1} (Fig. 2.14a,c,e,g,i) due to solar heating and moisture brought by the sea breeze (MY20). The updraft (1 m s^{-1}) associated with the gust front extended from surface to 5-km height in CNTL, DRY10 and DRY20 experiments. Afterwards, the passage of stronger cold pools in CNTL, DRY10 and DRY20 experiments resulted in a dramatic release of CAPE, as indicated by the CAPE decrease to less than 500 J kg^{-1} (Fig. 2.14b,d,f). In contrast, CAPEs over central Taipei in WET10 and WET20 experiments remained relatively high even after the passage of their weaker cold pools (Fig. 2.14h,j). If the initial mid-level RH in the CNTL increased by 20% (i.e., WET20 experiment), then the cold-pool depth (speed) decreased by 50% (21%), and the CAPE release rate decreased by 81% (Table 2.3). Figure 2.15 displays that DRY20 experiment had the most latent heating in the upper level, followed by CNTL, DRY10, WET10 and WET20. These results imply that the cold pools in wetter mid-level environments (i.e., WET10 and WET20) were too weak to lift the moist air

doi:10.6342/NTU202504233

parcels within sea breeze. As a result, CAPEs over the TB could not be released effectively.

The simulation results indicate that the response of convection to mid-level RH is somewhat nonlinear. Cold pool and entrainment process exert positive and negative influences on convection intensity, respectively. On one hand, the cold-pool intensity and hence the positive effect on convection were similar between CNTL and DRY10 runs (see C and $dCAPE_{0\text{-}1km}/dt$ in Table 2.3). On the other hand, drier air aloft in DRY10 produced stronger entrainment (negative effect) (see ε in Table 2.3), associated with the reduction in convection size (Fig. 2.5). Therefore, the convective updraft in DRY10 was more prone to the detrimental effect of dry-air entrainment than that in CNTL, and thus convection in DRY10 was weaker than that in CNTL. In other words, the nonlinear response of convection intensity to mid-level RH results from the compensating effects between cold-pool intensity and entrainment process. Note that DRY10 and CNTL experiments featured similar cold pool intensity because the reduction in mixing ratio offset the enhancement in evaporative cooling in DRY10 (Table 2.3).

doi:10.6342/NTU202504233

Table 2.3. TB domain 1-h averaged cold-pool variables [near-surface (35 m) buoyancy b, height h, propagation speed C], the rate of change of 0–1 km CAPE $dCAPE_{0\text{-}1km}/dt$, rainwater mixing ratio q_r, evaporative cooling of rainwater $cool_{evp}$, and entrainment rate ε during the time period when the ATS system moved into the TB [i.e., from Phase 2 (Fig. 2.4f-j) to Phase 3 (Fig. 2.4k-o)]. "0–1 km CAPE" is defined as the vertically integrated CAPE from the surface to 1 km ASL. q_r and $cool_{evp}$ are averaged over 0–6 km ASL. ε is averaged over 1.5–3 km ASL.

Experiment	DRY20	DRY10	CNTL	WET10	WET20
b ($m\ s^{-2}$)	–0.065	–0.059	–0.057	–0.044	–0.040
h (m)	388	348	304	196	152
C ($m\ s^{-1}$)	9.0	8.1	8.1	6.6	6.4
$dCAPE_{0\text{-}1km}/dt$ ($J\ m^{-2}\ h^{-1}$)	–0.33	–0.27	–0.26	–0.16	–0.05
q_r ($g\ kg^{-1}$)	0.51	0.43	0.45	0.37	0.31
$cool_{evp}$ ($K\ h^{-1}$)	2.1	1.8	1.7	1.3	1.0
ε ($10^{-4}\ m^{-1}$)	1.8	2.1	1.8	1.9	1.7

doi:10.6342/NTU202504233

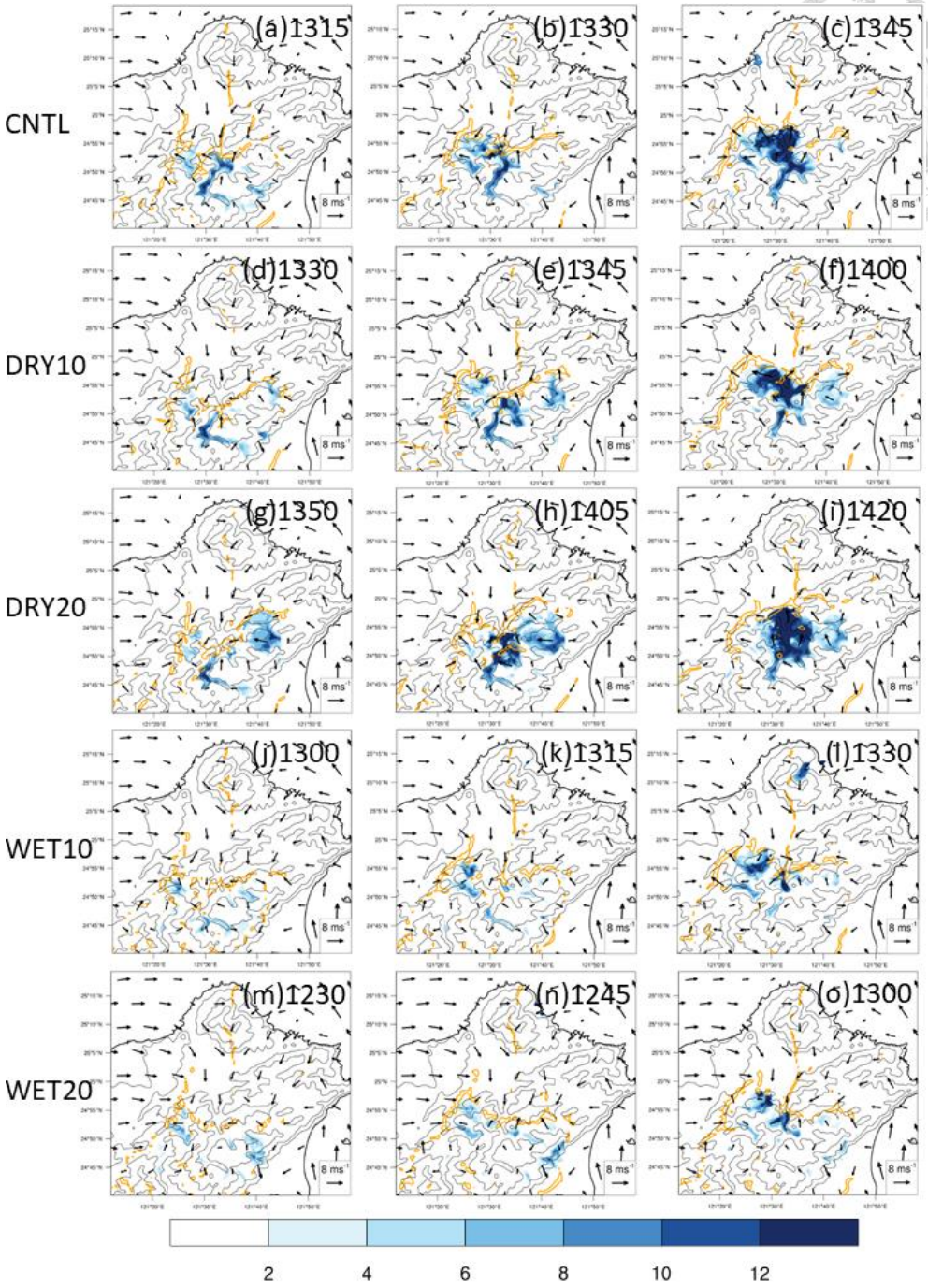

Figure 2.11. Horizontal cross sections of cold-pool propagation speed (colored; in units of m s^{-1}), 560-m vertical velocity (orange contoured; 2 m s^{-1}), and 10-m wind vectors from all experiments. Black line is for the terrain height contoured at 100, 300, 700, and 1300 m.

doi:10.6342/NTU202504233

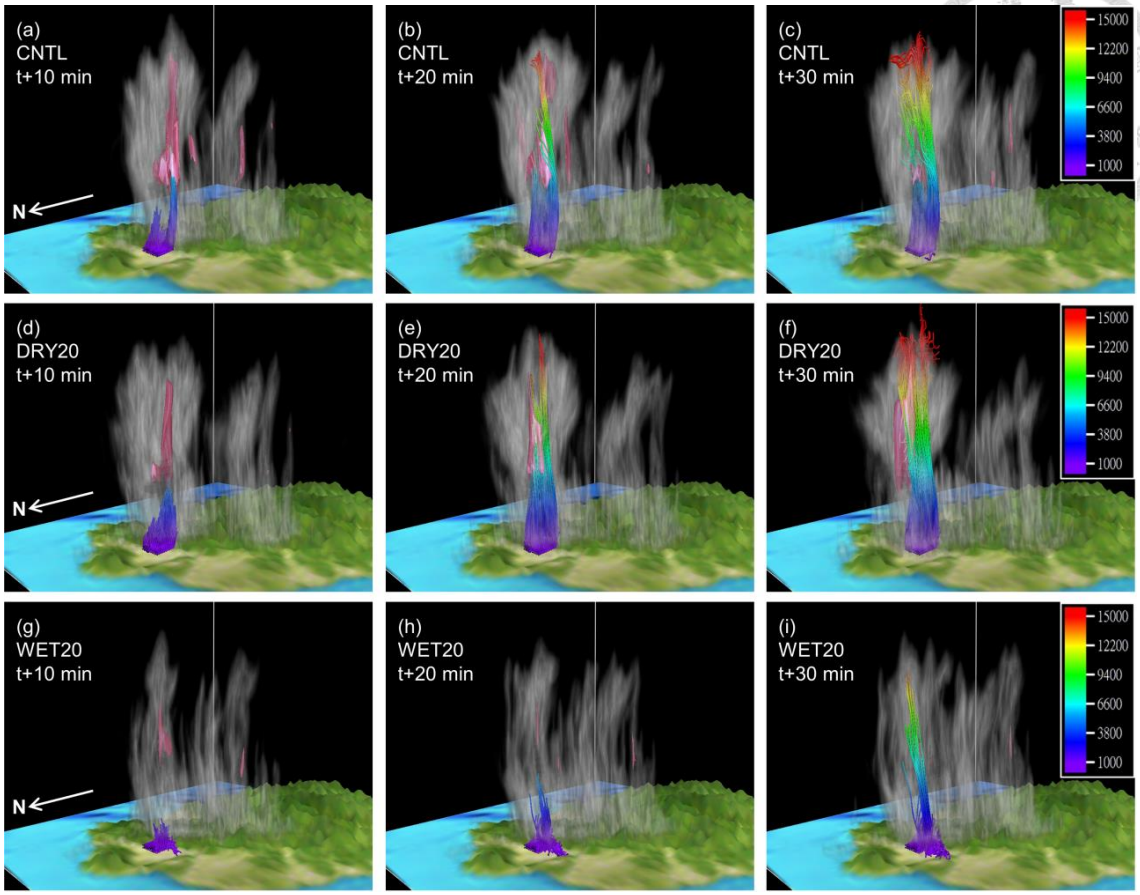

Figure 2.12. (a),(b),(c) Three-dimensional perspective view of the graupel, cloud condensate (sum of cloud water and ice), and air parcel forward trajectories at (a) t + 10 min, (b) t + 20 min, and (c) t + 30 min in the CNTL experiment. The initial time t of forward trajectories is at 1345 LST. The view is from the northwest. The isosurface of graupel (with mixing ratio 12 g kg^{-1}) is shown in raspberry color. Color scale along the trajectory indicates the height (in units of m ASL). Trajectories were initialized at every four model grid points within the rectangle at 400 and 600 m ASL for a total of 200 trajectories. (d),(e),(f) As in (a)-(c), but for trajectories starting at 1420 LST in DRY20 experiment. (g),(h),(i) As in (a)-(c), but for trajectories starting at 1300 LST in WET20 experiment.

doi:10.6342/NTU202504233

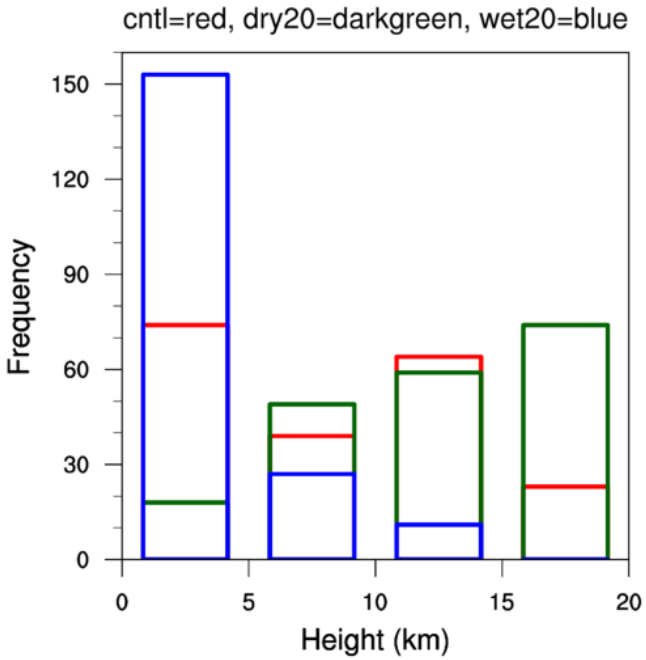

Figure 2.13. Histogram of the final heights attained by the air parcels at t + 30 min for the CNTL, DRY20, and WET20 experiments. For instance, the leftmost blue (red) bar indicates that 153 (74) parcels in WET20 (CNTL) experiment had final heights of less than 5 km ASL.

doi:10.6342/NTU202504233

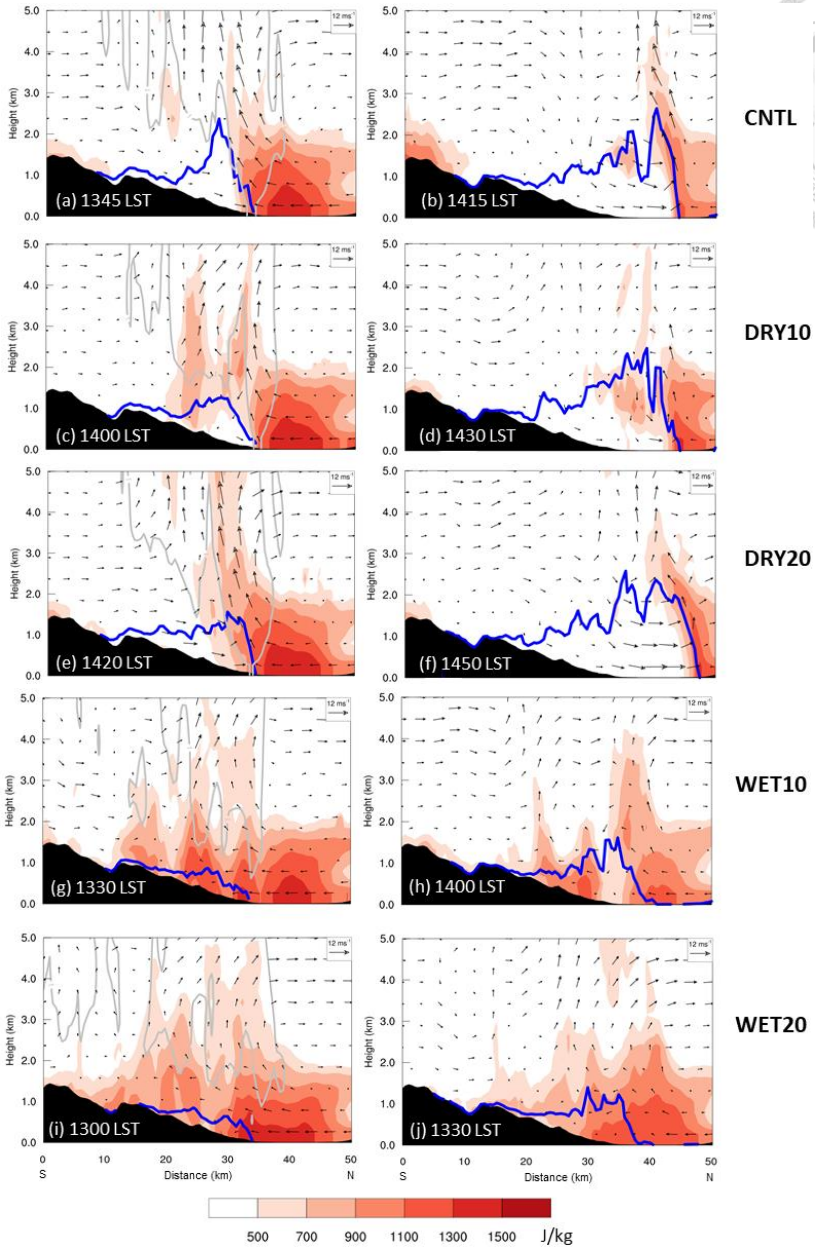

Figure 2.14. Vertical sections of CAPE (in units of J kg^{-1}; colored) for parcels lifted from each vertical level; cold-pool height (thick blue line) and vertical velocity (1 m s^{-1}; gray line). The vertical cross sections are along the N–S direction of the line shown in Fig. 2.4 (after the 10-km average in zonal direction). (a),(b) CNTL, (c),(d) DRY10, (e),(f) DRY20, (g),(h) WET10, and (i),(j) WET20 experiments. The time in LST is indicated at the lower left corner of each panel. (a),(c),(e),(g),(i) Note that the contours of vertical velocity are only plotted at the time before convection development.

doi:10.6342/NTU202504233

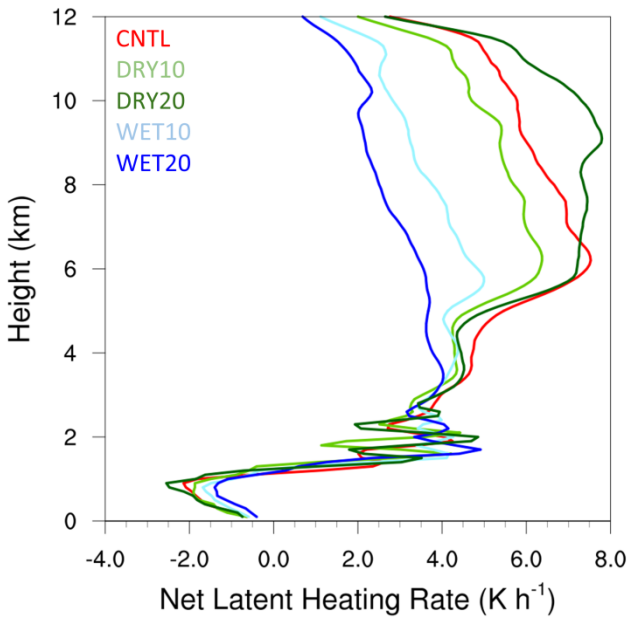

Figure 2.15. Vertical profiles of TB domain 1-h averaged net latent heating rate (in units of K h^{-1}). Profiles are averaged over the TB domain during the time period when the simulated ATS system moved into the TB.

2.4.4 Significance of mid-level dry air

We have examined the sensitivity of ATS intensity to mid-level moisture amount. However, there is a more fundamental problem to ask: why and how was the ATS intensity sensitive to mid-level moisture? Cold-pool dynamics certainly played a critical role in convection development. As a result, it is natural to expect that a notable proportion of cold-pool parcels came from the middle levels. To verify this expectation, 60-min backward trajectories were calculated from 5-min outputs from the CNTL using the VAPOR software. A total of 200 air parcels were traced back from the cold pool within the central Taipei Basin, with initial heights of 200 and 400 m ASL. Figure 2.16a displays the three-dimensional aerial view (from the top) of the 200 backward trajectories. By tracking the final position of these trajectories to the ending time (t – 60 min), we find that 59% of cold-pool parcels were above the TB one hour before, 18% were from the

doi:10.6342/NTU202504233

southern slope, 16% were from Keelung River Valley, and 6% were from the west of TB (see Fig. 2.1d in MY20 for the geography of TB). Figure 2.16b shows the perspective view of 200 trajectories from the west of TB. It is clear that the air parcels from the southern slope were transported by the northward-propagating ATS, with the highest parcel height located at 6.5 km ASL. Trajectory ending-height histogram indicates that 37% of cold-pool parcels descended from 3 km ASL or higher (Fig. 2.17). These statistics support our hypothesis and explain why the storm intensity was sensitive to mid-level RH.

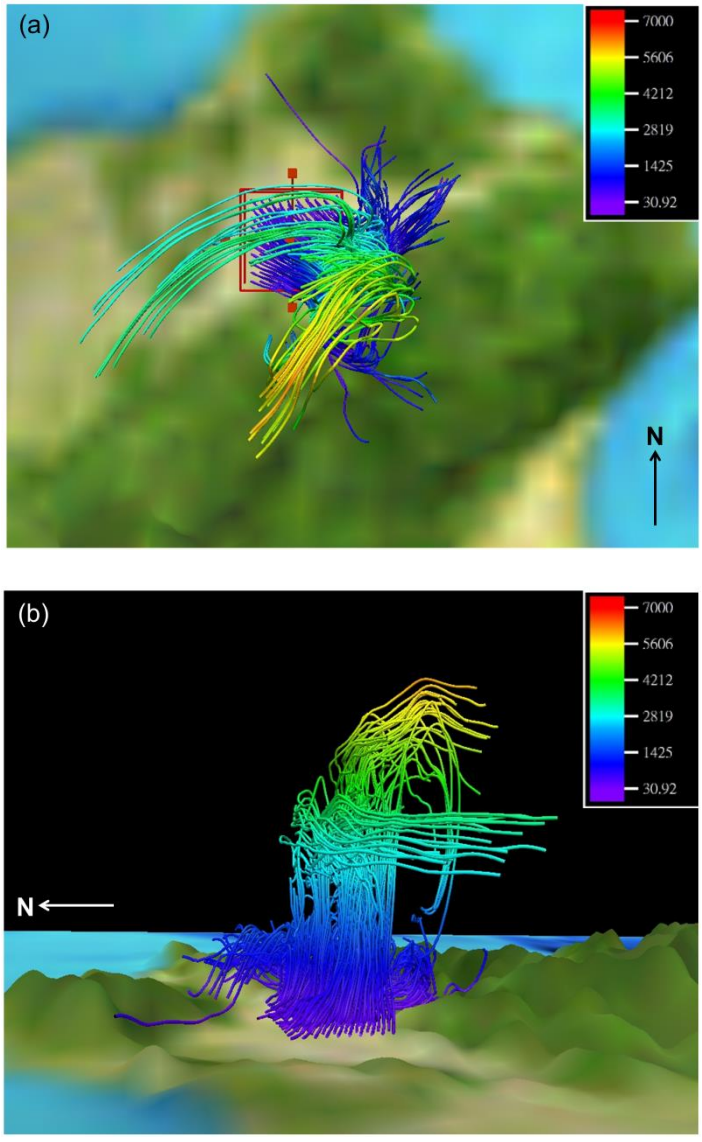

Figure 2.16. Three-dimensional view of the 60-min air parcel backward trajectories in the

doi:10.6342/NTU202504233

CNTL experiment. The view is from the (a) top and (b) west. The starting (ending) time t (t – 60 min) of backward trajectories is 1415 (1315) LST. Color scale along the trajectory indicates the height (in units of m ASL). Trajectories were initialized at every four model grid points within the square [the red box in (a)] at 200 and 400 m ASL for a total of 200 trajectories.

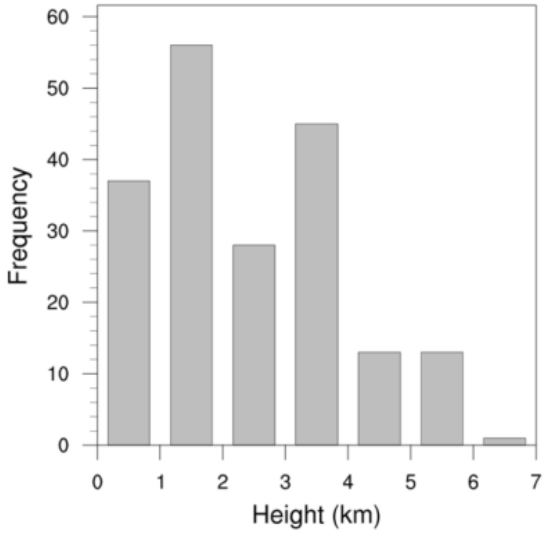

Figure 2.17. Histogram of the heights of backward trajectories at the ending time of t – 60 min.

2.5 Response of ATS to mid-level RH in the absence of Taiwan terrain

To investigate the effect of terrain on the response of convection to mid-level moisture content, we compare the NTER runs (CNTL_NTER, DRY20_NTER, WET20_NTER) with full-terrain runs (CNTL, DRY20, WET20) in this section. The model configuration of NTER runs is the same as full-terrain runs except that the Taiwan terrain is totally removed. Due to the delayed convection initiation in NTER runs, we examined the evolution of ATS during 1400–1700 LST (Fig. 2.18). In full-terrain runs, scattered convection initiated at the mountain slope south of TB, then merged into the

doi:10.6342/NTU202504233

thunderstorm complex, and finally propagated northward to basin plain (Fig. 2.4). Moreover, enhanced low-level convergence produced by sea breeze (northerly) and thunderstorm outflow (southerly) played a vital role in convection development in full-terrain runs. In contrast, the sea breeze (northerly) converged with the large-scale southerly in NTER run (Fig. 2.18). The ATS convection initiated at the northeastern coast and then propagated southward in NTER runs, which is opposite to the full-terrain runs. The southward propagation of ATS in NTER runs is due to the absence of terrain and convective outflow (southerly) at the foothills south of TB. Moreover, NTER simulations had more scattered convection and much weaker convection intensity than those in full-terrain simulations. Regarding rainfall characteristics in the terrain-removal experiments, WET20_NTER experiment had the most accumulated rainfall (Fig. 2.19); followed by CNTL_NTER and DRY20_NTER. Compared to the full-terrain runs, the accumulated rainfall in NTER runs decreased dramatically. It is worth noting that there were no TB-domain grid points with rainfall exceeding 40 mm in 30 min for NTER experiments (not shown). These results indicate that topography has a major impact on storm evolution and rainfall intensity.

For the TB-domain updraft mass flux of the NTER experiments, the updraft mass fluxes were stronger in WET20_NTER and CNTL_NTER experiments, with the contour of 2 $\times 10^9$ kg s^{-1} reaching about 15 km ASL (Fig. 2.20a,c). The updraft mass flux was weakest in DRY20_NTER, with the contour of 2 $\times 10^9$ kg s^{-1} reaching only 6 km ASL (Fig. 2.20b). In addition, WET20_NTER had the highest vertical velocity in the TB domain, followed by CNTL_NTER and DRY20_NTER. These results are consistent with those in James and Markowski (2010). Note that the updraft mass flux in NTER runs was much weaker than that in full-terrain runs (cf. Figs. 2.7a,c,e and 2.20a,b,c). For example, the low-level maximum updraft mass flux in CNTL_NTER run (~6×10^9 kg s^{-1})

doi:10.6342/NTU202504233

was less than that in CNTL run (~10×10^9 kg s^{-1}) by 30%, and the upper-level maximum updraft mass flux in CNTL_NTER (~2×10^9 kg s^{-1}) was less than CNTL (~10×10^9 kg s^{-1}) by 80%.

Before ATS convection dissipated (indicated by the dashed line in Fig. 2.20), DRY20 had the largest entrainment rate, followed by CNTL and WET20 (Fig. 2.20d-f). By comparing NTER results with full-terrain results, we found two main differences. Firstly, the entrainment rate in full-terrain runs was less than that in NTER runs (cf. Figs. 2.9a,c,e and 2.20d,e,f). Secondly, the entrainment rate decreased abruptly with the updraft mass flux in CNTL and DRY20 runs. However, due to the much smaller convection size, these phenomena did not occur in CNTL_NTER and DRY20_NTER runs.

These experiments have highlighted the most interesting possibility: The confined outflow associated with ATS within the TB was forced to converge with the moist sea breeze continuously, providing a favorable dynamic and thermodynamic environment for subsequent convection development. When more convective clouds are triggered at the collision boundary, the spacing among them is reduced and wider clouds are more frequently formed. As a result, the inner portion of updraft is protected by the nearby moist cloudy air, favoring the growth of the clouds into deep convection. In summary, the continuous low-level convergence within the basin plain supports cold pool dynamics and impedes entrainment process. This “basin confinement effect” which results in continuous and enhanced low-level convergence within basin plain, may be crucial for short-duration rainfall extremes over complex terrain.

doi:10.6342/NTU202504233

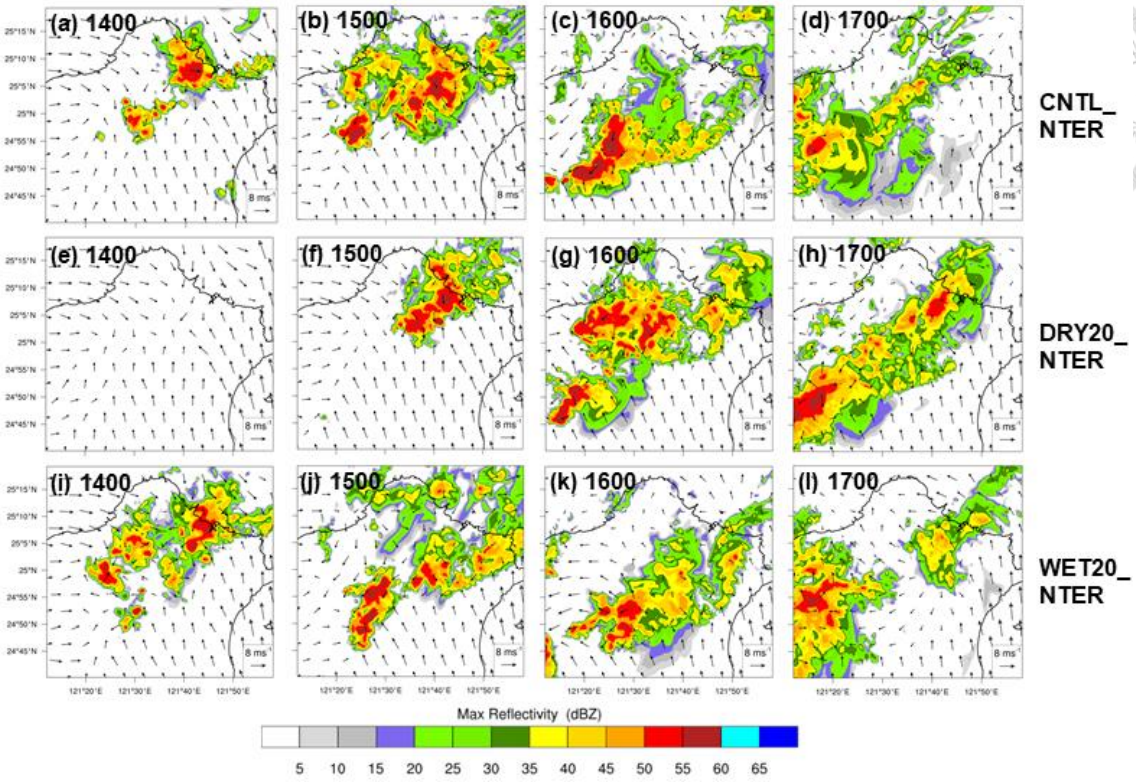

Figure 2.18: As in Fig. 2.4 but for (a),(b),(c),(d) CNTL_NTER, (e),(f),(g),(h) DRY20_NTER, and (i),(j),(k),(l) WET20_NTER experiments during 1400–1700 LST.

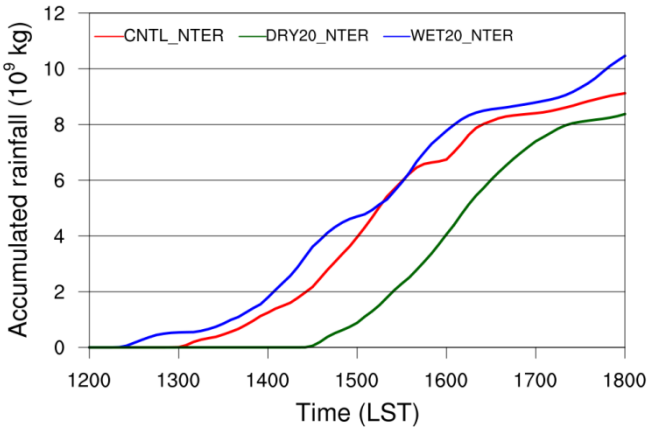

Figure 2.19. As in Fig. 2.6a but for CNTL_NTER, DRY20_NTER, and WET20_NTER experiments during 1200–1800 LST. Note that the y-axis is up to 12×10^9 kg.

doi:10.6342/NTU202504233

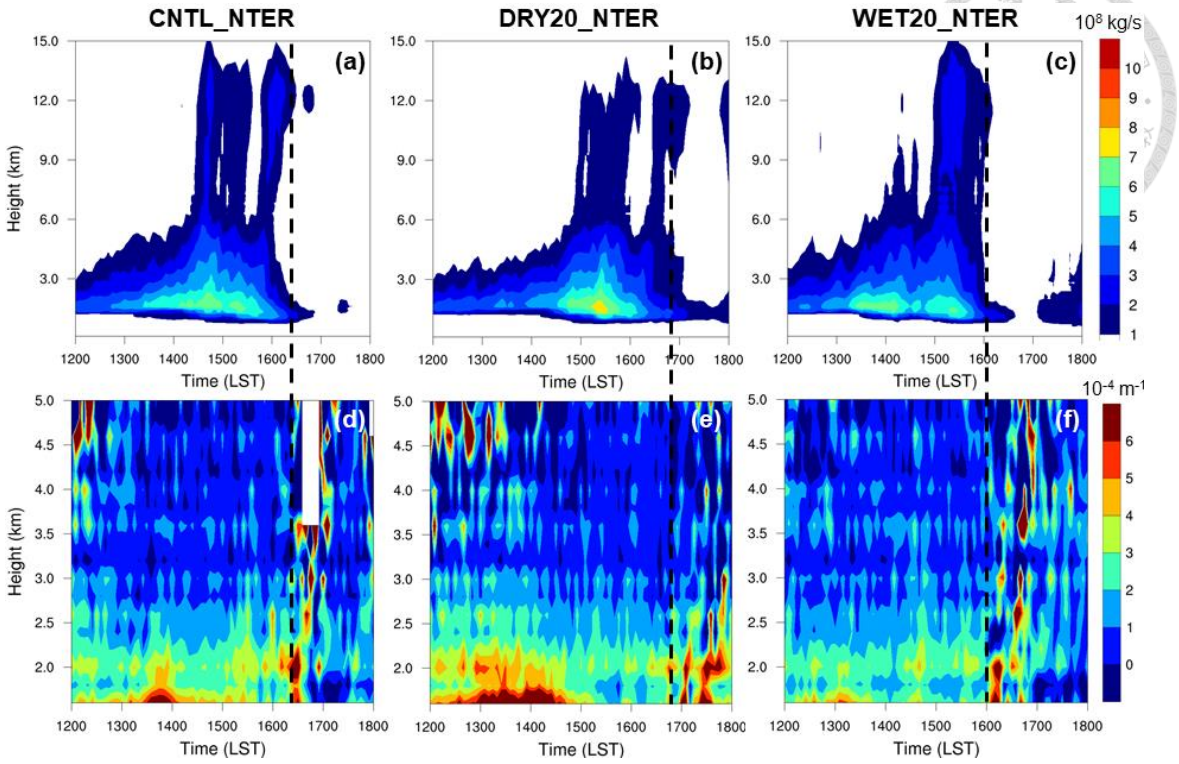

Figure 2.20. (a)(b)(c) As in Fig. 2.7 but for (a) CNTL_NTER, (b) DRY20_NTER, and (c) WET20_NTER experiments during 1200-1800 LST. (d)(e)(f) As in Fig. 2.9 but for (d) CNTL_NTER, (e) DRY20_NTER, and (f) WET20_NTER experiments during 1200–1800 LST. Dashed line indicates the last time when the updraft mass flux is greater than 3×10^9 kg s^{-1}.

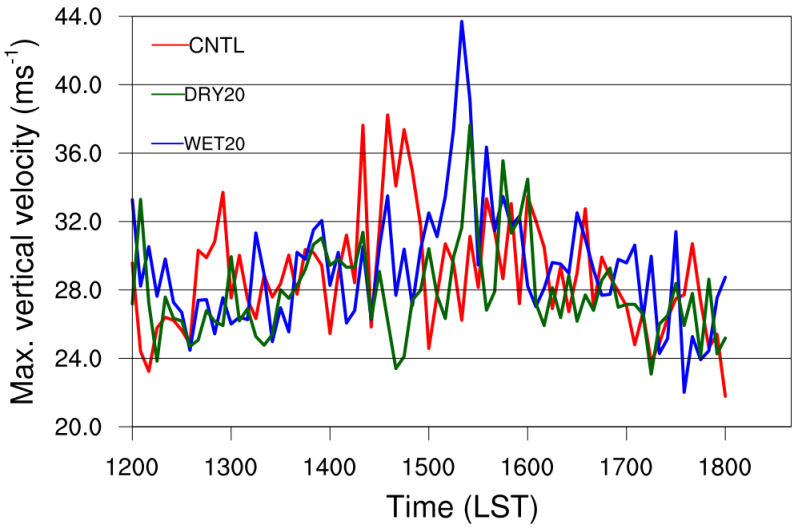

Figure 2.21. TB domain-maximum vertical velocity (in units of m s^{-1}) during 1200–1800 LST from all terrain-removal experiments.

doi:10.6342/NTU202504233

2.6 Discussion and summary

Expanding upon our previous research on the severe afternoon thunderstorm (ATS) system over the Taipei Basin (TB) on 14 June 2015, we have investigated the influence of mid-level relative humidity (RH) on the sea-breeze thunderstorm over basin terrain in this study. The control simulation (CNTL) using the WRF model with the horizontal grid size nested down to 500 m could reasonably capture the onset of the sea breeze, the merger of convective cells, and the evolution of the ATS system (Miao and Yang 2018; Miao and Yang 2020). Four numerical sensitivity experiments that alternatively increased or decreased the mid-level RH by 10% and 20% were conducted. Results from the sensitivity experiments were then compared with those from the CNTL to understand the physical processes leading to the intense ATS when a mid-level layer of dry air occurred. In addition, three mid-level-RH experiments were performed with Taiwan terrain totally removed to examine how Taiwan terrain affected the response of ATS to the mid-level moisture content.

Sensitivity experiment results in section 4 indicated that dry air at middle levels would enhance evaporative cooling, thus producing strong downdrafts and cold pools. This is consistent with previous studies (e.g., Johns and Doswell 1992; Yang and Houze 1995; Gilmore and Wicker 1998). Although the response of convection to mid-level moisture content is somewhat nonlinear, this study focuses on the physical processes leading to heavy rainfall in a dry mid-level environment. Overall, the stronger cold pool of the ATS system in the CNTL and DRY20 experiments would result in two indirect effects on convection:

- Stronger low-level convergence between colliding cold pools provides a favorable condition for convective cell merger (Tao and Simpson 1989; Carey

doi:10.6342/NTU202504233

and Rutledge 2000; Glenn and Krueger 2017; Miao and Yang 2018). The ATS system in CNTL and DRY20 experiments had larger convection size. Thus, the inner portion of convective updraft was shielded by the surrounding moist air and the bulk entrainment rate decreased significantly.

- Stronger low-level convergence between cold pool and sea breeze would lift most of moist parcels to upper levels, providing an abundant source of water vapor for the formation and growth of graupel particles. For example, 63% and 91% of parcels rose above the melting level (~5 km ASL) in the CNTL and DRY20 runs, respectively. On the contrary, only 24% of air parcels could reach above the melting level in the WET20 run. In other words, the ATS in CNTL and DRY20 experiments could consume the 0–1 km integrated CAPE over the TB more effectively, producing stronger freezing and deposition warming at upper levels. Cold pool acts as a conveyer belt, transporting moist air parcels within the sea breeze to the level of free convection and releasing the conditional instability.

Because of the above-mentioned indirect effects of dry air, CNTL and DRY20 experiments had stronger cold pools, more intense convection, stronger updrafts, more graupel particles, stronger net latent heating above the melting level, and much larger areas of the potential flooding region [> 40 mm (30 min)$^{-1}$]. On the other hand, a moister mid-level layer (i.e., WET10 and WET20 experiments) would induce less evaporative cooling and shallower cold pool, producing weaker convection, resulting in a much smaller area of the potential flooding region. Figure 2.22 is the schematic diagram illustrating the response of ATS to mid-level RH for this case over the Taipei Basin on 14 June 2015, under the environment with drier and wetter mid-level conditions. It should be noted that these results can only support the conclusion that

doi:10.6342/NTU202504233

drier air leads to stronger convection in this specific scenario of topography and sea breeze. Schumacher and Peters (2017) indicated that the convective rainfall was highly sensitive to the minor variations in low-level moisture. Our study suggests that the occurrence of short-duration intense rainfall produced by the sea-breeze thunderstorm over basin terrain may increase remarkedly with the decreased mid-level moisture. This issue is rarely discussed in previous studies.

Note that convection in DRY10 was weaker than that in CNTL, suggesting a nonlinear response of convection intensity to mid-level RH. Except for the indirect effects of mid-level dry air on convection, the entrainment process (direct effect) is detrimental to convection. In other words, cold pool and entrainment process exert positive and negative influences on convection intensity, respectively. On one hand, the cold pool intensity and hence the positive effect on convection were similar between the CNTL and DRY10 runs. On the other hand, drier air aloft in DRY10 produced stronger entrainment (negative effect), associated with the reduction in convection size. Therefore, the convective updraft in DRY10 was more prone to the detrimental effect of dry-air entrainment than that in CNTL, and thus convection in DRY10 is weaker. To put it succinctly, the nonlinear response of convection intensity to mid-level RH results from the compensating effects between cold-pool intensity and entrainment process.

James and Markowski (2010; hereafter JM10) investigated the sensitivity of squall lines and supercells to the mid-level dry air. They found that dry air aloft reduced total condensation, total rainfall, and total mass of each condensate species. The updraft and downdraft mass fluxes were also reduced, except in high-CAPE simulation. Moreover, the cold-pool intensity was either unchanged or reduced because the increased evaporative cooling could not offset the decrease of hydrometer mass. Their results do not contradict our current study on ATSs. First of all, in this extreme ATS case, solar

doi:10.6342/NTU202504233

heating and abundant moisture brought by sea breeze increased the CAPE over the TB, providing large conditional instability for the intensification of the thunderstorm convection (MY20). This high-CAPE environment (~3500 J kg^{-1}) produced intense convective storms, which were able to resist the detrimental effect from ambient dry air. The estimation of bulk entrainment rate provides evidence that the entrainment rate could be reduced by stronger cold pool and the widening of moist convection area, consistent with previous studies (e.g., Kuang and Bretherton 2006; Khairoutdinov and Randall 2006; Khairoutdinov et al. 2009; Kurowski et al. 2018). Interestingly, using the buoyancy-sorting model (Raymond and Blyth 1986; Kain and Fritsch 1990), JM10 also indicated that the convection in the high-CAPE environment was capable of withstanding the deleterious effect of dry air aloft.

Secondly, this study examines the ATS system over complex basin terrain, which is different from the convective systems over flat terrain discussed in JM10. The terrain sensitivity experiments in section 5 have highlighted the most interesting possibility: The confined outflow associated with ATS within the TB is forced to converge with the moist sea breeze continuously, providing a favorable dynamic and thermodynamic environment for subsequent convection development. When more convective clouds are triggered at the collision boundary, the spacing among them is reduced and wider clouds are more frequently formed. As a result, the inner portion of updraft is protected by the nearby moist cloudy air, favoring the growth of the clouds into deep convection. To put it succinctly, the continuous low-level convergence within the basin plain supports cold pool dynamics and impedes entrainment process. This “basin confinement effect” which modulates the response of convection to mid-level RH may be crucial for short-duration rainfall extremes over complex terrain. This “basin confinement effect” is a unique feature which is rarely discussed in previous studies on ATS systems over basin terrain.

doi:10.6342/NTU202504233

Previous ATS occurrence checklist (Lin et al. 2012; C16) indicated that mid-level moist air was favorable for thunderstorm development in a "weak synoptic environment", but the checklist did not perform well on this extreme rainfall case which resulted in urban-scale flooding. There are two possible reasons. Firstly, the composite analysis would miss the extreme cases (i.e., statistics outliers). Secondly, when the western North Pacific subtropical high covers northern Taiwan, the low and middle troposphere is relatively dry, inhibiting convection development. Note that mid-level dryness is usually associated with low-level dryness in this scenario. However, northern Taiwan was in the vicinity of the western North Pacific subtropical high for this case, with the deep dry air above moist air. It is suggested that the mid-level (700–500 hPa) mean RH and DCAPE may be critical predictors in severe ATS forecast and warrant further investigation. In addition, the location of western North Pacific subtropical high needs to be reexamined to better define the condition for "weak synoptic environment".

Even though this study can provide valuable insights into the thunderstorm dynamics under the influence of mid-level dry air and complex terrain, it has some limitations. Firstly, conclusions obtained in this study are mainly based on numerical simulations with some model deficiencies, physics uncertainties, and numerical errors, so we should keep these caveats in mind. Secondly, the nonlinear response of convection intensity to mid-level RH may limit the generalization of the results to other thunderstorm events. More case studies are required to generalize the findings from this particular afternoon thunderstorm case to other thunderstorm events in the future. Furthermore, the mid-level moisture sensitivity experiments in this study only address limited aspects of the predictability of the ATS rainfall over the TB. Further works are still needed to examine the sensitivity of ATS rainfall to a broader range of environmental conditions. For example, the large-scale wind direction (Wang and Sobel

doi:10.6342/NTU202504233

2017) and low-level thermodynamic environment (Chen et al. 2017) could also significantly impact the ATSs and their accumulated rainfall.

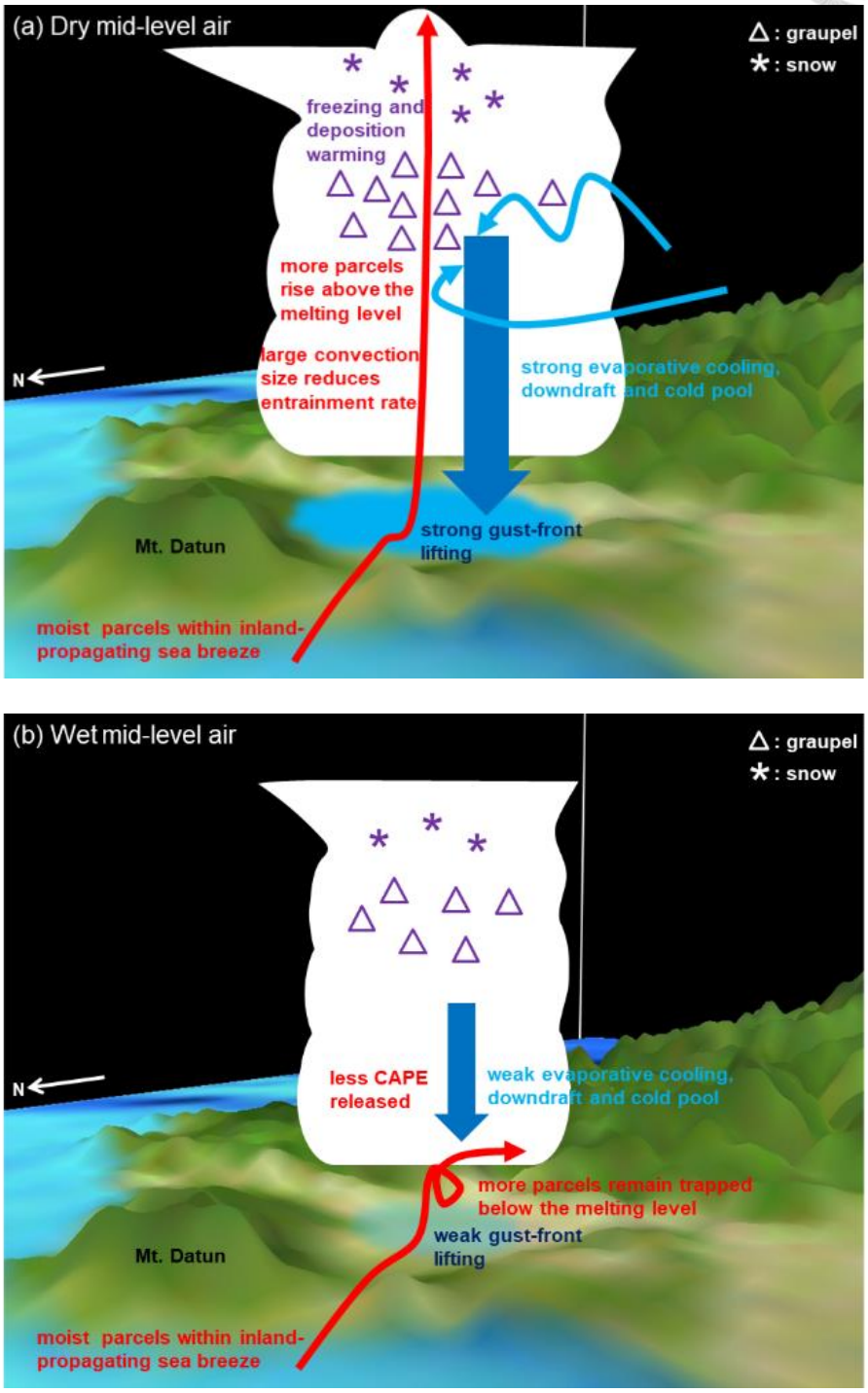

Figure 2.22. Schematic diagram based on the sensitivity experiment results: (a) the control simulation where the environmental middle levels are dry (CNTL), and (b) the experiment where the environmental middle levels are relatively wet (WET20).

doi:10.6342/NTU202504233

Chapter 3 Storm Organization and Microphysics in Strongly-Forced ATSs

3.1 Background

Polarimetric radars offer valuable insights into the microphysical and dynamical characteristics of convective updrafts. Differential reflectivity (ZDR), which represents the difference between horizontally and vertically polarized radar returns, provides information on particle shapes and sizes. A prominent polarimetric signature is the ZDR column, an enhanced ZDR region that extends above the environmental 0°C level in strong updrafts, indicating the presence of large supercooled drops, ice crystals, graupel, or hail undergoing wet growth (Illingworth et al. 1987; Kumjian et al. 2014). While ZDR columns in midlatitude storms can extend over 3 km above the freezing level, those in subtropical storms typically rise 1–2 km above it (Yu et al. 2022; Jung and Jou 2023). Algorithms such as the one developed by Snyder et al. (2015) enable identification and quantification of ZDR columns in operational radar data, aiding in storm evolution assessment. Recent studies (e.g., Kuster et al. 2019; French and Kingfield 2021) have highlighted the potential of ZDR column area as an indicator of storm intensity for nowcasting applications.

Additionally, polarimetric radars can reveal microphysical processes through unique polarimetric fingerprints related to particle size, shape, and phase. Kumjian and Ryzhkov (2012) introduced a framework to diagnose dominant precipitation processes by analyzing vertical gradients of ZH and ZDR in the warm cloud layer. Observations from the tropical DYNAMO/ARM-AMIE project showed that convective cases often

doi:10.6342/NTU202504233

exhibit fingerprints of coalescence and evaporation, while stratiform cases reveal signatures of breakup, coalescence, and evaporation (Kumjian and Prat 2014).

The convective cell merger process occurs when two or more convective cells merge and form a larger and more intense storm (Tao and Simpson 1989; Carey and Rutledge 2000; Moseley et al. 2016; Glenn and Krueger 2017). This process played an important role in the development of ATSs over the Taipei Basin (Jou et al. 2016; Miao and Yang 2018) and also occurred in TAHOPE/PRECIP IOP 2 (31 May 2022). JJ23 suggested that decreased ZDR and increased specific differential phase (KDP) near the 0°C level after the merging indicated the increasing graupel concentration. The abundance of melted graupel enhanced ZDR and KDP below the 0°C level, which was related to the subsequent heavy rain.

Although polarimetric radars have significantly advanced our understanding of microphysical processes in convective storms, detailed case studies focusing on thunderstorms in northern Taiwan remain limited (e.g., JJ23). Most prior research has been conducted in the U.S., particularly over the Great Plains, where environmental conditions and orographic characteristics differ substantially from those in Taiwan (e.g., Kumjian and Ryzhkov 2008; Picca and Ryzhkov 2012; Bodine and Rasmussen 2017; Van Den Broeke 2017; Van Den Broeke 2020; Wilson and Van Den Broeke 2021; Segall et al. 2022; Tam et al. 2022; Klaus et al. 2023). Moreover, previous studies on ATSs over the Taipei Basin (e.g., JJ23) used reconstructed RHIs to identify ZDR columns and other polarimetric features. However, the time difference between radar scans and spatial interpolation errors may significantly impact the pseudo-RHI results (Snyder et al. 2015), limiting the interpretation.

High-quality RHIs from the S-Pol radar can provide detailed insights into the microphysical and kinematical characteristics of deep convection that were unavailable

doi:10.6342/NTU202504233

for previous studies in northern Taiwan. In addition, we used the Spline Analysis at Mesoscale Utilizing Radar and Aircraft Instrumentation (SAMURAI-TERRAIN; Bell et al. 2012; Cha and Bell 2023) software, a three-dimensional variational analysis method that can retrieve multi-Doppler winds over complex terrain. We investigate the microphysics and kinematics of the severe ATS in TAHOPE/PRECIP IOP 2 utilizing a unique combination of S-Pol observations and 3D winds retrieved by SAMURAI-TERRAIN. This is the first time this novel radar technique has been used to observe convective-scale processes in northern Taiwan. The primary objective of this study is to compare the microphysical and kinematic characteristics of merged and isolated convective cells, and to identify the key physical processes leading to the extreme orographic rainfall in ATSs. In addition, we investigate how updraft strength relates to observed ZDR column characteristics. By analyzing these advanced radar observations, we aim to gain new insights into the microphysical and kinematic characteristics of ATSs producing heavy rainfall over the mountainous region.

Section 3.2 details our data sources and the tracking algorithm. In section 3.3, we analyze the pre-storm synoptic environment and storm evolution. The main results are presented in section 3.4. Section 3.5 provides the discussions and summary.

3.2 Data and methodology

3.2.1 Polarimetric measurements from S-Pol

We utilized the level-II polarimetric products from the NCAR S-Pol radar (NCAR/EOL S-Pol Team 2023) to examine polarimetric radar signatures in the ATSs on 31 May 2022, which was IOP 2 of TAHOPE/PRECIP. The S-Pol scanning strategy alternated between the PPI and RHI modes every 12 minutes. To ensure unbiased RHI

doi:10.6342/NTU202504233

sampling, the RHI mode employed a combination of fixed and user-defined azimuth angles. The fixed azimuth angles provided a statistically representative dataset of convective structures, while the user-defined azimuth angles were adjusted in real time to target active convection regions. S-Pol plays a vital role in minimizing errors caused by attenuation and hail contamination (Chang et al. 2015). Most importantly, the S-Pol polarimetric RHI scans, which provide invaluable insights into the microphysical features of precipitation systems, have previously been unavailable for observational studies on the ATSs in northern Taiwan.

The Python ARM Radar Toolkit (Py-ART; Helmus and Collis 2016) was used to interpolate PPI scans onto a Cartesian grid with a horizontal grid spacing of 1 km and a vertical grid spacing of 0.5 km. The primary radar parameters analyzed in this study were ZH, ZDR, and KDP. The quality control procedure removed radar gates with correlation coefficient (ρ_{HV}) < 0.8 or ZH < 0 dBZ to eliminate the non-hydrometeor signals. The particle identification (PID) provides the most likely particle type at every gate within the three-dimensional scan. This categorization is achieved using a fuzzy logic algorithm (Vivekanandan et al. 1999), which quantifies the probability of various particle types based on different polarimetric variable ranges. This study used the RadxPid algorithm within the Lidar Radar Open Software Environment (LROSE; DeHart et al. 2024) to perform PID, enabling robust hydrometeor classification.

3.2.2 Kinematic field retrieval from SAMURAI-TERRAIN

Multi-Doppler analyses were generated using the SAMURAI-TERRAIN software (Bell et al. 2012; Foerster and Bell 2017; Cha and Bell 2023), a component of the LROSE. SAMURAI-TERRAIN employs a three-dimensional variational data assimilation technique, integrating radar observations and cubic b-spline basis functions

doi:10.6342/NTU202504233

to produce the most probable atmospheric state by minimizing a cost function. In this process, SAMURAI-TERRAIN calculates the three-dimensional wind field, incorporating mass continuity as a numerical constraint. Moreover, the impermeability and topographic forcing boundary conditions are implemented at the terrain height. The outcome is a 3D cubic spline representation of the wind field. The multi-Doppler winds were synthesized with a horizontal spline nodal spacing of 1 km and a vertical nodal spacing of 0.5 km. Gaussian filters with a $4\Delta x$ length in the horizontal plane and $2\Delta x$ length in the vertical direction were applied. This nodal spacing and filter length led to a minimum resolved scale of approximately 4 km horizontally. Further details on SAMURAI-TERRAIN can be found in Cha and Bell (2023).

This study utilizes RHI data from S-Pol radar and PPI data from RCWF and RCSL radars to perform wind retrieval (see the radar locations in Fig. 3.1). RCWF is a WSR-88D dual-polarization radar operating in PPI mode, completing a full volume scan approximately every 6 minutes. RCSL is a METEOR 1700C C-band dual-polarization radar, also operating in PPI mode, with a volume scan interval of approximately 7 minutes. Further details on these radars can be found in Chang et al. (2021).

Before the wind retrieval process, the PPI data of RCWF and RCSL radars was quality-controlled using the Py-ART software. Additionally, the 78° and 83° RHI data of S-Pol radar are also quality-controlled and used in the wind retrieval to obtain better coverage of the wind analysis in deep convection. The 78° azimuth was selected to capture cell mergers in Episode 1, allowing detailed analysis of storm interactions, while the 83° azimuth targeted convection farther south in Episode 2. The time difference between the PPI scans from RCWF and RCSL and the RHI scans from S-Pol was less than 5 minutes. Utilizing data from PPI and RHI, the multi-Doppler analysis

doi:10.6342/NTU202504233

offered comprehensive 3D winds and further aided in analyzing the interaction between convective cells over complex terrain.

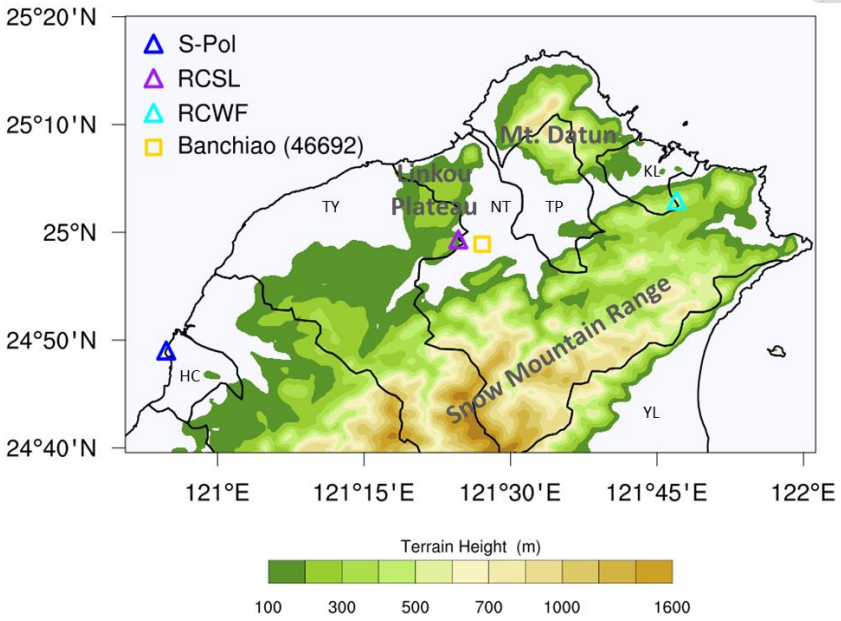

Figure 3.1. Northern Taiwan domain with terrain elevations plotted (colored; in units of meter). The primary instruments including S-Pol, RCWF, and RCSL radars are indicated. The location of the Banchiao sounding station (46692) is also labeled. The main cities on the map are Taipei (TP), New Taipei (NT), Keelung (KL), Taoyuan (TY), Hsinchu (HC), and Yilan (YL).

3.2.3 Tracking algorithm for ZDR columns

Detecting ZDR columns is complicated by the relatively limited mid-tropospheric resolution and coverage inherent in the scanning strategies of many operational weather radars (Snyder et al. 2015). Scanning in elevation (i.e., RHIs) helps eliminate spurious tilting caused by data collection delays and enables more accurate quantification of ZDR columns. Thus, we employed “tobac” (Heikenfeld et al., 2019), a recently developed framework designed for the tracking and analysis of individual features in various data sources, on the RHI data from S-Pol.

Using the Python package tobac, ZDR columns were identified in each RHI scan

doi:10.6342/NTU202504233

in the gridded field of ZDR. The tracking library allows for smoothing the input field using a Gaussian filter. After testing different smoothing options, we set the Gaussian filter to 1, which results in minimal smoothing of the ZDR field and keeps the details of the ZDR column structure in the original data. To detect ZDR columns, we adopted the ZDR threshold of 1 dB used in previous studies (Snyder et al. 2015; Kuster et al. 2019). The minimum number (15) of contiguous pixels for the feature to be detected is set to avoid extraneous points to be detected as erroneous features because the focus of this paper is on ZDR columns associated with the updrafts in deep convection. A ZDR column feature is hence defined as a contiguous area with ZDR > 1dB extending ≥ 5 km AMSL.

3.2.4 Measurement of ZDR Column Width

Previous studies (e.g., Kuster et al. 2019; French and Kingfield 2021) have analyzed updraft area proxies and found a positive correlation between ZDR column area and severe weather in the U.S. In this study, we utilize high-quality RHI scans to determine ZDR column width, rather than ZDR column area. Given that updraft width and area are related, this study directly measures proxies for updraft width. We focus on the width of the enhanced ZDR region (> 1 dB) at 5.5 km AMSL, which is approximately 0.5 km above the environmental 0°C level based on the sounding data from this case and consistent with the May-June climatology in northern Taiwan (Lee et al. 2019). This analysis height was selected to reduce potential contamination near the melting layer (Van Den Broeke 2017; Kuster et al. 2019; French and Kingfield 2021) while ensuring a sufficient sample size. The calculated width is defined as the maximum horizontal extent of enhanced ZDR values (>1 dB) at 5.5 km AMSL, representing their full coverage at that level.

doi:10.6342/NTU202504233

3.3 Case overview

The TAHOPE/PRECIP IOP 2 was chosen because it presented a unique opportunity to study ATSs producing extreme rainfall over complex terrain. The planning of TAHOPE/PRECIP IOP 2 anticipated heavy rainfall over the entire Taipei Basin, including both the basin plain and mountainous regions. However, the event resulted in heavy rainfall occurring predominantly over the mountainous areas, with significantly less precipitation observed in the basin plain. Additionally, operational model forecasts performed poorly for this extreme rainfall event. This case represents a unique opportunity to improve our understanding of the physical mechanisms leading to extreme orographic rainfall and to explore the limitations of current forecasting models. This section examines the synoptic conditions and storm evolution for this terrain-confined ATS event.

3.3.1 Mesoscale environment

On 31 May 2022 at 08 LST (00 UTC), the 700-hPa relative humidity exceeded 80% over the ocean north of Taiwan, while inland values were ~70 % (Fig. 3.2a). At 850 and 925 hPa, prevailing southwesterly monsoonal winds transported high-θ_e air (>342 K) toward Taiwan, where a leeside low was observed northeast of the island (Figs. 3.2b,c). This leeside pressure feature was also evident at the surface, accompanied by a surface front located offshore of northern Taiwan (Fig. 3.2d). Radar quantitative precipitation estimates (QPE; Fig. 3.2e) indicate that the heaviest rainfall occurred along the SMR, with 12-h accumulations exceeding 150 mm. Additional heavy rainfall was also observed along the eastern coastal region. This extreme rainfall event occurred

doi:10.6342/NTU202504233

under a strong synoptic environment, characterized by southwesterly monsoonal flow and a surface front near the northern coast of Taiwan.

The sounding at the Banchiao station (Fig. 3.3a) indicated weak convective instability for the thermodynamic conditions at 0800 LST. Although the moisture was abundant at the low and middle levels, the near-surface inversion impeded the ascent of surface air parcels and led to an insignificant surface-based CAPE value (near 0 J kg^{-1}) in the morning. Weak winds prevailed in the Taipei Basin within the boundary layer, associated with prevailing southwesterly winds (20–25 kt) at 800–500 hPa. Note that the layer between 925–850 hPa was saturated, which suggests limited solar heating and surface temperature increases for the day. At 1100 LST, the wind below 950 hPa turned northerly (Fig. 3.3b), indicating the sea breeze penetrating the Taipei Basin. The moisture brought by the sea breeze and the surface warming due to diurnal heating led to a significant increase in CAPE to 2600 J kg^{-1}, consistent with the results in Miao and Yang (2020).

doi:10.6342/NTU202504233

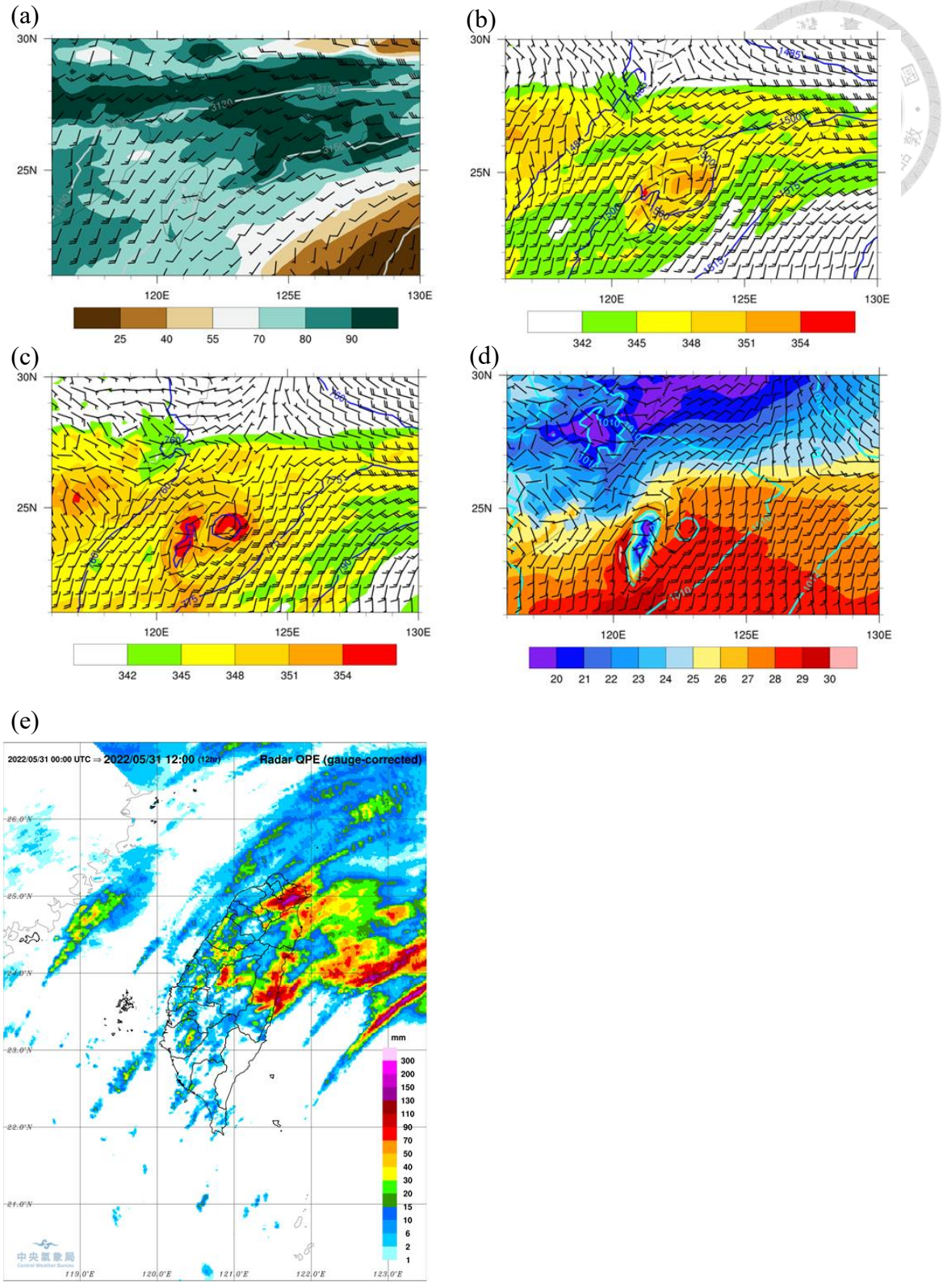

Figure 3.2. Mesoscale environment at 0000 UTC (0800 LST) 31 May 2022: (a) 700-hPa map with the geopotential height (contours), relative humidity (colored), and horizontal wind (barbs; full barb is 10 kts, half barb is 5 kts); (b) As in (a), but for 850-hPa map with equivalent potential temperature (colored); (c) As in (b), but for 925-hPa; (d)

doi:10.6342/NTU202504233

surface map with the mean sea level pressure (contours), 2-m temperature (colored), and horizontal wind. (e) Radar quantitative precipitation estimates (QPE) accumulated from 0000 to 1200 UTC on 31 May 2022. Source of (e): Central Weather Bureau.

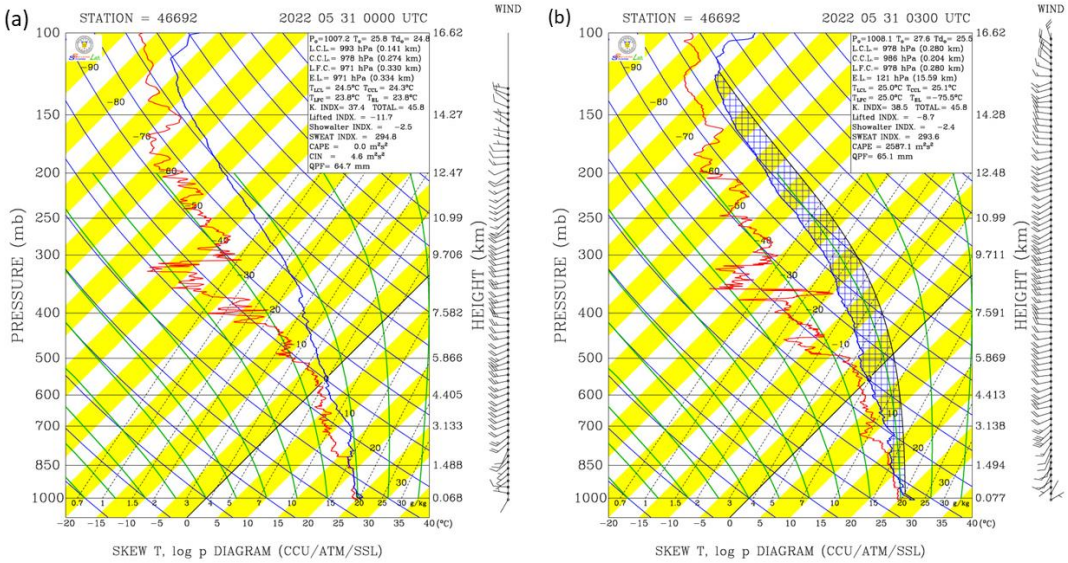

Figure 3.3. Soundings of temperature (blue line) and dew point (red line) at Banchiao station (46692) at (a) 0800 and (b) 1100 LST 31 May 2022. The location of Banchiao sounding station is shown in Fig. 3.1.

3.3.2 Storm evolution

Convective cells initiated near the foothills of the Snow Mountain Range (SMR) around 1140 LST. Subsequently, the convection gradually evolved into an organized ATS system. Strong radar reflectivity values (> 40 dBZ) mainly occurred over the SMR in the afternoon on 31 May 2022 (Fig. 3.4a). In contrast, there was no significant signal of strong convection over the basin plain, which is different from a previously studied ATS case on 14 June 2015 (e.g., Miao and Yang 2020; JJ23). There were two episodes of convection with ZH > 40 dBZ in this case (Fig. 3.4b,c). Episode 1 occurred from 1200–1400 LST and Episode 2 occurred from 1500–1700 LST. The convection in both episodes propagated northeastward; however, the convection in Episode 1 exhibited a broader and more persistent region of strong reflectivity, indicating a higher degree of

doi:10.6342/NTU202504233

organization (1240–1330 LST; Fig. 3.4b,c). Note that the convection was confined within the mountainous region (Fig. 3.4c), resulting in heavy rainfall over the SMR but only weak rainfall over the basin plain.

To investigate the role of local circulation in this terrain-confined thunderstorm event, the evolution of reflectivity and multi-Doppler winds at 1.5 km AMSL is shown in Fig. 3.5. It is clear that there were multiple mergers of convective cells in Episode 1. Following Miao and Yang (2018), a cell merger is defined as a situation when the 40-dBZ ZH radar contour connects at 1.5 km AMSL, lasting for at least 24 min. At 1200 LST, three convective cells, A, B, and C, were located at the foothills (Fig. 3.5a). Subsequently, cells A and B merged and then intensified slightly (Fig. 3.5b,c).

Southwesterly flow occurred over western SMR (< 121.5E) at 1200 LST, similar to the prevailing low-level winds shown by the sounding. On the other hand, southeasterly flow prevailed over the eastern SMR (> 121.5E), which appeared to be the upslope wind. Although cells A and B were located in an environment with southwesterly winds, the winds were weaker near cell B and even shifted to northwesterly at the foothills. The difference in environmental wind speeds near cells A and B suggests that the physical mechanism of single cell merger (SCM; i.e., the merge of cells A and B) may be a "rear-end collision" type due to the different propagation speeds (Miao and Yang 2018). It should be noted that the upslope (northwesterly) winds became more significant at the northwestern foothills in the SMR and converged with the southeasterly flow at 1236 LST, producing enhanced low-level convergence over the mountainous region. Cell A+B merged with cell C and formed a large area of strong reflectivity around 1248 LST (Fig. 3.5d). After the multiple cell merger (MCM; the merger of A+B and C), the new convective cell A+B+C intensified significantly (Fig. 3.5e). The orientation of the strong echoes and the enhanced low-level convergence region were both parallel to the

doi:10.6342/NTU202504233

SMR, implying that the terrain might play an important role in this MCM event. Afterward, the merged cell propagated northeastward and weakened slightly at 1336 LST (Fig. 3.5f).

The ATSs in Episode 2 showed a distinct multicellular structure (Fig. 3.6). It is clear that convective cells in Episode 2 were more isolated and much weaker than in Episode 1. Moreover, there was no cell merger in Episode 2. Note that the enhanced low-level convergence over the SMR seen in Episode 1 was absent in Episode 2 (cf. Figs. 3.5c, 3.6c). One reason for this difference could be a weaker temperature gradient from previous rainfall. Interestingly, there was a cyclonic circulation near the coastline in Yilan County at 1500 LST (Fig. 3.6a), corroborated by NCEP FNL (Final) Operational Global Analysis (not shown). Afterward, this vortex appeared to form a closed circulation and moved northward during 1536–1600 LST (Fig. 3.6b,c). Meanwhile, the easterly winds north of the vortex penetrated into the SMR. The convection over the SMR was located at the front of the advancing easterly winds and weakened gradually (Fig. 3.6c,d). The comparison between Episodes 1 and 2 indicates that convective cells in Episode 2 were isolated and weaker in the absence of the enhanced upslope wind over the SMR region, suggesting the importance of thermally-driven flow in convective organization and development.

doi:10.6342/NTU202504233

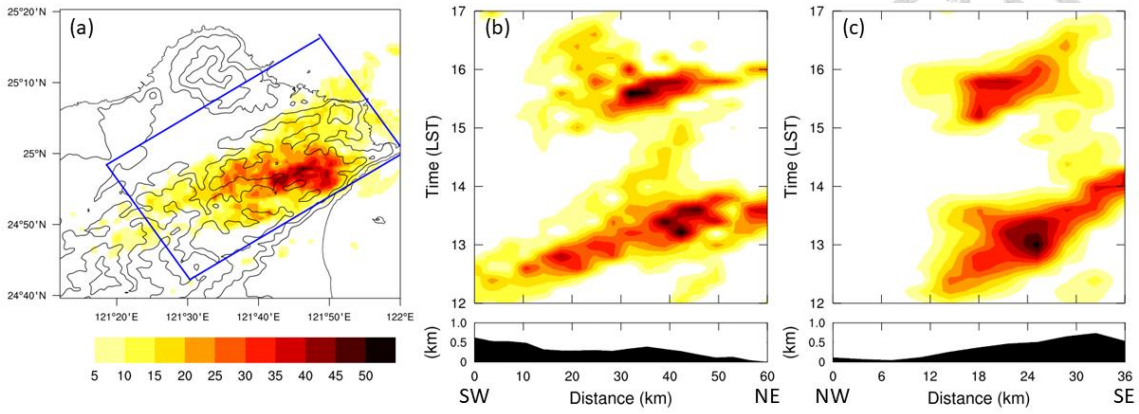

Figure 3.4. Temporal and spatial distribution of ZH at the height of 3 km AMSL on 31 May 2022. (a) Occurrence frequency (%) of ZH > 40 dBZ between 1200 and 1700 LST. Terrain heights are contoured by gray lines at 100, 300, 700, and 1300 m. (b) The averaged spatial frequency of ZH > 40 dBZ along the southwest–northeast direction of the blue rectangle in (a). The average terrain height is indicated at the bottom. (c) As in (b), but along the northwest–southeast direction.

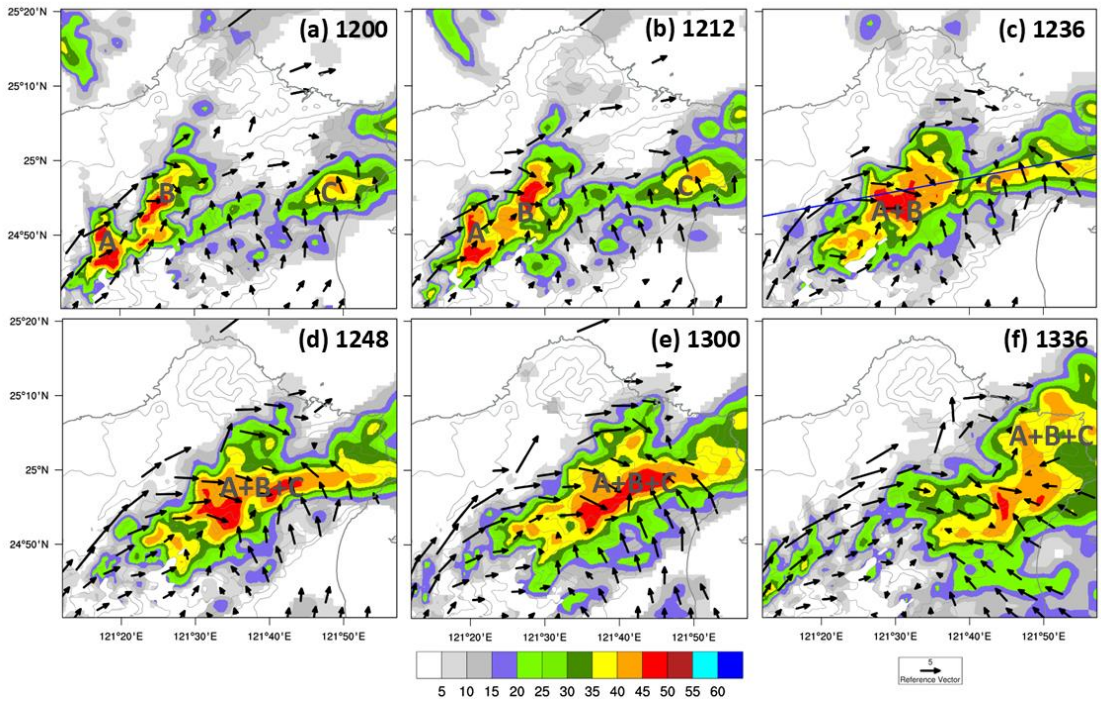

Figure 3.5. Constant-altitude plan position indicator (CAPPI) of radar reflectivity at 1.5 km AMSL from S-Pol radar on 31 May 2022: (a) 1200 LST, (b) 1212 LST, (c) 1236 LST, (d) 1248 LST, (e) 1300 LST, and (f) 1336 LST. Multi-Doppler retrieved horizontal wind at 1.5 km AMSL (arrows) is also indicated. Terrain heights are contoured by gray lines at 100, 300, 700, and 1300 m. Blue line in (c) show the location of the vertical cross sections (S-Pol 78° RHI) in Figs. 3.7–3.11. The convective cells A+B, C and A+B+C are labeled.

doi:10.6342/NTU202504233

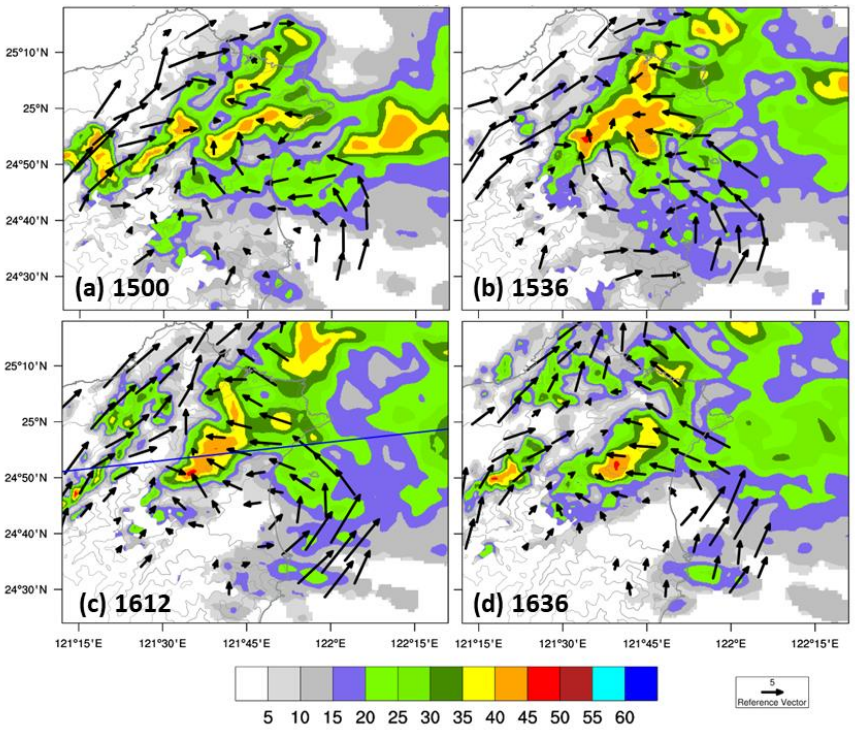

Figure 3.6. As Fig. 3.5, but for (a)1500 LST, (b)1536 LST, (c)1612 LST and (d)1636 LST. Note that the domain is larger with terrain heights contoured by gray lines at 100, 700, 1300, and 2000 m. The blue line in (c) show the location of the vertical cross sections (S-Pol 83° RHI) in Figs. 3.12–3.13.

3.4 Results

3.4.1 Episode 1: Multiple cell merger (MCM)

The detection of ZDR columns can be challenging due to operational radar resolution and storm motion effects (Snyder et al. 2015). To get an accurate quantification of ZDR columns, the evolution of RHIs from the S-Pol radar with an azimuth of 78° is shown in Figs. 3.7–3.10. Luckily, these high-resolution RHI scans captured the merger of A+B and C in Episode 1, providing valuable insights into the MCM process.

The reflectivity plot at 1223 LST (Fig. 3.7a) shows the position and height of two convective cells A+B and C, with cell A+B exhibiting the stronger convection. Cell

doi:10.6342/NTU202504233

A+B had high ZH exceeding 55 dBZ and a 20-dBZ echo top of 14.5 km AMSL. The ZDR plot (Fig. 3.8a) reveals ZDR columns in cells A+B and C at x (distance from the radar) = 60 km and x = 100 km, respectively, with heights reaching approximately 6 km, indicating the presence of convective updrafts. The ZDR value within the ZDR column of cell A+B (x ~ 60 km) is relatively large, with local maxima located at the middle (4–5 km AMSL) and low levels (< 2 km AMSL). The area of high ZDR (> 2.0 dB) values at middle levels corresponds to hail/rain and graupel/rain mixtures (Fig. 3.10a). Additionally, the PID shows the presence of graupel and small hail in cell A+B at 5–10 km AMSL, suggesting ongoing riming processes and the presence of supercooled liquid water. The KDP plot (Fig. 3.9a) reveals the existence of a KDP column coincident with a ZDR column (x = 60 km), which might be due to the low environmental wind shear (Kumjian and Ryzhkov 2008). However, there is no prominent KDP column in cell C because it was relatively weak and had low liquid water content.

Note that at 1223 LST, developing cumulus and congestus clouds were observed between the two convective cells at x = 70–90 km. Subsequently (Fig. 3.7b), these clouds extended above 8km AMSL by 1235 LST. The cumulus and congestus clouds that developed between cells A+B and C coincided with the low-level convergence produced by upslope winds (Fig. 3.5b), highlighting the role of terrain-induced circulation in this MCM process.

Before the merger, the 20-dBZ echo top only reached 14.5 km AMSL. After the merger of cells A+B and C, there was a significant increase in the horizontal and vertical extent of the high ZH (Fig. 3.7c,d) with the echo top exceeding 16 km AMSL. After the MCM, the enhanced ZDR region (>1 dB) broadened, accompanied by the merger of ZDR columns (Fig. 3.8c,d). The merged ZDR columns had a larger horizontal and vertical extent than the isolated ZDR columns before the MCM process (Fig.

doi:10.6342/NTU202504233

3.8a,d). Since a ZDR column is a proxy for convective updrafts and its scale is correlated with updraft characteristics (Bringi et al. 1991; Kumjian et al. 2014), the occurrence of merged ZDR columns may suggest wider updrafts.

The KDP field at the time of the MCM (Fig. 3.9c) showed a KDP column at x = 84 km with a height of 7 km AMSL (~2 km above the 0°C level). The maximum value of KDP (~ 3.5 deg km^{-1}) occurred below the melting level, and the magnitude was larger after the MCM process. The KDP column above the melting level was composed of abundant graupel, small hail, and rain/hail mixture (Fig. 3.10c), indicating an active mixed-phase process. KDP was positively correlated with ZH in the merged cell below the melting level, likely because the bulk of graupel/hail melted into raindrops producing high KDP. Therefore, it can be inferred that active riming occurred above the melting level, and a large amount of graupel/hail melted into raindrops below the melting level.

At 1259 LST, the merged cell exhibited a maximum ZH of ~ 60 dBZ, signifying the presence of hail aloft (Fig. 3.7d). ZDR and KDP columns were observed at x = 85 km with a height of about 7 km (~2 km above the 0°C level; Figs. 3.8d and 3.9d). PID (Fig. 3.10d) shows a significant increase in the horizontal extent of the graupel/small hail mixture and the height extended to 12 km AMSL. Furthermore, there was an increase in the occurrence of hail, rain/hail, and graupel/rain mixtures at x ~ 80–91 km. Some water-coated graupel and large supercooled raindrops may have produced high values of KDP (> 2.5 deg km^{-1}) above the freezing level and formed the upper part of the KDP column (Ryzhkov and Zrnic 2019). Below the melting level to a height of 3.5 km (x = 80–91 km), a large amount of graupel/rain and rain/hail mixture was observed, corresponding to high ZDR (> 2 dB), possibly attributed to the large raindrops produced by the shedding and melting of graupel and hail.

doi:10.6342/NTU202504233

Previous results show that microphysics in the merged cell transitioned to more active riming and melting processes. To shed more light on the storm kinematics and its connection with polarimetric signatures, multi-Doppler winds interpolated to the S-Pol 78° RHI position are shown in Fig. 3.11 and provide valuable insights into cell merger dynamics. At 1223 LST, the retrieved updrafts match well with the ZDR columns of cells A+B and C at x = 60 km and 100 km, respectively (Figs. 3.8a, 3.11a). The upward motion between cells A+B and C was associated with the low-level convergence produced by upslope winds (Fig. 3.5b). As the cells and associated updrafts became closer at 1235 LST, the compensating downdraft at the upper levels between them extended down to 8 km AMSL (Fig. 3.11b).

Before the cell merger, the maximum vertical velocity w was ~12 m s^{-1}. The mid-to-upper-level updrafts (> 4 m s^{-1}) merged and intensified dramatically to ~18 m s^{-1} while the cells A+B and C merged (Fig. 3.11c). Note that this wide and strong updraft in the merged cell following the MCM process was associated with the merged ZDR columns, suggesting that merged ZDR columns may be a proxy for updraft mergers and convective organization, which has been less emphasized in previous studies. Subsequently, the strongest updraft reached up to 17 km AMSL with a maximum w of greater than 20 m s^{-1} (Fig. 3.11d; x ~ 85 km), which was associated with the broaden enhanced ZDR region (Fig. 3.8d) and a large amount of hail and graupel (Fig. 3.10d). The merged ZDR columns exhibited a broader horizontal extent compared to the isolated ZDR columns. This broader enhanced ZDR region may suggest a wider updraft region, which could influence the microphysical pathways of ATS. Given the 12-minute RHI update interval, this interpretation should be regarded as tentative.

doi:10.6342/NTU202504233

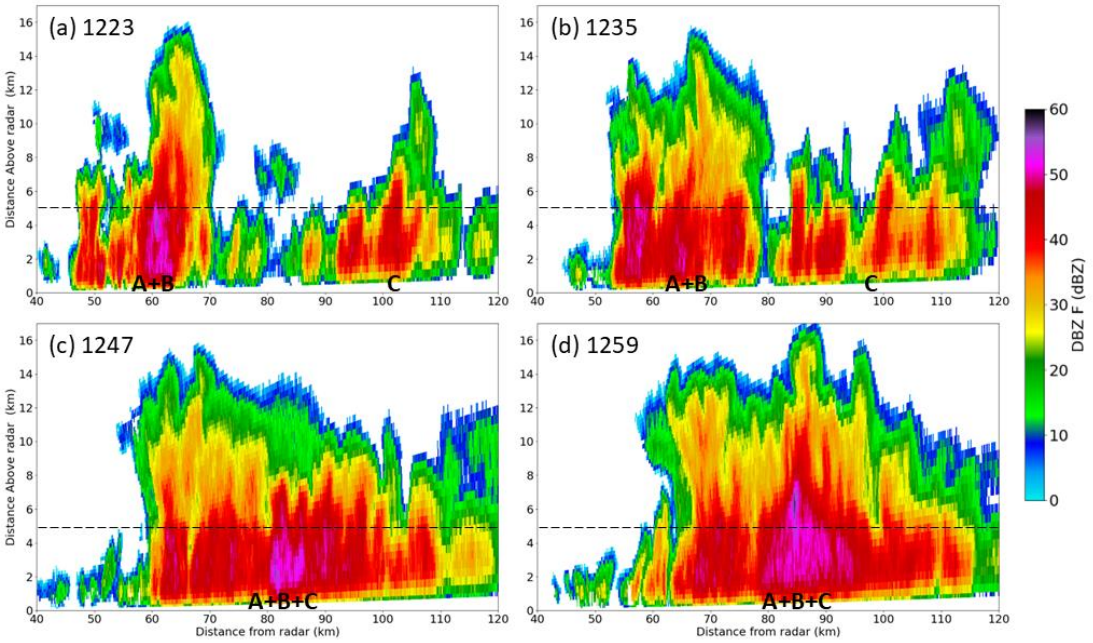

Figure 3.7. S-Pol range height indicator (azimuth angle 78°) of Z_H on 31 May 2022: (a) 1223, (b) 1235, (c) 1247, and (d) 1259 LST. The convective cells A+B, C, and A+B+C are labeled. The dashed line represents the environmental 0°C level.

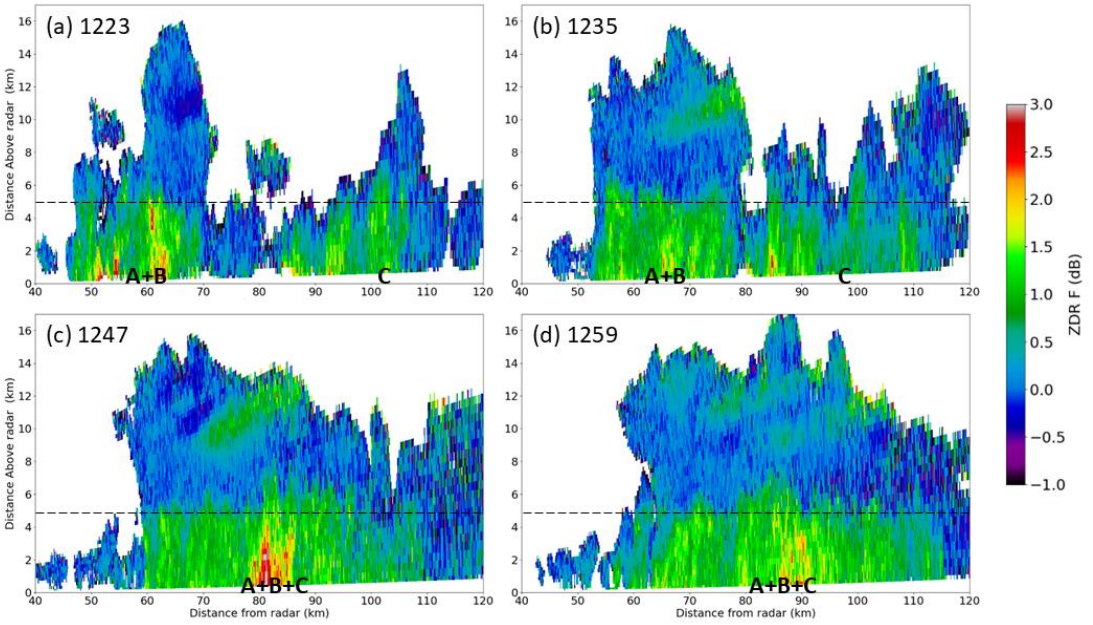

Figure 3.8. As Fig. 3.7, but for Z_{DR}.

doi:10.6342/NTU202504233

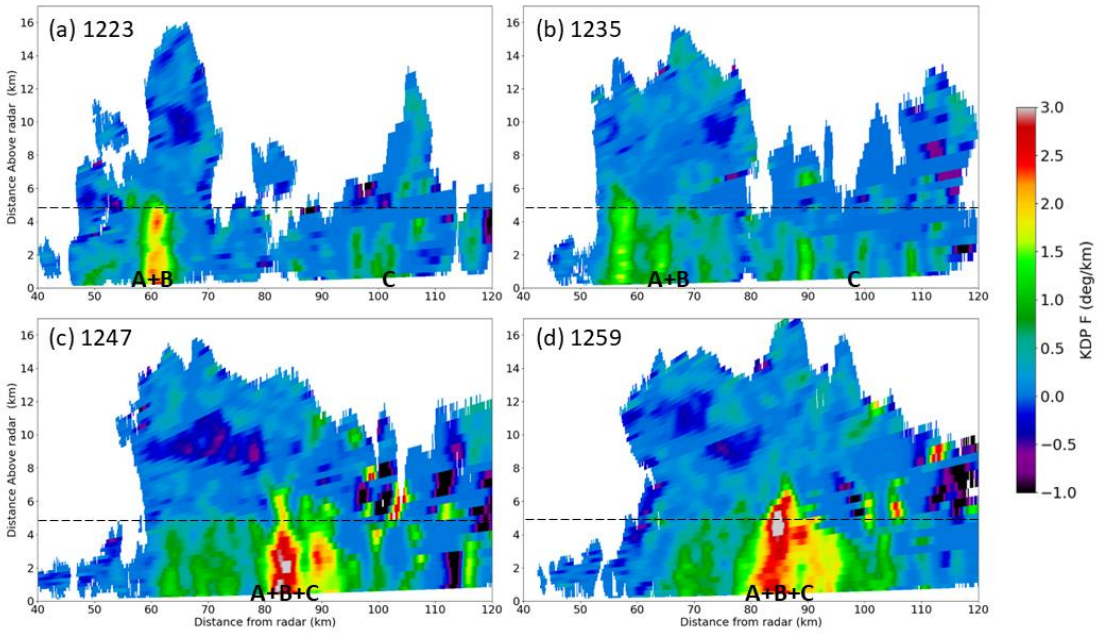

Figure 3.9. As Fig. 3.7, but for K_{DP}.

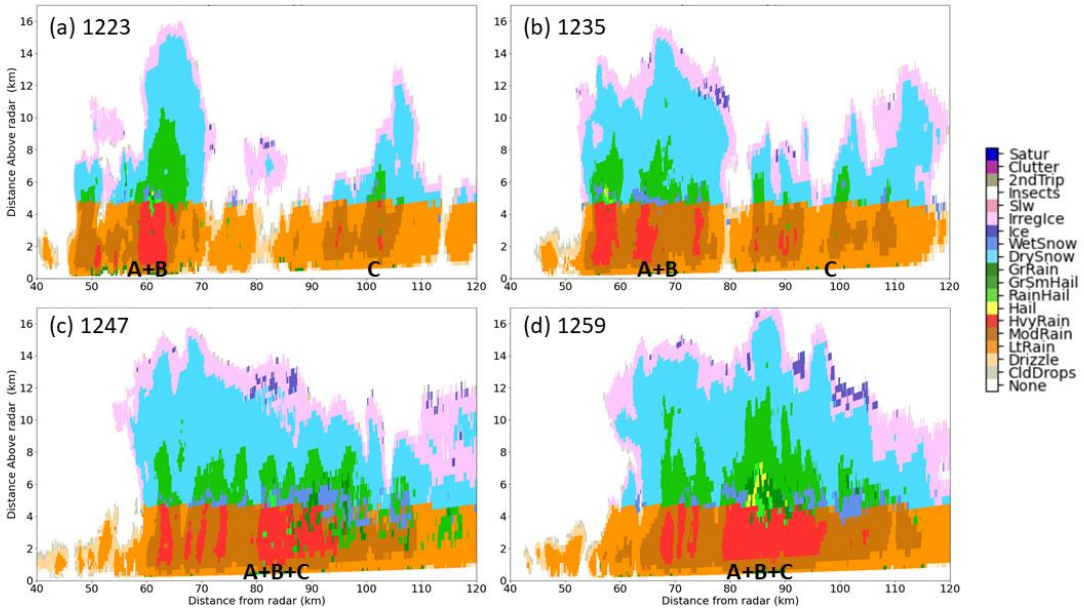

Figure 3.10. As Fig. 3.7, but for particle identification (PID).

doi:10.6342/NTU202504233

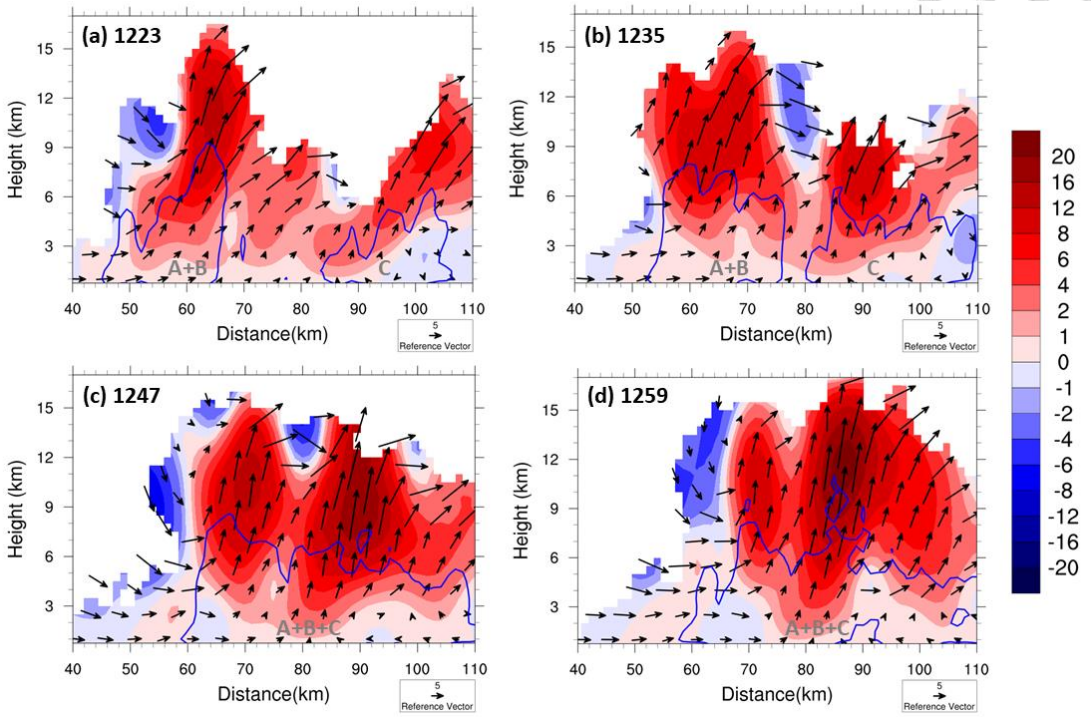

Figure 3.11. Evolution of retrieved winds (arrows) and vertical velocity (colored; in units of m s^{-1}) in cross-sections through the S-Pol 78° RHI: (a) 1223, (b) 1235, (c) 1247, and (d) 1259 LST. The radar reflectivity is contoured by blue lines at 35 dBZ. The convective cells A+B, C, and A+B+C are labeled.

3.4.2 Episode 2: Isolated convective cells

Figure 3.12 shows the evolution of ZH, ZDR, KDP, and PID in Episode 2. Convective cells in Episode 2 were more isolated and much weaker than those in Episode 1. The 20-dBZ echo top only reached 12 km AMSL in episode 2, while echo tops extended up to 16 km AMSL in Episode 1. At 1535 LST, the ATS system shows a multicellular structure (Fig. 3.12a). Subsequently, the isolated cells propagated eastward and the front side of the system (Fig. 3.12b, c; x = 100–125 km) gradually evolved into a stratiform region. The melting layer (~5 km AMSL) in the stratiform region was marked by a slight enhancement of ZDR and well-pronounced correlation coefficient (ρhv) minimum (not shown), although the ZH does not exhibit a clearly defined bright band.

doi:10.6342/NTU202504233

In contrast to the ATS in Episode 1, there were no well-defined ZDR columns in most scans during Episode 2, likely due to relatively weak updrafts (cf. Figs. 3.11 and 3.13). Accordingly, instead of graupel particles, there was a large amount of dry snow at mid-to-upper levels and wet snow near the melting level in Episode 2 (Fig. 3.12d, h, l). Compared to Episode 1, the area of heavy rainfall decreased noticeably in Episode 2, accompanied by much lower values of ZDR and KDP that might be due to the lack of large raindrops produced by melting hail and graupel.

In the absence of a cell and updraft merger, the updrafts showed a disorganized and slantwise structure with the maximum w of 8 m s^{-1} at 1535 LST (Fig. 3.13a). Meanwhile, the aforementioned easterly flow was located below 2 km AMSL (x ~ 90–125 km). An hour later, this easterly flow advanced westward to x ~ 75 km (Fig. 3.13c). It can be seen that the slantwise upward flow over the easterly flow weakened gradually and became downdrafts in the stratiform region.

doi:10.6342/NTU202504233

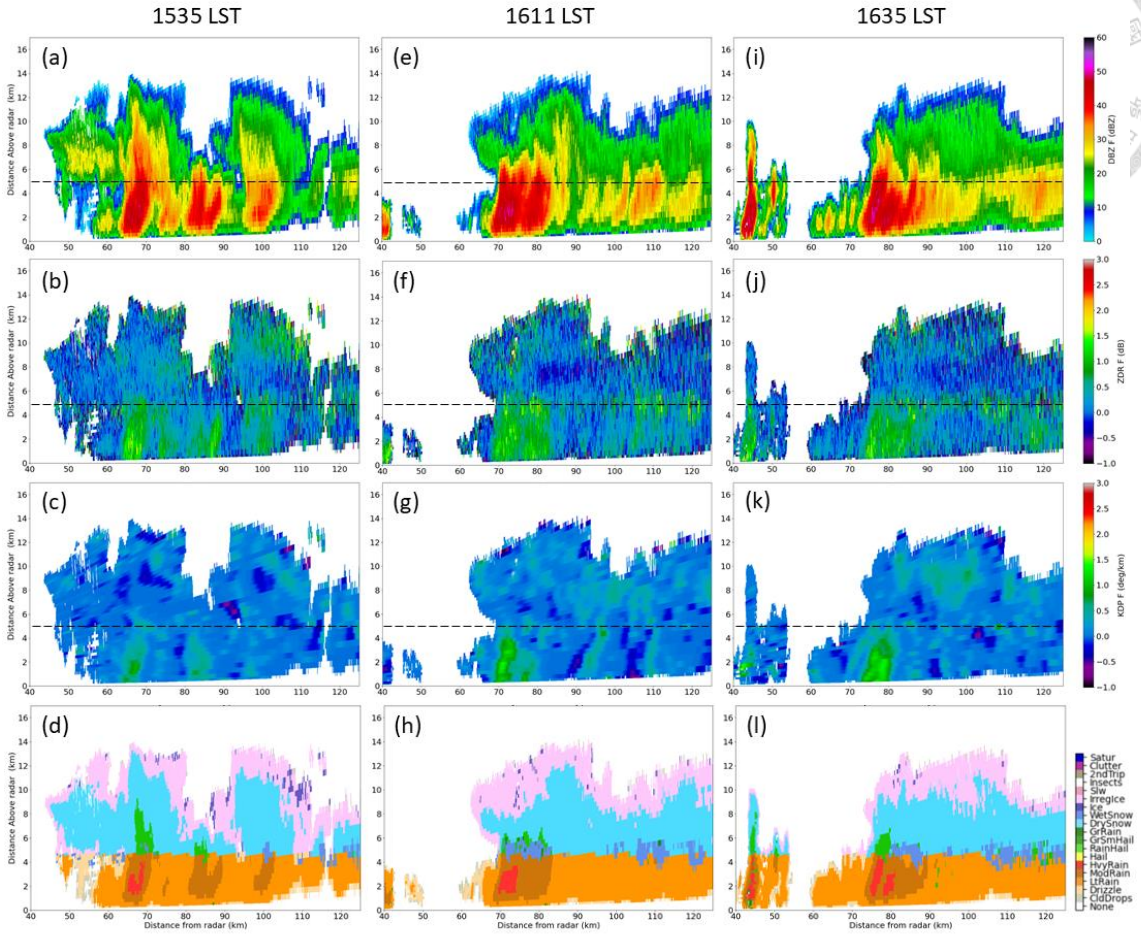

Figure 3.12. S-Pol range height indicator (azimuth angle 83°) of ZH, ZDR, KDP and PID on 31 May 2022: (a)(b)(c)(d) 1535 LST, (e)(f)(g)(h) 1611 LST, and (i)(j)(k)(l) 1635 LST.

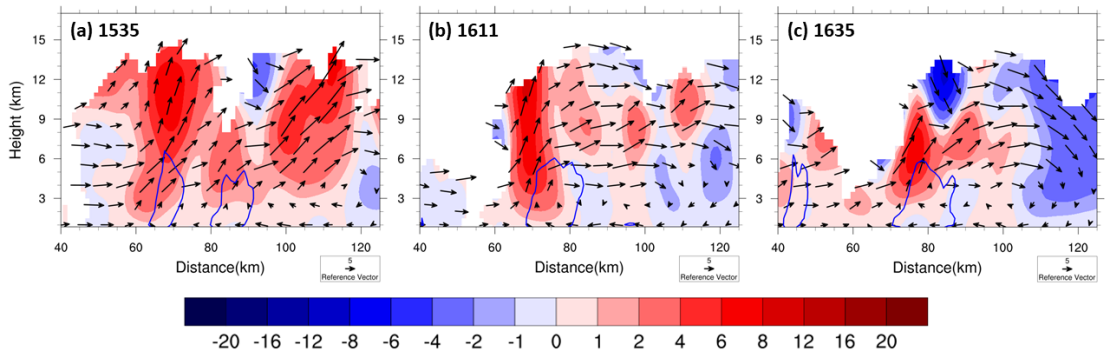

Figure 3.13. As Fig. 3.11, but for the cross-sections through the S-Pol 83° RHI: (a) 1535, (b) 1611, and (c) 1635 LST.

doi:10.6342/NTU202504233

3.4.3 Evolution of ZDR column and updraft

Thunderstorm updrafts are key areas for precipitation growth and electrification, making their accurate detection via radar data essential for assessing storm damage potential. Tracking the height of ZDR columns has been proposed for nowcasting thunderstorm evolution with lead times of 10–20 minutes (Snyder et al. 2015; Kuster et al. 2019). This study analyzes the temporal evolution of polarimetric signatures and updraft intensities to explore their relationship over complex terrain, while acknowledging that the 12-minute RHI update interval limits the ability to fully capture short-lived features.

Figure 3.14a,b show the time series of maximum height and width for the ZDR columns along S-Pol 78° RHI in Episode 1. Note that the width of the enhanced ZDR region (>1 dB) is computed at 5.5 km AMSL. Before the merger of cells A+B and C, the maximum height of ZDR columns was 6.0–6.5 km AMSL (~1.0–1.5 km above the 0°C level). It can be seen that the maximum height increased to 7.0 km AMSL around the merging time (1247 LST), indicating that the MCM process was accompanied by strong updrafts that lifted more supercooled water above the melting level (Fig. 3.11c). The maximum width of ZDR columns was ~4 km before cell merger. The width increased twofold to 8 km at the merging time, with an even broader width (~9.5 km) observed at 1311 LST, suggesting a wider updraft region. A temporary decrease in width occurred at 1259 LST, which might be attributed to the presence of hail (Kumjian et al. 2014). Afterward, the maximum width (height) of ZDR columns plummeted to ~0.5 km (5.5 km) at 1335 LST.

To investigate the relationship between ZDR columns and updraft intensity, Fig. 3.14c,d show the maximum w along the S-Pol 78° RHI and the maximum connected area of updrafts with $w > 4$ m s^{-1} at 5.5 km AMSL in Episode 1. Both updraft velocities

doi:10.6342/NTU202504233

and areas rose rapidly at the merging time. The maximum updraft speed (area) increased from 13 m s^{-1} (90 km^2) to 22 m s^{-1} (250 km^2) after the MCM. Note also that the updraft velocity and area followed a similar evolution, seemingly related to the width of the ZDR column. After the merger, the horizontal extent of updrafts enlarged. Thus, the updraft core might have been less likely to be impacted by environmental dry air entrainment, which maintained the positive buoyancy and lead to the intensification of the merged cell (Miao and Yang 2022).

In contrast to Episode 1, the convective cells were isolated, and no well-defined ZDR columns were observed in most scans during Episode 2 (Fig. 3.12 b,f,j). The maximum updraft speed (<10 m s^{-1}) in Episode 2 was much lower than that in Episode 1 (Fig. 3.14c,e). Moreover, the maximum updraft area (<100 km^2) was far smaller (Fig. 3.14d,f). These results suggest that convective organization in the MCM process plays a critical role in the development of ATSs over the SMR, although short-lived features might have gone undetected due to the 12-minute radar update time.

doi:10.6342/NTU202504233

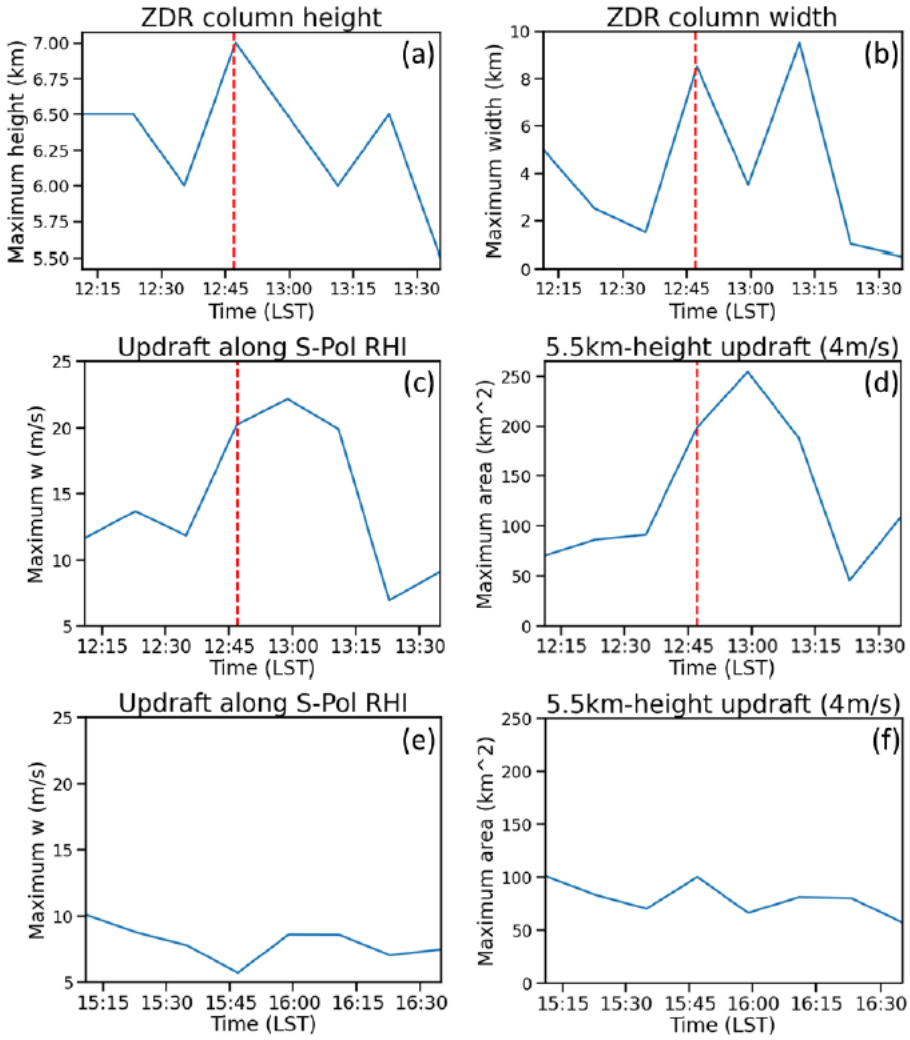

Figure 3.14. (a),(b),(c),(d) Evolution during Episode 1: (a) maximum height and (b) maximum width of the Z_{DR} columns along the S-Pol 78° RHI. (c) maximum retrieved vertical velocity w of the updrafts along the S-Pol 78° RHI. (d) The maximum connected area of updrafts (w > 4 m/s) which is calculated at the 5.5 km AMSL. The maximum width of ZDR columns is calculated at the 5.5 km AMSL. The time of merger of A+B and C is labeled as the red dashed lines. (e),(f) As (c),(d) except for Episode 2. Note that (e) is computed at S-Pol 83° RHI.

3.4.4 Evolution of microphysical processes

To further compare the bulk polarimetric features of the merged and isolated convective cells during Episodes 1 and 2, contoured frequency by altitude diagrams (CFADs; Yuter and Houze 1995) of ZH, ZDR, and KDP in the tracked convective areas are presented in Figs. 3.15 and 3.16. The maximum connected area of strong echo (> 40

doi:10.6342/NTU202504233

dBZ) at 1.5 km AMSL was tracked and the CFADs were computed within this area. First, we compare the vertical structure of polarimetric measurements in SCM (1224 LST) and MCM (1300 LST). The less intense and shallower convection in SCM had 1% of 35-dBZ reflectivity extending through 7.5 km AMSL (Fig. 3.15a). The MCM with more intense and deeper convection had 1% of 35-dBZ reflectivity up to 12 km AMSL (Fig. 3.15d). The mean ZH profile (Fig. 3.15a,d) indicates higher values in MCM than SCM throughout the low to upper levels.

The 0.1% frequency contour of 1.0-dB ZDR extended to higher levels (6.5 km; Fig. 3.15b) in MCM compared to SCM (6.0 km; Fig. 3.15e). Moreover, 0.1% of 1-deg/km KDP also reached higher levels (7.0 km; Fig. 3.15c) in MCM than SCM (6 km; Fig. 3.15f). These results indicate more supercooled liquid droplets were lofted by stronger updrafts in MCM, which can enhance the riming and electrification processes (Takahashi 1978; Kumjian and Ryzhkov 2008; Mattos et al. 2017). Note that the 0.1% threshold highlights rare but significant radar features linked to the most intense updrafts during storm mergers, providing insights into kinematic differences between SCM and MCM. At 8–12 km AMSL, the majority of ZDR values were centered at ~0 dB and showed no noticeable vertical variation for SCM. On the other hand, the upper-level distribution of ZDR shifted to larger values (~ 0.5 dB) and displayed a significant downward decrease of ZDR between 8 and 12 km for MCM, which might be due to a more active riming process (Kumjian et al. 2022) or depolarization effect by oriented crystals (Ryzhkov and Zrnic 2007). The downward increase of ZDR due to the melting of graupel was more pronounced near the 0°C level in MCM. Below the freezing level, the mean values of ZDR and KDP were higher in MCM, suggesting larger raindrops and higher rainwater content.

Secondly, we compare the profile of polarimetric variables between merged and

doi:10.6342/NTU202504233

isolated convection in Episodes 1 and 2, respectively. The 1% 35-dBZ reflectivity descended from 9 km to 7 km (Fig. 3.16a,d), suggesting the convection in Episode 2 weakened. In contrast to Episode 1, the heights of 0.1% 1-dB (deg km^{-1}) ZDR (KDP) were about 5 km or even lower (Fig. 3.16b,c,e,f), indicative of the much weaker updrafts in Episode 2 (Fig. 3.14). At 8–12 km, the major distribution (> 20%) of ZDR approached ~ 0 dB in Episode 2, suggesting no signal of active riming. At low levels, the mean value of ZDR (KDP) in Episode 2 was lower by ~17% (24%) than that in Episode 1, suggesting smaller raindrops and lower rainwater content.

Recent studies have utilized dual-polarization radar "fingerprints," specifically the vertical gradients of polarimetric variables, to infer dominant microphysical processes within storms (Kumjian et al. 2022). ZH and ZDR variations within the 1.5-km pure rain layer (1.5–3.0 km AMSL) provide insights into changes in raindrop size and number concentration, offering a way to infer dominant warm-rain processes such as coalescence, evaporation, size sorting, and breakup (Chen et al. 2019). Figure 3.17 illustrates the evolution of ZH and ZDR in this layer (1.5–3.0 km AMSL) over the strong echo (>40 dBZ) during Episodes 1 and 2. Each dot represents a radar volume scan, with color indicating the chronological order. Interestingly, the temporal evolution of the samples shows a distinct pathway from coalescence ($\Delta ZH > 0$ and $\Delta ZDR > 0$) to the evaporation/size sorting quadrant ($\Delta ZH < 0$ and $\Delta ZDR < 0$) during Episode 1 (Fig. 3.17a). The samples in the SCM fall in the coalescence-dominant quadrant, indicating the importance of the coalescence process at low levels. Afterward, samples in the MCM are located in the top left quadrant, indicating the significant role of evaporation and size sorting in the later stage of the merged ATS system. In contrast, most of the samples are located in the evaporation/size sorting regime during Episode 2 (Fig. 3.17b), indicating that evaporation processes are dominant at most of the time. Only few

doi:10.6342/NTU202504233

samples with low ΔZDR and low ΔZH fall in the coalescence quadrant, suggesting the limited coalescence process within isolated convection, which may be due to the weaker low-level convergence and updrafts in Episode 2.

In the tropical DYNAMO/ARM-AMIE dataset of S-Pol observations, most of the convection cases reveal fingerprints for coalescence and evaporation while many stratiform cases exhibit signatures of breakup, coalescence, and evaporation (Kumjian and Prat 2014). They further suggest that the initial ZDR aloft is the primary indicator of the subsequent behavior of the rain shaft. Specifically, drop size distributions (DSDs) characterized by smaller drops initially (i.e., smaller initial ZDR) tend to lead to increases in ZDR over the rain shaft. Our study indicates that coalescence and evaporation are the dominant warm-rain processes in this terrain-confined ATS case in TAHOPE/PRECIP IOP 2, which is consistent with the results from Kumjian and Prat (2014) on the oceanic convection.

doi:10.6342/NTU202504233

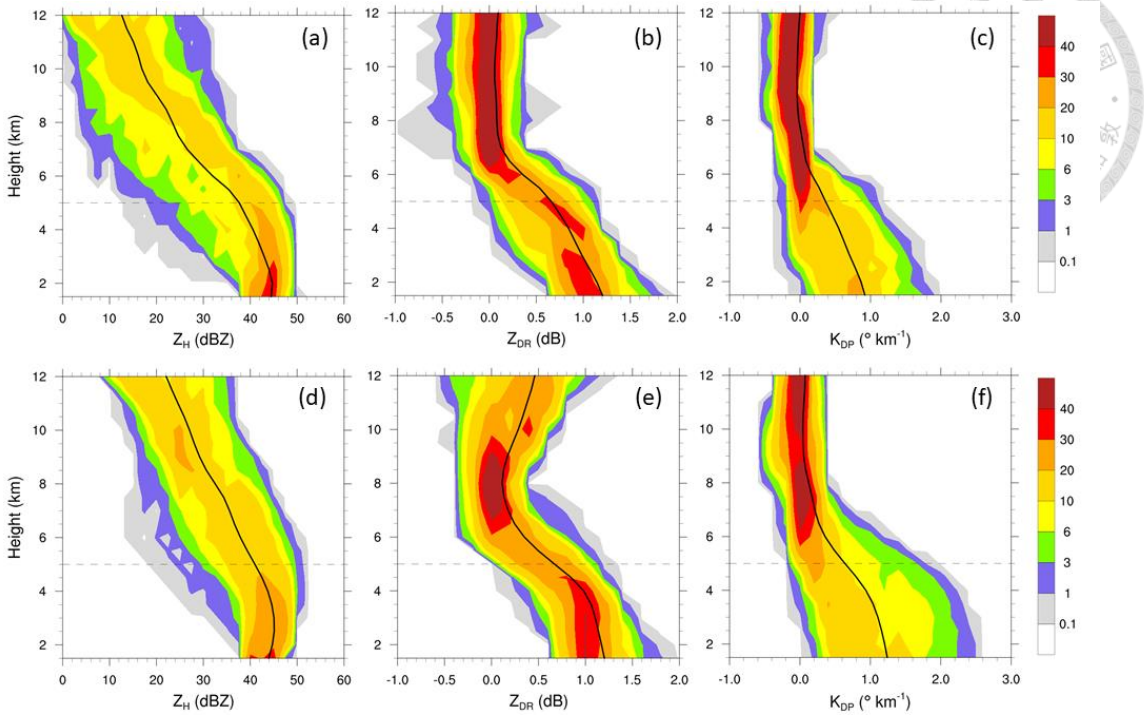

Figure 3.15. (a),(b),(c) CFADs (colored; in units of %) of (a) ZH, (b) ZDR, and (c) KDP within the 1.5-km-height strong echo region (>40 dBZ) over the Taipei Basin domain at 1224 LST. The CFAD percentages represent the relative frequency of each variable within a height bin, normalized by the total number of data points in that height bin. The mean profile is indicated as a black line in each panel. The environmental 0°C level is labeled as a dashed line. (d),(e),(f) As (a),(b),(c) except for 1300 LST. The CFADs are computed from the PPI scans of S-Pol.

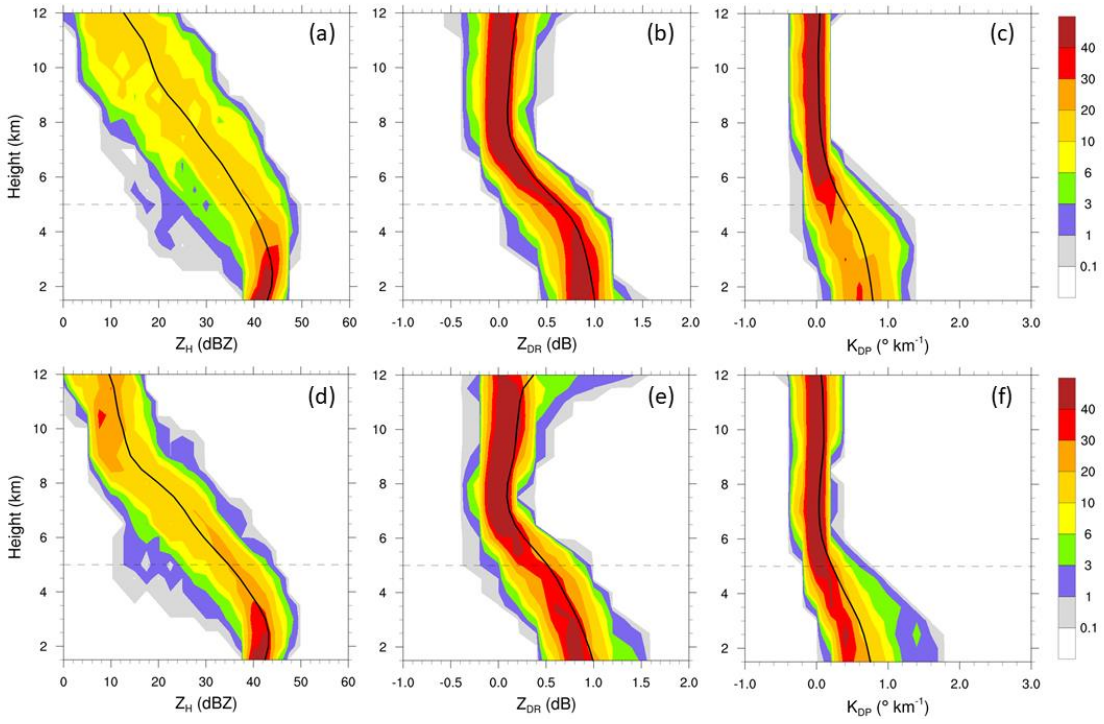

Figure 3.16. As Fig. 3.15, but for (a),(b),(c) 1524 LST and (d),(e),(f) 1612 LST.

doi:10.6342/NTU202504233

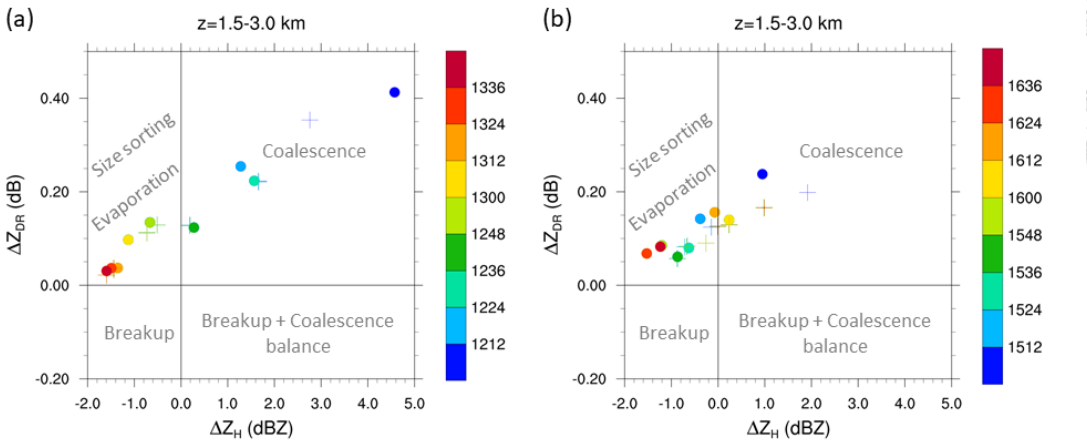

Figure 3.17. The change in ZDR as a function of the change in ZH from 3 to 1.5 km AMSL in the afternoon thunderstorms in the Eulerian (cross) and Lagrangian (circle) framework: (a) Episode 1 and (b) Episode 2. The microphysical processes represented by each quadrant are annotated. The colors of these symbols represent the observed time (LST).

3.5 Discussion and summary

This study investigates the microphysical and kinematic processes of severe afternoon thunderstorms (ATS) of the IOP 2 in TAHOPE/PRECIP field campaigns utilizing the high-quality S-Pol radar observations and the multi-Doppler winds retrieved by SAMURAI-TERRAIN. RHI observations from the S-Pol radar provided detailed insights into the microphysical and kinematical characteristics of deep convection that were unavailable from previous studies in northern Taiwan. Complete 3D retrieved winds are obtained using both PPI and RHI radar data, providing valuable information about the dynamics of the ATSs. This aids in the analyses of the interaction between convective cells over complex terrain in northern Taiwan. It was found that there were two episodes of severe ATSs over the SMR south of the Taipei Basin. The main morphologic difference between the storms was the multiple cell merger in Episode 1 and the isolated convective cells in Episode 2.

doi:10.6342/NTU202504233

In Episode 1, the physical mechanism of single cell merger (SCM; i.e., the merge of cells A and B) was likely rear-end collision due to different propagation speeds (Miao and Yang 2018), while the multiple cell merger (MCM; i.e., the merge of cells A+B and C) was favored by terrain-induced circulation. The low-level convergence produced by upslope winds favored the development and organization of ATSs over the SMR. Wind retrievals indicate that updrafts merged near the time of the MCM, followed by intensification with maximum w exceeding 20 m s^{-1}. Furthermore, the multi-merger convection had a large region of graupel/small hail extending up to 12 km AMSL. In summary, cloud microphysics in the multiple-merger cell transitioned to more active riming and melting processes, leading to heavy rainfall over the mountainous region.

In contrast, convective cells in Episode 2 were isolated and much weaker than in Episode 1. In the absence of cell and updraft merger processes, the relatively weak updrafts showed a disorganized and slantwise structure with a maximum w of ~ 10 m s^{-1}. Accordingly, instead of hail and graupel, there was a large amount of dry snow at mid-to-upper levels and wet snow near melting level in Episode 2. Compared to Episode 1, the area of heavy rainfall reduced noticeably in Episode 2, accompanied by much lower values of ZDR and KDP that might be due to the lack of large raindrops produced by melting of hail and graupel.

JJ23 investigated a severe ATS case on 14 June 2015 resulting in flash flooding in the Taipei metropolitan area, indicating that the development of convective cells from the foothill to the basin was favored by the enhanced low-level convergence produced by the downslope outflow boundary and sea breeze (Jou 1994; Miao and Yang 2020). In contrast to the 14 June 2015 case (see Fig. 5b in JJ23), the convection in this case was confined to the mountainous region (Fig. 3.4a), leading to extreme orographic rainfall over the SMR. Although the mechanism of cells A and B merger in this terrain-confined

doi:10.6342/NTU202504233

ATS system has been discussed in previous studies (Tao and Simpson 1989; Miao and Yang 2018), the subsequent A+B and C merger is closely related to the upslope wind. This finding provides a new insight into the cell merger mechanism that was not discussed in previous studies. The merging of cells A+B and C was preceded by a bridge of cumulus and congestus clouds, which was similar to the "cloud bridge" proposed by Tao and Simpson (1989) and might simply represent the importance of low-level convergence to the merging process. Notably, the low-level convergence region was parallel to the orientation of the SMR (Fig. 3.5c), implying the role of topography in convective organization. Furthermore, the cell separation distance before the MCM was ~ 30–40 km (Fig. 3.7a), which was longer than that in previous modeling (< 10 km; Table 1 in Stalker and Knupp 2003) and observational studies (e.g., ~ 15–20 km in JJ23; ~ 20 km in Wu et al. 2021). These results have highlighted the interesting possibility: *Low-level convergence resulting from terrain-induced circulation may provide a forcing mechanism for the formation of convective cells with a longer cell separation distance for cell mergers over mountainous regions*. It should be noted that some aspects of cell evolution in this study may have gone undetected due to the 12-minute RHI update interval, and future work with high-temporal-resolution observations and numerical experiments is needed to validate these mechanisms and their sensitivity to terrain geometry.

Thunderstorm updrafts are crucial for precipitation growth and electrification, making their accurate detection vital for assessing storm damage potential. Tracking ZDR column heights and areas has been suggested for nowcasting thunderstorm evolution (Snyder et al. 2015; Kuster et al. 2019; French and Kingfield 2021). This study investigates the relationship between ZDR column metrics and updraft intensities over the terrain near Taipei Basin. The high-resolution RHIs are utilized to measure the

doi:10.6342/NTU202504233

height and width of ZDR columns directly. While the 12-minute update time limits the ability to resolve rapid changes, these observations still provide valuable information on the connection between ZDR column width and updraft intensity/size in Taiwan's orographic convection.

In Episode 1, the observed maximum height of the ZDR column (7.0 km) occurred at the timing of the MCM and appeared to precede the observed highest updraft speeds by more than 10 min. Notably, the maximum width of ZDR columns increased twofold to 8 km at the merging time, consistent with the appearance of merged ZDR columns. After the MCM, a broader enhanced ZDR region (~9.5 km) was observed, associate with stronger updrafts (~22 m s^{-1}) and a larger updraft area (~250 km^2). In contrast, no well-defined ZDR columns were observed in most scans during Episode 2, and the observed maximum updraft speed (~10 m s^{-1}) and area (~100 km^2) in Episode 2 was much lower than in Episode 1.

The updraft velocity and area followed a similar evolution in Episode 1, seemingly related to the width of the enhanced ZDR region, highlighting that ZDR column width was a promising forecasting parameter for thunderstorm evolution and intensity. Furthermore, in northern Taiwan, merged ZDR columns may be a manifestation of the updraft merger process, suggesting less dilution of updraft buoyancy due to entrainment (Glenn and Krueger 2017; Miao and Yang 2022). Although previous research on thunderstorms over the Taipei Basin (e.g., JJ23) did not emphasize the broadening of the enhanced ZDR region during cell merger, this feature is discernible in their Fig. 8 and is consistent with our observations. These findings suggest that forecasting heavy rainfall in ATSs could benefit from considering the ZDR column width, especially when combined with other polarimetric radar signatures. Monitoring both the height and width of the enhanced ZDR region offers valuable insights into updraft characteristics

doi:10.6342/NTU202504233

and storm intensity, expanding its potential applications.

To further examine the relationship between the MCM, updraft intensity, and precipitation evolution, we also analyze two additional ATS cases presented in Appendix and develop a conceptual diagram of the MCM based on all three cases in northern Taiwan (Fig. 3.18). Across all three cases, a broadening of the enhanced ZDR region beyond 8 km at 5.5 km AMSL was observed during the MCM (Figs. 3.14b, A4b, A8b), despite the 12-minute RHI update time. The key time series characteristics from these cases are summarized in Table 3.1. The results indicate that the observed maximum vertical velocity following the MCM exceeded 22 m s^{-1} in all cases, with the highest reaching 27 m s^{-1} on 23 June. The time lag between the MCM and observed peak updraft velocity ranged from 12 to 36 minutes. The maximum 10-minute accumulated rainfall exceeded 24 mm in all cases, with the 23 June case reaching 35 mm. The peak precipitation occurred 23–47 minutes after the MCM. These findings suggest that the MCM, along with the broadening of the enhanced ZDR region (>8 km), tends to precede intense updrafts and heavy rainfall.

This work builds on recent studies that examined ZDR column size in different geographic settings, such as Kuster et al. (2019) and French and Kingfield (2021). While those studies focused on the relationship between ZDR column area and severe weather in the U.S., our research suggests that wide, merged ZDR columns may be relevant to severe storms over complex terrain in Taiwan, highlighting their potential utility as indicators of convective organization. However, this study is subject to limitations, particularly the 12-minute radar update interval, which introduces uncertainty when interpreting rapidly evolving convective features. Although our three case studies support the value of ZDR column width as a diagnostic metric, further validation is needed to assess its broader applicability. Future work will extend this

doi:10.6342/NTU202504233

analysis to the entire TAHOPE/PRECIP dataset to evaluate whether the ZDR column size reliably indicates storm intensification across a wider range of convective environments.

Table 3.1. Summary of key time series characteristics across three ATS cases, highlighting the relationship between multiple cell merger, updraft intensity, and precipitation evolution.

Case	Maximum Vertical Velocity (m/s)	Time Lag from Multiple Cell Merger to Peak Updraft (min)	Maximum 10-min Accumulated Rainfall (mm)	Time Lag from Multiple Cell Merger to Peak Rainfall (min)
0531	22	12	24.5	23–33
0623	27	36	35	47
0624	25	12	24.5	27

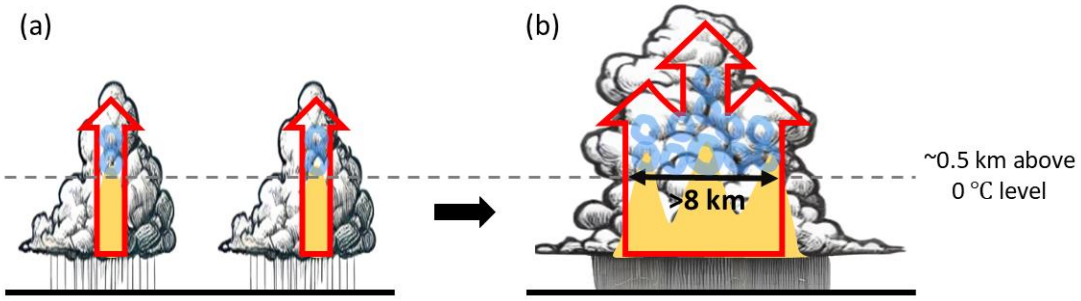

Figure 3.18. Conceptual diagram illustrating changes in ZDR column structure associated with multiple cell mergers. (a) Before the merger, individual convective cells contain distinct ZDR columns (yellow shading), each associated with localized updrafts (red arrows). (b) After multiple cell mergers, the updrafts merge, along with the development of a wide (>8 km) enhanced ZDR region (>1 dB) at 5.5 km altitude (~0.5 km above the environmental 0°C level). This structure indicates a larger, more organized updraft region with enhanced mixed-phased microphysical processes, including the lofting of graupel (blue circles) above the 0°C level.

doi:10.6342/NTU202504233

Chapter 4 Orographic Control on Strongly-Forced ATSs

4.1 Background

Terrain plays a significant role in modulating the diurnal cycle of moist convection and rainfall (Romatschke & Houze, 2010). During the warm season, mountainous regions exhibit pronounced day-night variations in convective activity (Kerns et al., 2010). The differential heating and cooling between mountains and adjacent plains, driven by the diurnal cycle of solar radiation, generate distinct local circulations that are critical for convection development. Additionally, the multiscale interactions among large-scale winds, thermally driven flows, and topographic effects further complicate the evolution of convection over mountainous region (Nair et al., 1997; Houze, 2012; Xu et al., 2012; Huang et al., 2019; Du et al., 2020; Li et al., 2021). For instance, Rasmussen and Houze (2012) demonstrated that the combination of synoptic-scale moisture transport and upslope flow strengthened mesoscale convective systems (MCSs), leading to a flash-flooding storm in the Himalayas. Similar physical mechanisms were observed in the Big Thompson Flood and Black Hills Flood in the Rocky Mountains, where persistent upslope transport of lowland moisture sustained intense convection (Maddox et al., 1978; Caracena et al. 1979).

Beyond the mechanical aspects of orographic lifting, these motions can destabilize the atmosphere by lifting moist and conditionally unstable air to saturation (Kirshbaum et al. 2018). This process can result in the formation of moist absolutely unstable layers (MAULs; Bryan & Fritsch 2000), where the lapse rate of a saturated layer exceeds the

doi:10.6342/NTU202504233

moist adiabatic lapse rate. Numerous observational and modeling studies (Table 4.1) have identified the presence of MAULs in a variety of storm environments across different geographic regions. Bryan and Fritsch (2000) and Mechem et al. (2002) highlighted MAULs within MCSs over the midlatitude United States and the tropical western Pacific, respectively. In both studies, MAULs extended horizontally for hundreds of kilometers along the axis of MCSs and vertically up to ~100 mb, primarily formed by mesoscale lifting induced by cold pools. Schumacher and Johnson (2008) similarly found deep (~1–2 km) MAULs in flash-flood-producing MCSs, associated with mesoscale convective vortices. Zou et al. (2023) found MAULs within a narrow cold frontal rainband associated with an atmospheric river in California, driven by large-scale frontal convergence.

Recently, MAULs have been reported in several heavy rainfall events in East Asia. Choi et al. (2011) found deep (~200 mb) MAULs aligned along linear MCSs in Korean Peninsula, maintained by strong vertical motions due to low-level jets. Takemi and Unuma (2020) analyzed Typhoon Hagibis (2019) and identified MAULs over 2 km deep in the eastern part of Japan, associated with abundant moisture and the circulation of the typhoon. Tsuji et al. (2021) examined moisture transport in heavy rainfall events in western Japan and found that MAUL was present in the mid-to-lower troposphere around peak precipitation, occurring more frequently during intense rainfall. Hua et al. (2020) examined a heavy rainfall event in the mountainous region of North China and revealed shallow MAULs (<1 km) generated by orographic gravity wave.

While the mechanisms for MAUL formation vary—including cold pools, low-level jets, mesoscale convective vortices, fronts and orographic gravity waves—they share a common feature: dynamically driven mesoscale ascent that cools the air layer to saturation. Notably, Hua et al. (2020) suggested that terrain could induce MAUL, stating

doi:10.6342/NTU202504233

that persistent upward motion associated with orographic gravity waves could sustain the MAUL. Takemi and Unuma (2020) indicated that MAULs, under highly humid conditions, characterize the thermodynamic environment for extreme rainfall during Typhoon Hagibis (2019). While their study did not explicitly attribute MAUL formation to orographic lifting, the combination of typhoon-induced moisture transport and terrain-forced ascent may have contributed to its development.

Despite the increasing recognition of MAUL as a critical factor in extreme precipitation, no prior studies have examined its occurrence in Taiwan's heavy rainfall events. This knowledge gap is particularly surprising given Taiwan's humid subtropical environment, which is often conducive to deep convection. This study seeks to address this gap by investigating whether complex terrain can induce MAUL formation and subsequently enhance extreme orographic rainfall during the TAHOPE/PRECIP IOP 2. The main objective is to identify the physical processes through which terrain contributes to MAUL development. In addition, the relationship between MAUL and heavy rainfall will be explored.

doi:10.6342/NTU202504233

Table 4.1. Summary of documented MAUL-related events in previous studies.

Reference	Storm type and region	MAUL horizontal/vertical scale	MAUL formation mechanism
Bryan and Fritsch (2000, BAMS)	Midlatitude MCSs over the United States	O(100 km) along MCS axis; O(10 km) across; ~100 mb deep	Mesoscale layer lifting by cold pool
Mechem et al. (2002, QJRMS)	MCSs over western tropical Pacific warm pool	Similar to Bryan and Fritsch (2000)	Mesoscale layer lifting by cold pool
Schumacher and Johnson (2008, MWR)	MCS producing flash flooding over eastern Missouri	O(100 km); 1–2 km deep	Lifting by mesoscale convective vortex
Choi et al. (2011, APJAS)	Linear MCS in central Korean Peninsula	O(100 km) along MCS axis; O(10 km) across; ~200 mb deep	Strong vertical motion due to low-level jet
Takemi and Unuma (2020, SOLA)	Typhoon Hagibis (2019) over eastern Japan	O(100 km); >2 km deep	Moisture and circulation associated with typhoon
Hua et al. (2020, JGR)	Convective system in mountainous North China	O(10 km); <1 km deep	Weak (<1 m s^{-1}) orographic gravity wave ascent
Tsuji et al. (2021, GRL)	MCS in western Japan	O(10 km); 800–500 hPa	Not investigated
Zou et al. (2023, JGR)	Cold frontal rainband in California	O(10 km) wide; ~850–700 hPa	Large-scale convergence in frontal zone

4.2 Numerical model and experimental design

4.2.1 Model configuration and validation

This study employs the Advanced Research version of the Weather Research and

doi:10.6342/NTU202504233

Forecasting (WRF-ARW) Model, version 4.5.2 (Skamarock et al. 2019), to simulate the extreme rainfall event during TAHOPE/PRECIP IOP 2. A two-way nested domain configuration is used, consisting of three domains with horizontal grid spacings of 13.5 km, 4.5 km, and 1.5 km (Fig. 4.1), respectively. The model uses 55 vertically stretched levels and a model top at 20 hPa. The outermost domain uses a time step of 15 seconds. The simulation period spans from 1200 UTC 30 May to 1200 UTC 31 May 2022. Model outputs at interval of 10 min are used for analysis, except for the trajectory analysis, which utilizes 5-minute output data.

The physical parameterizations follow the configuration in Miao and Yang (2022), including the Kain–Fritsch cumulus scheme (Kain and Fritsch, 1993) applied only to the outermost domain, the WDM6 microphysics scheme (Lim and Hong, 2010), the Rapid Radiative Transfer Model (RRTM) for longwave radiation (Mlawer et al., 1997), the Dudhia (1989) scheme for shortwave radiation, and the Yonsei University (YSU) planetary boundary layer scheme (Hong and Pan, 1996). Initial and lateral boundary conditions are provided by the NCEP Final (FNL) Operational Global Analysis data, available every 6 hours with a horizontal resolution of 0.25°.

Note that we conducted a series of sensitivity tests by varying the microphysics schemes and initial and boundary conditions. Among these, the aforementioned configuration produced the most realistic simulation of the event and is designated as the control (CNTL) run in this study.

The CNTL simulation demonstrates reasonable skill in capturing the synoptic to mesoscale environment of the 31 May 2022 event. It reproduces the moist region (relative humidity >70%) near northern Taiwan at 700 hPa (cf. Figs. 3.2a and 4.2a). The simulation also captures the low-level southwesterly flow advecting high-θ_e air toward Taiwan, the formation of a leeside low northeast of the island, and the position of the

doi:10.6342/NTU202504233

surface front offshore of northern Taiwan (cf. Figs. 3.2b–d and 4.2b–d). While CNTL underestimates the light rainfall along the western coast, it successfully captures the heavy rainfall over the northern mountainous region and the eastern coastal area (cf. Figs. 3.2e and 4.3a). In addition, the simulated convective evolution over the terrain agrees well with observations (cf. Figs. 4.4 and 4.5), reproducing the two distinct convective episodes and the confinement of strong reflectivity over the SMR.

These results indicate that CNTL captures the key features of the event, providing a reliable framework for investigating the role of terrain in MAUL formation and extreme orographic rainfall. To further examine the effects of terrain, a sensitivity experiment without Taiwan's topography (NTER) was also conducted, using identical model configurations as CNTL.

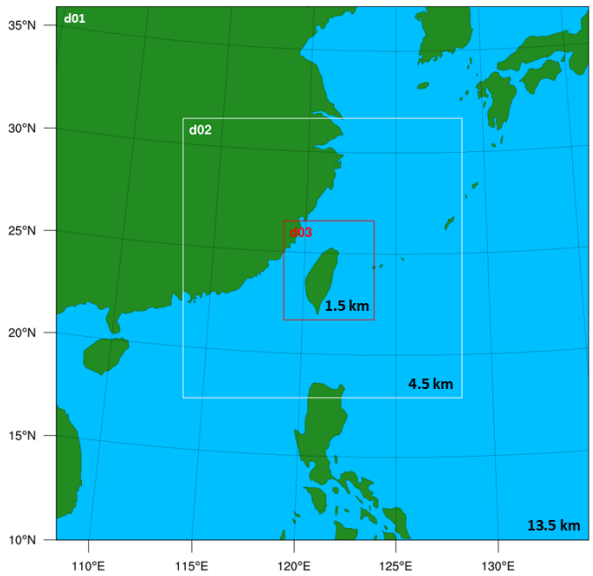

Figure 4.1. Three nested domains (with horizontal grid sizes of 13.5, 4.5, and 1.5 km) of the WRF model.

doi:10.6342/NTU202504233

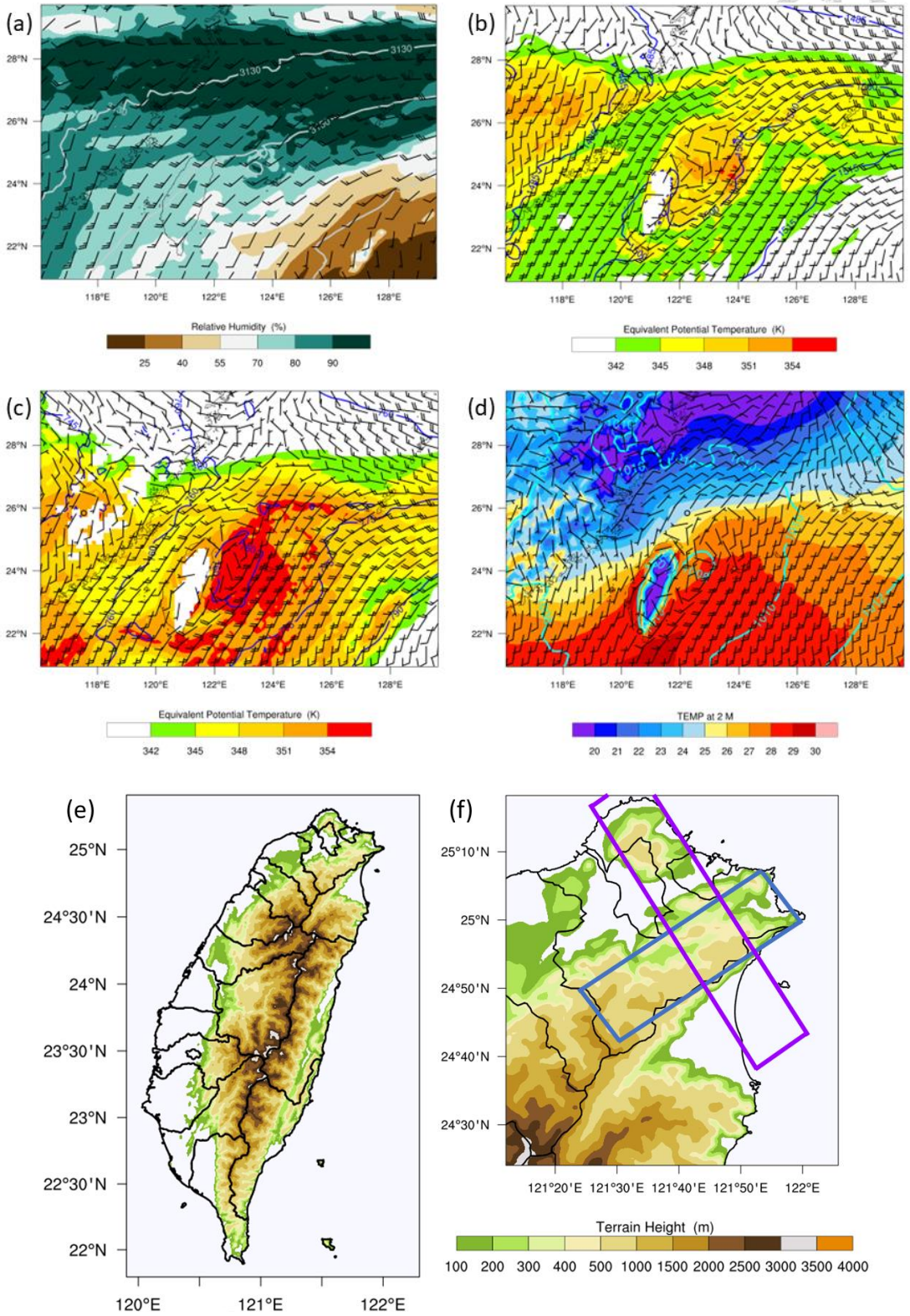

Figure 4.2. Simulated mesoscale environment at 0000 UTC (0800 LST) 31 May 2022: (a) 700-hPa map with the geopotential height (contours), relative humidity (colored), and horizontal wind (barbs; full barb is 10 kt, half barb is 5 kt); (b) As in (a), but for 850-hPa map with equivalent potential temperature (colored); (c) As in (b), but for

doi:10.6342/NTU202504233

925-hPa; (d) surface map with the mean sea level pressure (contours), 2-m temperature (colored), and horizontal wind. (e) Terrain height (colored) of Taiwan. (f) Terrain height (colored) of northern Taiwan. The blue box marks the location of the northeast–southwest cross section along the SMR. The purple box marks the location of the northwest–southeast cross section across the SMR.

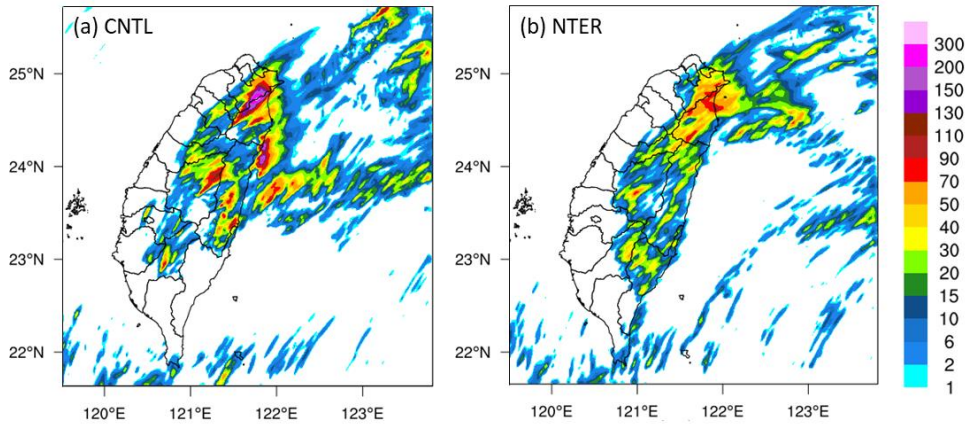

Figure 4.3. 0800–2000 LST accumulated rainfall (in units of mm) from (a) CNTL and (b) NTER experiments.

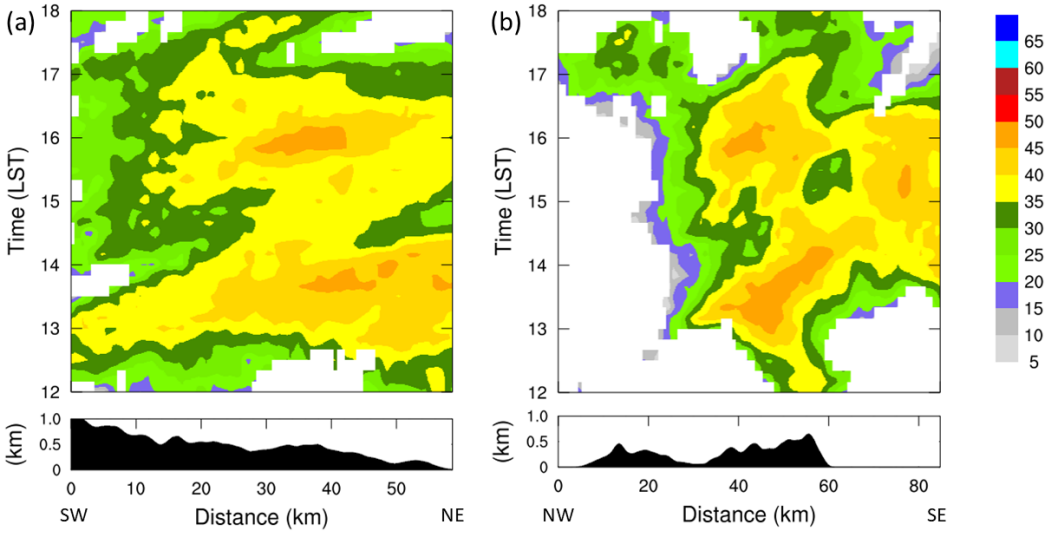

Figure 4.4. (a) Hovmöller diagrams of column-maximum radar reflectivity from QPESUMS (colored; in units of dBZ) along the NE–SW direction of the blue box in Fig. 4.2f. (b) As in (a), but along the NW–SE direction of the purple box in Fig. 4.2f. The averaged topography profile is shown by black shading.

doi:10.6342/NTU202504233

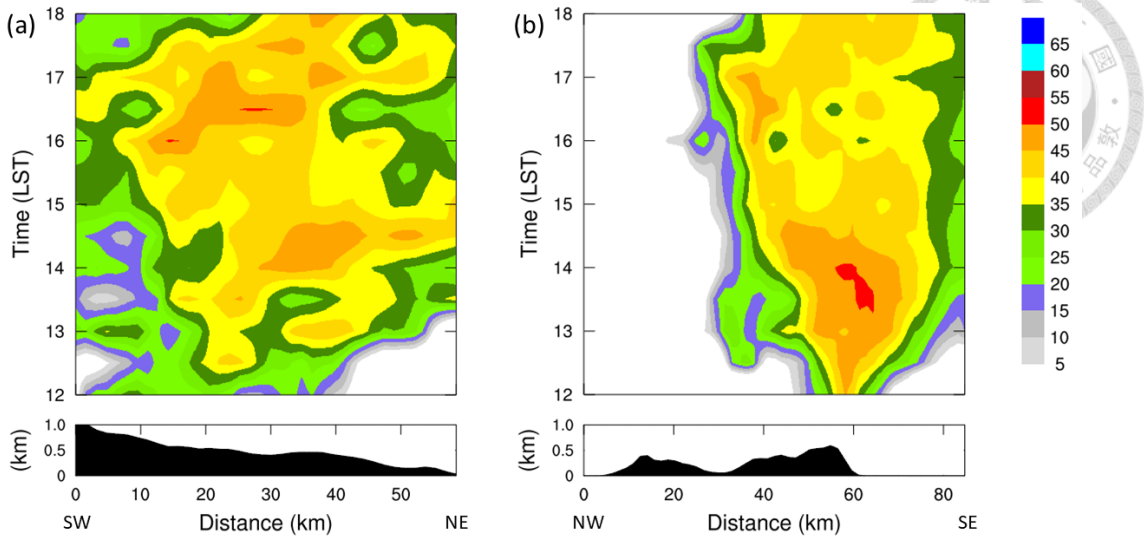

Figure 4.5. (a) Hovmöller diagrams of simulated column-maximum radar reflectivity (colored; in units of dBZ) along the NE–SW direction of the blue box in Fig. 4.2f. (b) As in (a), but along the NW–SE direction of the purple box in Fig. 4.2f. The averaged topography profile is shown by black shading.

4.2.2 Moisture flux convergence (MFC)

MFC is a widely used diagnostic for evaluating the atmospheric conditions favorable for convective initiation and development (Banacos and Schultz 2005; Rasmussen and Houze 2016). Following Banacos and Schultz (2005), MFC is expressed as the sum of the moisture advection and convergence terms:

$$\mathrm{MFC} = -u\frac{\partial q}{\partial x} - v\frac{\partial q}{\partial y} - q\left(\frac{\partial u}{\partial x} + \frac{\partial v}{\partial y}\right), \tag{4.1}$$

where u and v represent the zonal and meridional wind components, and q denotes specific humidity. The first two terms correspond to the horizontal advection of moisture, and the third term represents moisture convergence.

In this study, we calculate vertically integrated MFC over the 0–3 km AMSL. The MFC is decomposed into the advection term and convergence term to evaluate their relative contributions to the total moisture flux convergence. All MFC calculations are

doi:10.6342/NTU202504233

performed at a 10-minute temporal resolution using the 1.5-km domain output. Spatial averages are computed over the northern Taiwan domain to facilitate comparison between experiments.

4.2.3 Moist absolutely unstable layer (MAUL)

Following Takemi and Unuma (2020), the MAUL condition is defined as

$$\partial\theta_e/\partial z < 0 \text{ and } RH > 99\% , \quad (4.2)$$

where θ_e is the equivalent potential temperature and RH is the relative humidity. The MAUL volume is calculated by multiplying the vertical thickness of MAULs at each grid column by the horizontal area of regions where the MAUL thickness exceeds 0.5 km. This threshold excludes shallow layers and emphasizes regions with physically meaningful instability.

In practice, we first identify all vertical layers that meet MAUL criteria, and then retain only those contiguous MAUL segments that span at least three consecutive vertical levels, in order to exclude shallow layers. For each column, we sum the vertical thicknesses of all qualifying segments to obtain the MAUL depth. Finally, we multiply the MAUL depth (>500 m) by the horizontal grid area and sum over the domain to compute the total MAUL volume.

4.3 Results

4.3.1 Terrain enhanced MFC and induced MAUL over northern Taiwan

Figure 4.3 shows that the CNTL simulation reasonably captures the extreme rainfall over northern Taiwan, with the maximum accumulation (~200 mm) occurring along the SMR—the focus region of this study. In addition, CNTL also reproduces the

doi:10.6342/NTU202504233

heavy rainfall along the eastern coastal region. In contrast, the NTER experiment simulates weaker rainfall over northern Taiwan, with a markedly lower maximum (~90 mm), and significantly reduced coastal rainfall.

A key question is how terrain influences the development of this extreme orographic rainfall event under the prevailing southwesterly monsoon flow. The CNTL simulation shows strong low-level moisture flux over northern Taiwan (Fig. 4.6; peak values ~320 g kg^{-1} m s^{-1}). Located within the wake region of the southwesterly monsoon flow, northern Taiwan experiences enhanced moisture transport where the wake flow interacts with sea breeze and upslope winds (Figs. 4.6 and 4.7), channeling moisture toward the SMR. In contrast, the NTER experiment simulates moderate moisture flux (~240 g kg^{-1} m s^{-1}) on the southwestern windward slopes, but much weaker transport over northern Taiwan (~160 g kg^{-1} m s^{-1}). Notably, CNTL captures a convergence line offshore of eastern Taiwan, with intensified moisture flux along its southern flank, while NTER fails to reproduce this feature and shows considerably weaker flux in the same region. These differences underscore the critical role of terrain in redistributing and intensifying moisture transport under a southwesterly monsoon regime.

Radar reflectivity (Fig. 4.8) shows that low-level convergence associated with upslope flow develops along the SMR, supporting convection development and confining strong convection over the terrain, consistent with the observational findings of Miao et al. (2025). In NTER, the southwesterly monsoon flow penetrates into northern Taiwan, and once convection forms, it rapidly moves southeastward.

Radar reflectivity Hovmöller diagrams (Fig. 4.9) illustrate the evolution of convection along a northwest–southeast cross section over northern Taiwan. In CNTL (Fig. 4.9a), intense reflectivity exceeding 40 dBZ persists over the Snow Mountain

doi:10.6342/NTU202504233

Range (SMR) throughout 12-18 LST. A strong convective burst occurs between 1200 and 1400 LST, producing a period of high-intensity rainfall. Overall, the reflectivity pattern in CNTL exhibits a relatively stationary structure, collocated with sustained moisture flux convergence (MFC) over the mountainous region. In contrast, convection in NTER (Fig. 4.9b) initiates later than in CNTL and, once developed, rapidly propagates southeastward toward the ocean. The absence of terrain in NTER leads to more transient convection with fast propagation, highlighting the role of orography in maintaining localized, persistent deep convection over the SMR.

To quantify the terrain's impact on MFC, Table 4.2 presents the time-averaged, vertically integrated (0–3 km AMSL) MFC over northern Taiwan. The CNTL run exhibits a value of 44.5×10^4 kg s^{-1} m^{-2}, approximately 18% higher than NTER (37.8×10^4 kg s^{-1} m^{-2}), with both simulations showing dominance of the convergence term. This result indicates the role of terrain in enhancing low-level moisture accumulation and promoting a more humid environment over northern Taiwan (Fig. 4.10).

To examine the convective structure, Figures 4.11 and 4.12 present vertical cross sections of simulated radar reflectivity and equivalent potential temperature (θ_e) along a southeast–northwest transect. In the CNTL simulation (Fig. 4.11, upper row), convection initiates over the SMR by 1200 LST and rapidly intensifies, with 40 dBZ reflectivity extending upward to 9–10 km by 1300–1400 LST. This convective structure is associated with persistent upslope flow and strong updrafts (w >6 m s^{-1}). The ascending inflow forms a ~2-km-deep layer of θ_e >352 K (Fig. 4.12, upper row), associated with the development of MAULs (regions with $d\theta_e/dz < 0$ and RH > 99%) over the slope region. These MAULs are pronounced during 1300–1400 LST and accompanied by the intense convection and updrafts. The CNTL simulation exhibits features similar with the MAUL conceptual model proposed by Bryan and Fritsch (2000;

doi:10.6342/NTU202504233

their Fig. 5), including a potentially unstable environment in the mid-to-lower troposphere, the presence of MAULs near the inflow region, and the intrusion of descending low-θ_e air from the opposite side of the inflow into the convection.

In contrast, NTER shows markedly shallower convection (Fig. 4.11, bottom row), with 40-dBZ reflectivity reaching only 4 km height and weaker updrafts. The θ_e structure in NTER (Fig. 4.12, bottom row) indicates a thinner layer of inflow (~1 km). MAULs are also less extensive in NTER, both in vertical depth and horizontal coverage, suggesting that the absence of terrain suppresses the formation of deep and broad MAULs.

Previous research on MAULs suggests that these unstable layers are often associated with layer-lifting inflow signal (Bryan & Fritsch 2000; Mechem et al. 2002). To further examine the impact of topography on the nature of inflow ascent, Fig. 4.13 shows 60-minute forward trajectories initialized at 1300 LST. In CNTL, tracers originating from the basin are lifted upslope as a coherent layer, with most tracers reaching the upper level. In contrast, NTER exhibits a parcel-based ascent pattern, where only near-surface tracers are lifted, and the majority remain below 5 km. These results suggest that terrain facilitates layer lifting conducive to MAUL formation and promotes the development of deep convection.

doi:10.6342/NTU202504233

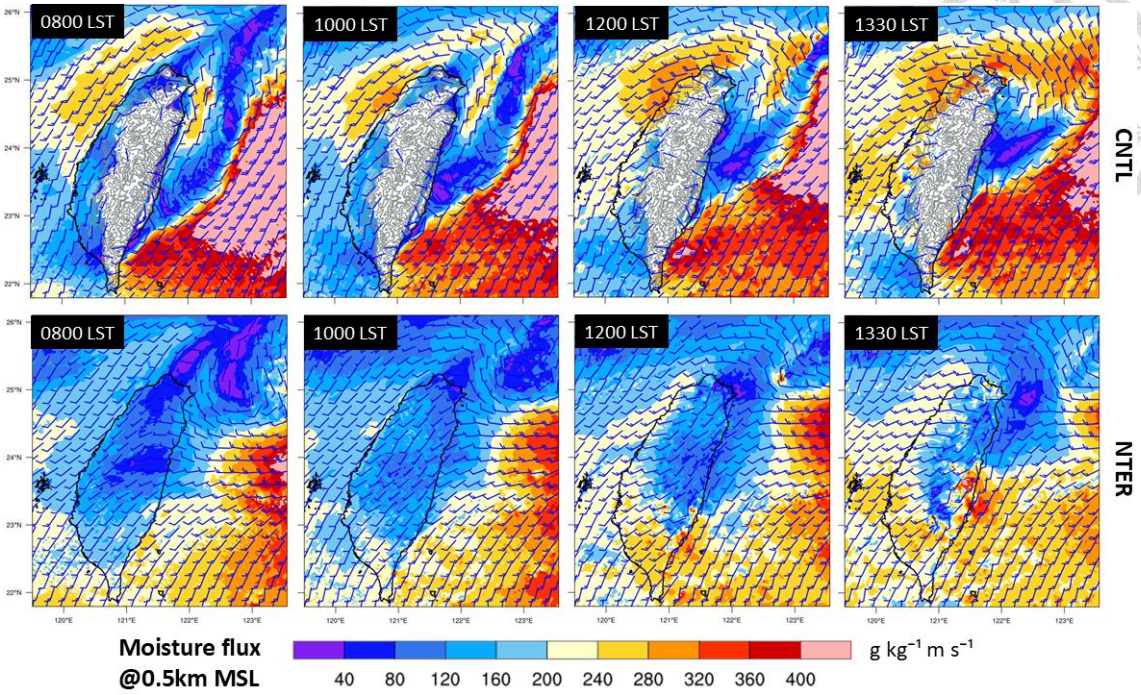

Figure 4.6. Horizontal cross sections of 0.5-km water vapor flux (colored; unit: g kg^{-1} m s^{-1}) and 0.5-km horizontal wind (barbs; full barb is 10 kt, half barb is 5 kt) from CNTL (top row) and NTER (bottom row) experiments. The time in LST is indicated at the upper-left corner in each panel. Black line is for the terrain height.

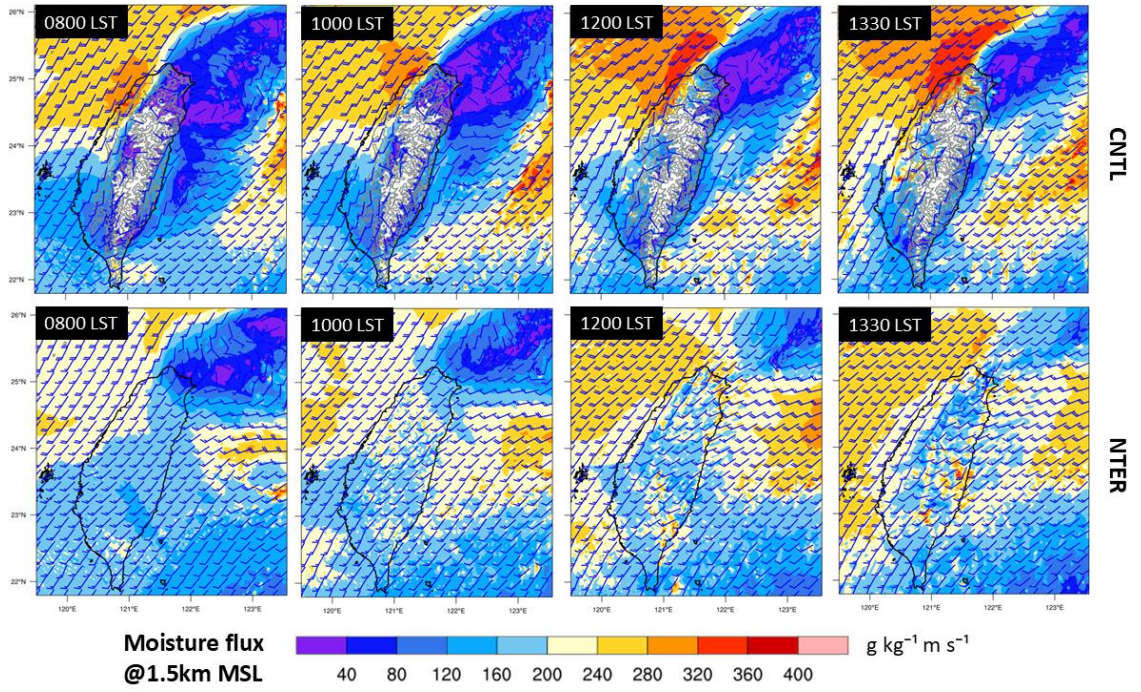

Figure 4.7. As in Fig. 4.6, but for 1.5-km water vapor flux and horizontal wind.

doi:10.6342/NTU202504233

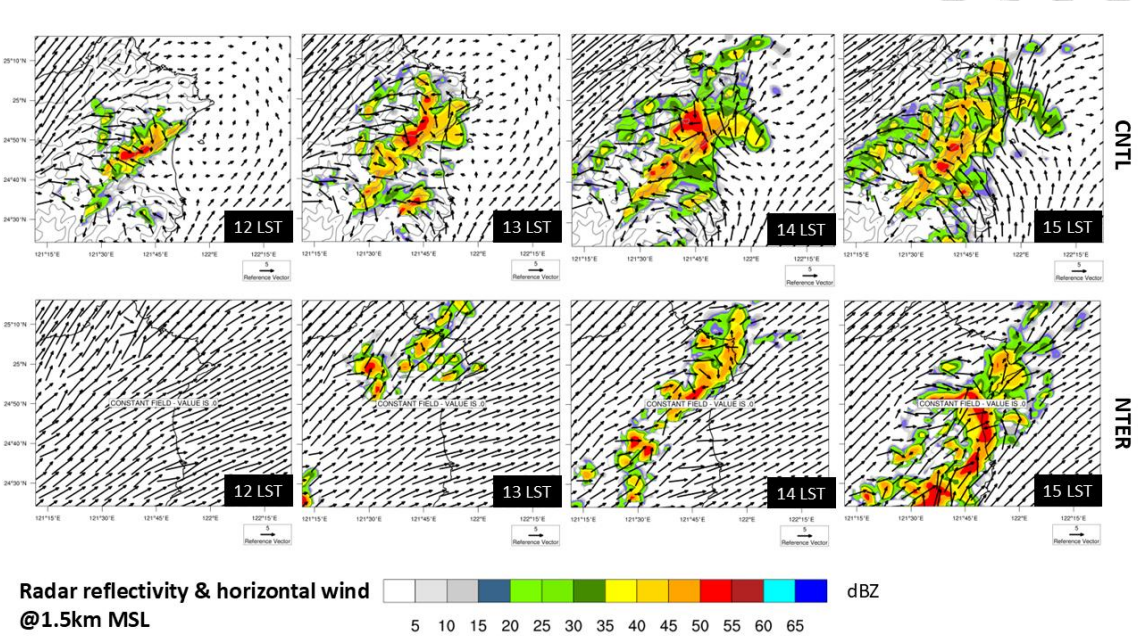

Figure 4.8. Horizontal cross sections of 1.5-km radar reflectivity (colored; unit: dBZ) and horizontal wind from CNTL (top row) and NTER (bottom row) experiments. The time in LST is indicated at the lower-right corner in each panel. Black line is for the terrain height.

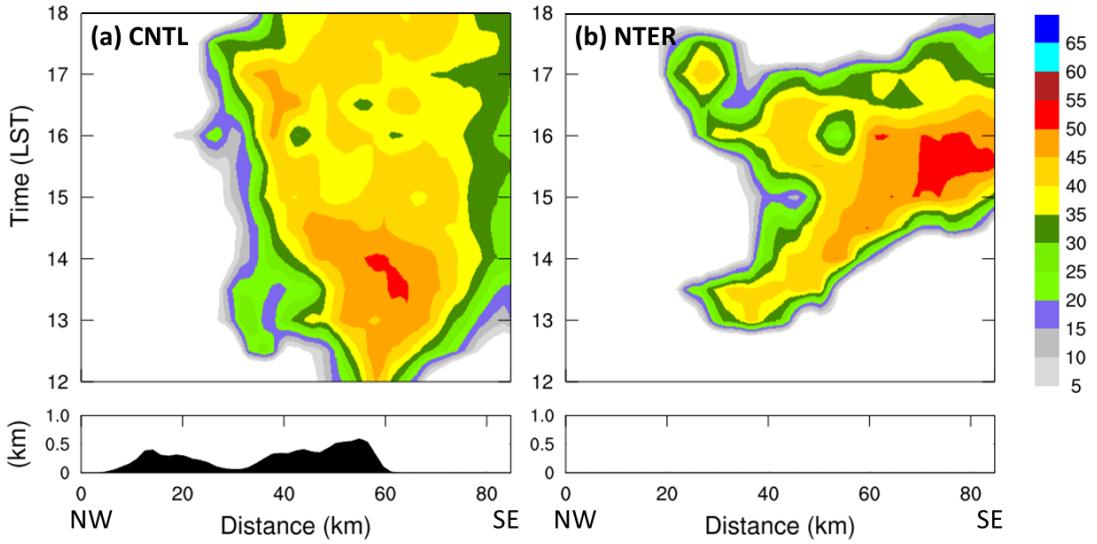

Figure 4.9. Hovmöller diagrams of simulated column-maximum radar reflectivity (colored; in units of dBZ) along the NW–SE direction of the purple box in Fig. 4.2f: (a) CNTL; (b) NTER experiment. The averaged topography profile is shown by black shading.

doi:10.6342/NTU202504233

Table 4.2. Time-averaged vertically (0-3 km MSL) integrated moisture flux convergence (10^4 kg $s^{-1}m^{-2}$) in each simulation in the northern Taiwan domain. All values are averaged from hours 12–24 of each simulation.

Exp.	MFC	MFC_{conv}	MFC_{adv}
CNTL	44.5	44.4	0.1
NTER	37.8	34.5	3.3

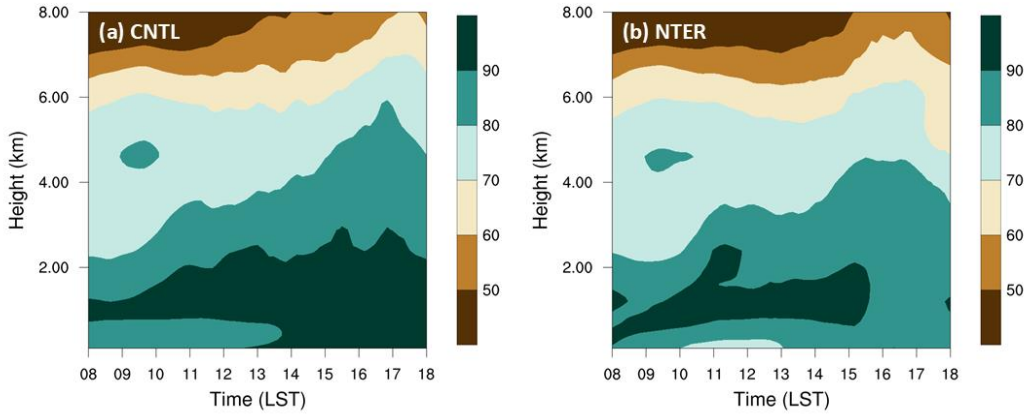

Figure 4.10. Time–height plot of domain-averaged relative humidity (colored; unit: %) over northern Taiwan domain for the (a) CNTL and (b) NTER experiments.

doi:10.6342/NTU202504233

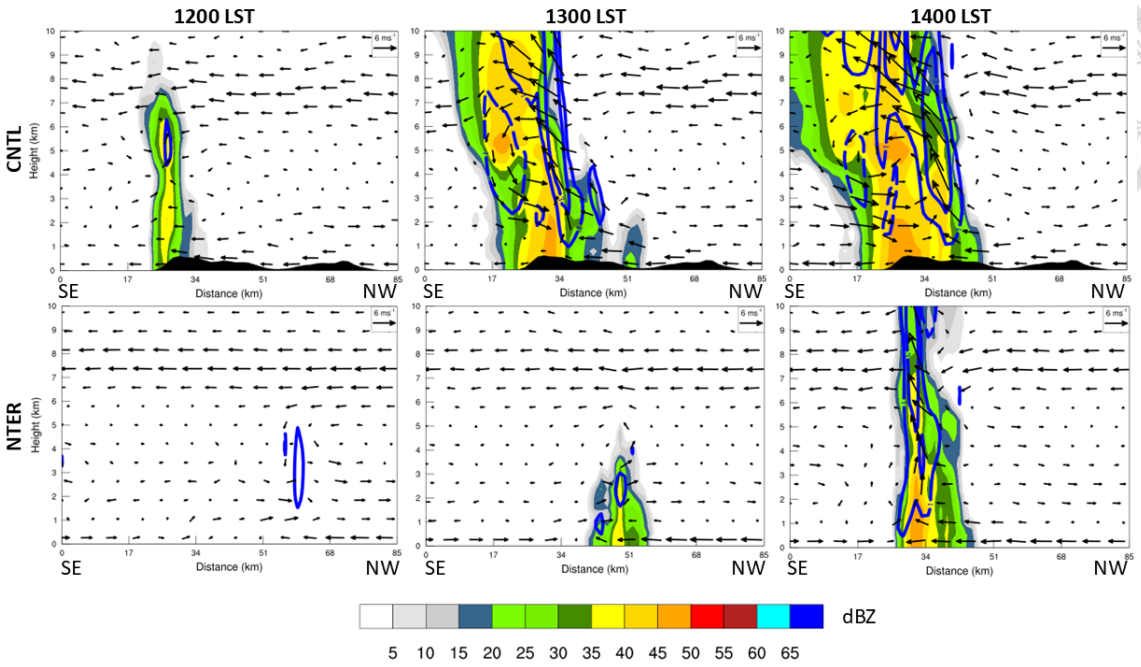

Figure 4.11. Time evolution of vertical cross sections along the NW–SE transect at 1200, 1300, and 1400 LST on 31 May 2022, for the CNTL (top row) and NTER (bottom row) experiments. Color indicates simulated radar reflectivity (dBZ), vectors show along-plane wind, and blue contours represent vertical velocity (solid for updrafts, dashed for downdrafts; −1, 1, 3, and 6 m s^{-1}). The average topography profile is shown by the black shading.

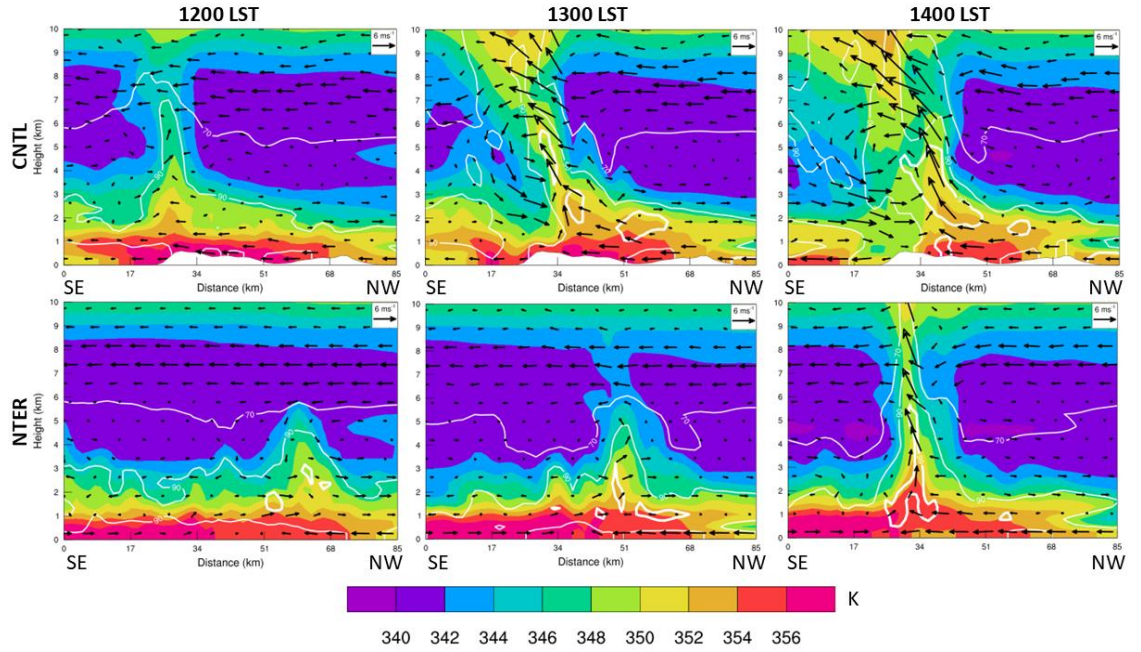

Figure 4.12. As in Fig. 4.11, but for equivalent potential temperature (colored; unit: K) and relative humidity (white contours at 70, 90, and 99%, with the 99% contour shown as a thick line).

doi:10.6342/NTU202504233

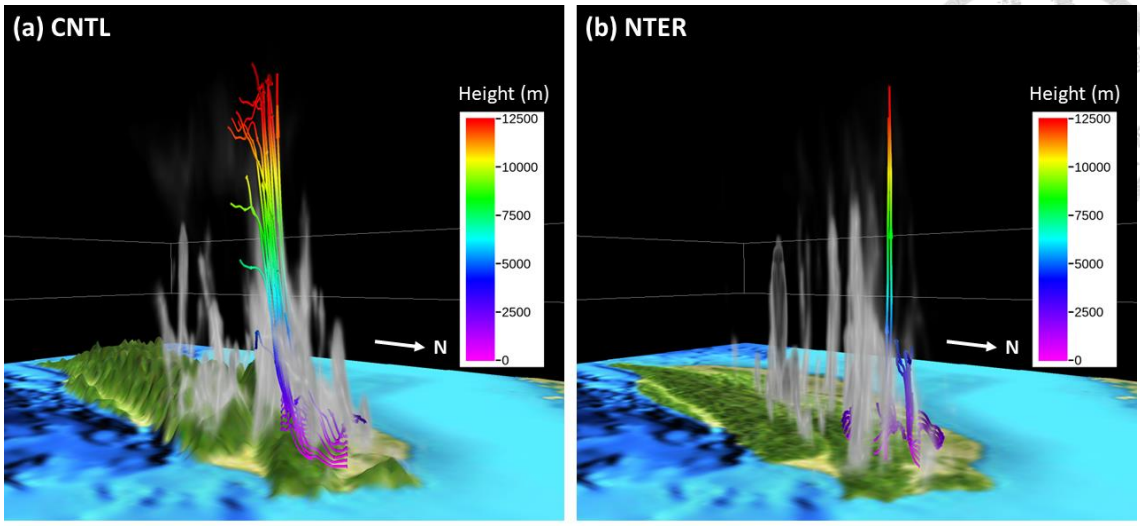

Figure 4.13. Three-dimensional perspective view of the cloud condensate (sum of cloud water and ice) and air parcel forward trajectories at t + 60 min in the (a) CNTL and (b) NTER experiments. The initial time t of forward trajectories is at 1300 LST. The view is from the northeast. Color scale along the trajectory indicates the height (unit: m MSL).

4.3.2 The relationship between MAUL and extreme rainfall

Figure 4.14 show time–height plots of MAUL grid counts within the northern Taiwan domain. It is evident that CNTL produces broader and deeper MAUL structures, with the 500-grid contour extending from near the surface up to ~5 km (Fig. 4.14a). In contrast, NTER shows more limited MAUL coverage, largely confined between 1 and 3.5 km (Fig. 4.14b). Notably, only CNTL exhibits significant MAUL presence below 1 km after 1300 LST, consistent with the enhanced relative humidity (Fig. 4.10). These results again highlight the important role of terrain-enhanced MFC in sustaining deep and persistent MAULs.

Naka and Takemi (2023) found a positive correlation between MAUL volume and total rainfall area during warm-season extreme rainfall events in Kyushu. To examine the relationship between MAUL and extreme rainfall over northern Taiwan, Fig. 4.15 shows the time series of MAUL volume and next-hour rainfall over land within the

doi:10.6342/NTU202504233

northern Taiwan domain. In CNTL, MAUL volume begins increasing rapidly after 0900 LST, exceeds 2000 km³ around 1100 LST, and reaches over 6500 km³ by 1530 LST (Fig. 4.15a). In contrast, NTER exhibits a more gradual increase, with MAUL volume surpassing 2000 km³ around 1300 LST and a lower peak of ~5000 km³ by 1500 LST.

Correspondingly, extreme rainfall in CNTL occurs earlier and is more intense than in NTER (Fig. 4.15b). For example, the maximum 1-hour rainfall in CNTL (~125 mm) peaks nearly two hours earlier than in NTER (~100 mm). A similar pattern is observed in the 99th percentile rainfall, whereas the 95th percentile maxima are comparable between simulations. The domain-average rainfall peak is marginally higher in NTER. These differences are consistent with the previous result that rainfall in CNTL is more spatially concentrated over the SMR (Fig. 4.3a), while NTER exhibits a broader distribution (Fig. 4.3b), suggesting that terrain confines convection to mountainous region and enhances localized extreme precipitation.

Figure 4.16 shows the relationship between MAUL volume and the next-hour rainfall statistics for the CNTL and NTER simulations. Notably, MAUL volume appears to be linked to subsequent rainfall intensity: both CNTL and NTER show that when MAUL volume exceeds 2000 km³ (3000 km³), the following hour's peak rainfall generally surpasses 40 mm (80 mm). Although the peaks in MAUL volume and rainfall do not occur simultaneously in CNTL, this discrepancy may be due to post-rainfall reductions in MFC. Nevertheless, this relationship underscores the importance of MAUL development in preconditioning the environment for extreme precipitation.

doi:10.6342/NTU202504233

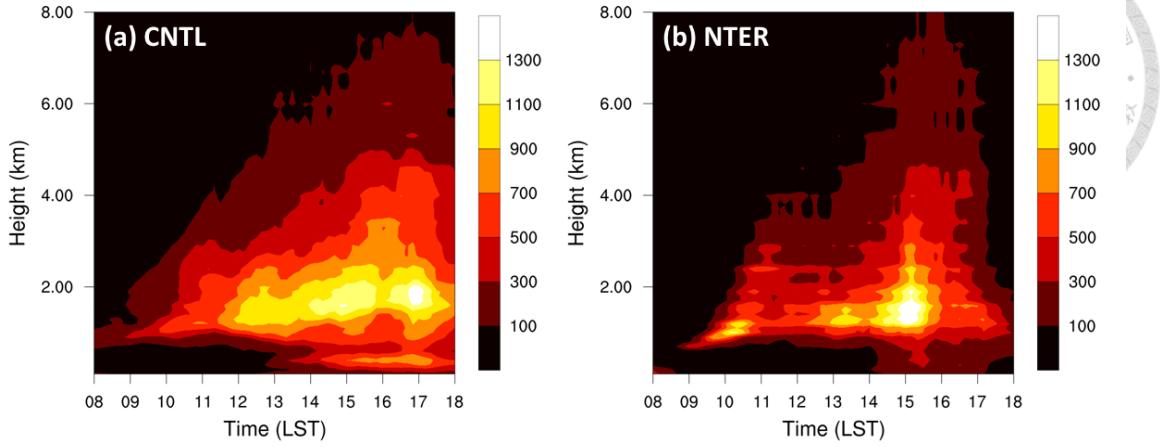

Figure 4.14. Time–height evolution of the number of moist absolutely unstable layer (MAUL) grid points within the northern Taiwan domain for (a) CNTL and (b) NTER experiments. Colors indicate the number of MAUL grid points at each time and height level.

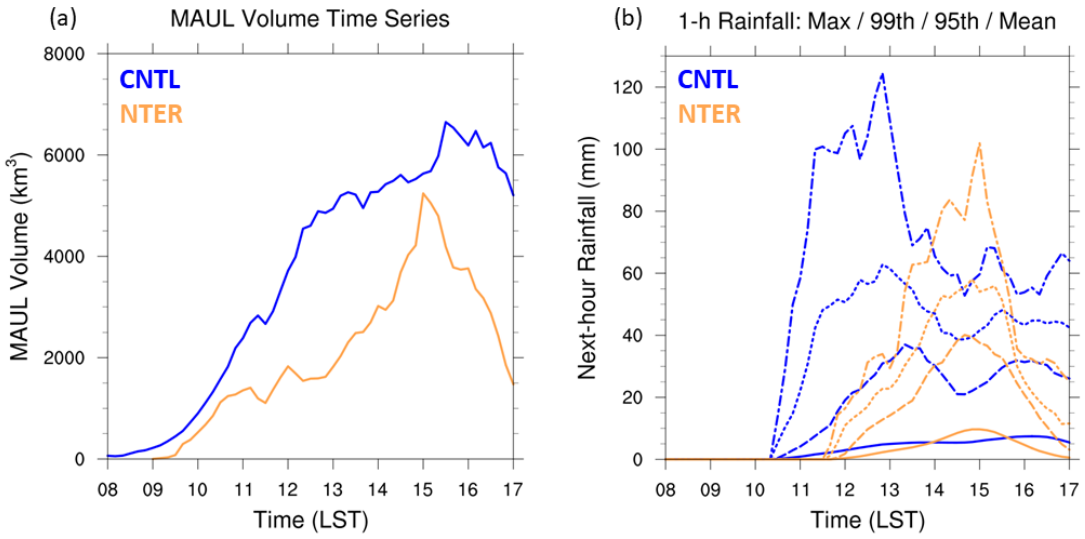

Figure 4.15. (a) Time series of moist absolutely unstable layer (MAUL) volume over northern Taiwan domain in CNTL (blue) and NTER (orange) experiments. (b) Time series of maximum (dash-dotted), 99th percentile (dotted), 95th percentile (dashed), and mean (solid) next-hour rainfall over land within northern Taiwan domain for CNTL (blue) and NTER (orange) experiments.

doi:10.6342/NTU202504233

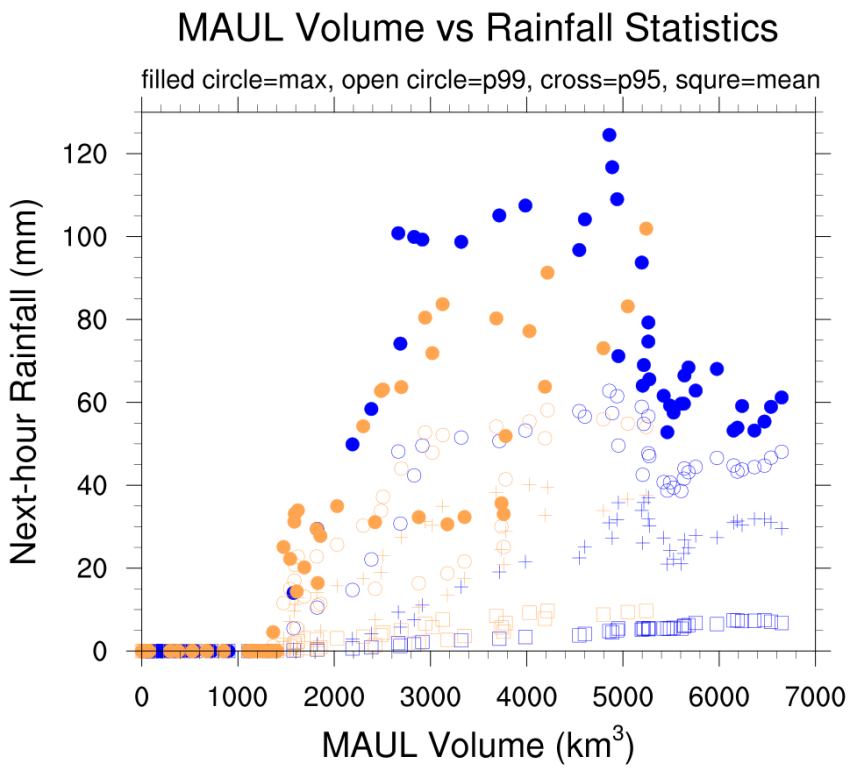

Figure 4.16. Scatterplot of next-hour rainfall statistics versus MAUL volume for CNTL (blue) and NTER (orange) experiments. Filled circles represent maximum 1-hour rainfall, open circles the 99th percentile, crosses the 95th percentile, and squares the domain-mean rainfall over northern Taiwan domain.

4.4 Discussion and summary

This study provides the first investigation of how terrain induces moist absolutely unstable layers (MAULs) and enhances the orographic rainfall in Taiwan. Using high-resolution WRF simulations with and without Taiwan terrain, we show that topography plays a critical role in enhancing moisture flux convergence (MFC) and supporting the formation of deep, persistent MAULs that precede intense precipitation. The key physical processes are summarized in Fig. 4.17.

When the southwesterly monsoon is blocked by Taiwan's topography, enhanced MFC develops in the wake region. The interaction among wake flow, sea breeze, and

doi:10.6342/NTU202504233

upslope flow transports abundant moisture from the ocean toward the mountain slope, a process shown to be critical for mountain flooding (Rasmussen & Houze 2012). The sustained upslope lifting in CNTL leads to the development of deep MAULs extending from near the surface up to ~5 km altitude. Trajectory analysis reveals that these MAULs are associated with layer lifting, in contrast to the shallower MAULs in NTER, where ascent is parcel-based and limited. These terrain-induced MAULs create a favorable thermodynamic environment for convection development.

Moreover, our results suggest a consistent relationship between MAUL volume and subsequent hourly rainfall. When MAUL volume exceeds 2000 km³ (3000 km³), the following hour's peak rainfall often surpasses 40 mm (80 mm). While the timing of MAUL and rainfall peaks may differ, this threshold-like relationship highlights the diagnostic potential of MAUL volume as a precursor to extreme precipitation events. Naka and Takemi (2023) used the analysis fields from the Mesoscale Model (MSM), which has a horizontal grid spacing of 5 km and a temporal resolution of 3 hours, along with rain gauge observations. They found that humid conditions contribute to the formation of deep MAULs, which tend to appear within localized areas in and around regions of heavy rainfall, often preceding the onset of intense precipitation. Their findings are consistent with our results, which suggest that terrain-enhanced moistening plays a critical role in preconditioning the environment for MAUL development and subsequent extreme rainfall.

Bryan and Fritsch (2000) has suggested that the maintenance of MAUL requires mesoscale, dynamically forced ascent; otherwise, MAULs are rapidly eroded by small-scale convective turbulence. For example, in relatively dry midlatitude environments, cold pool lifting has been shown to help sustain MAUL by providing strong mesoscale ascent (Bryan and Fritsch 2000; James et al. 2005). In this study, we

doi:10.6342/NTU202504233

emphasize the terrain-induced MAUL. The multiscale interactions of terrain with background flow and local circulation enhance MFC, promoting a more humid environment, which supports MAUL formation (Mechem et al., 2002; Takemi and Unuma, 2020; Tsuji et al., 2021). This moist environment, combined with layer-lifting inflow along the mountain slope, facilitates the formation of deep MAULs responsible for the extreme orographic rainfall.

Although this study provides valuable insights into thunderstorm dynamics influenced by southwesterly monsoon flow and complex terrain, it has several limitations. First, the conclusions are based on numerical simulations, which are subject to model deficiencies, uncertainties in physical parameterizations, and numerical errors. These limitations should be kept in mind when interpreting the results. While the analysis focuses on a single case, the detailed process-level understanding of MAUL formation in a subtropical mountainous environment lays the groundwork for broader investigations. Future research should evaluate the generality of these findings across multiple events and incorporate high-resolution observations and analysis data to validate the simulated MAUL structures (e.g., Tsuji et al. 2021; Naka and Takemi 2023). In addition, assessing the representation of MAUL in operational weather and regional climate models may help improve the prediction of high-impact weather events in complex terrain.

doi:10.6342/NTU202504233

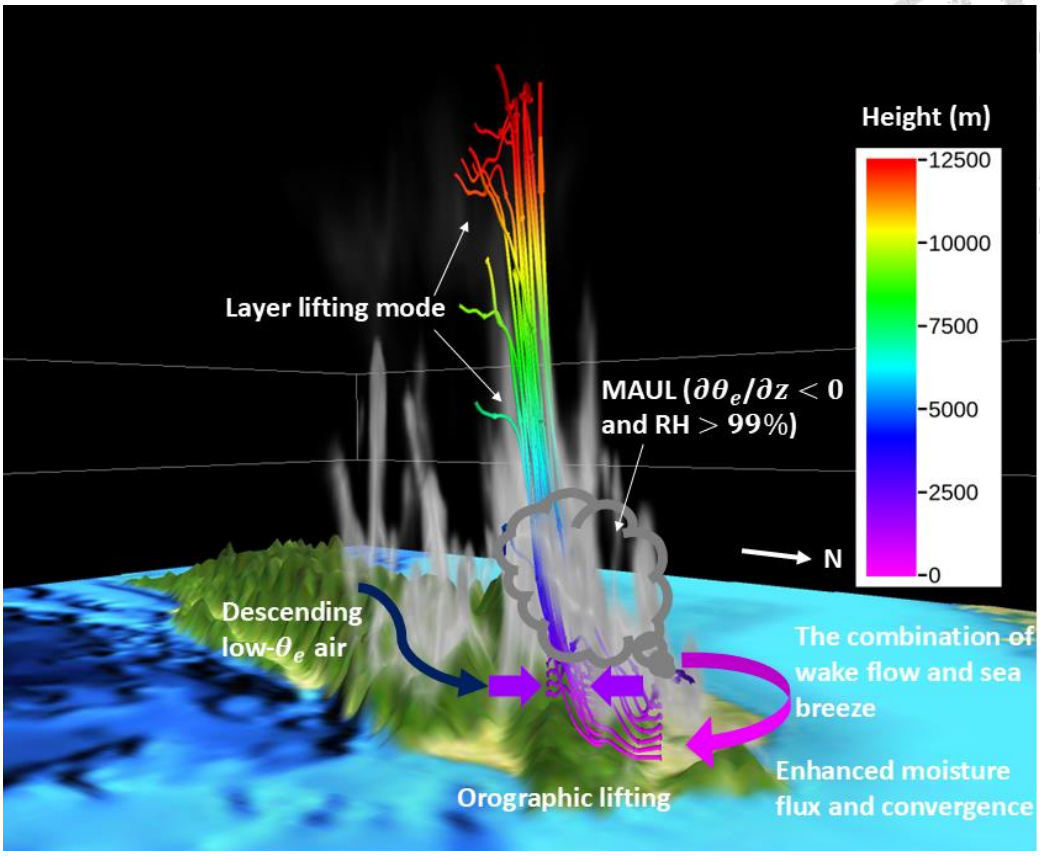

Figure 4.17. Conceptual 3D visualization of the physical processes leading to MAUL formation and extreme orographic rainfall in CNTL. Arrows illustrate the interaction of wake flow and sea breeze enhancing moisture flux convergence, with orographic lifting forcing layer lifting of inflow. The layer lifting mode supports the development of MAULs (defined by $d\theta_e/dz < 0$ and RH > 99%) and intense convection. Descending low-θ_e air intrudes from the southeast, possibly maintaining the low-level convergence. Trajectories are colored by altitude to illustrate the vertical extent of updrafts.

doi:10.6342/NTU202504233

Chapter 5 Conclusions and Future Work

This dissertation advances the understanding of extreme afternoon thunderstorms (ATSs) over complex terrain by elucidating how multiscale interactions among large-scale synoptic flow, mesoscale terrain-modulated circulations, and storm-scale convective processes jointly control the evolution and intensity of severe convection in northern Taiwan. Through a combination of high-resolution numerical simulations and polarimetric radar observations, this research highlights the critical role of terrain in modulating key convective ingredients — cold pool dynamics, moisture flux convergence (MFC), and the formation of moist absolutely unstable layers (MAULs) — and demonstrates how these ingredients interact to produce short-duration extreme rainfall.

Chapter 2 explored how mid-level relative humidity affects the evolution and intensity of weakly-forced ATSs over basin terrain, using an extreme ATS event on 14 June 2015. Sensitivity experiments demonstrated that drier mid-level conditions enhance cold pool strength through increased evaporative cooling, which promotes stronger low-level convergence and more effective lifting of moist parcels into the upper troposphere. This process favors the formation of large graupel particles and intense latent heating aloft, leading to wider and more intense convective systems. Conversely, moister mid-level air reduces evaporative cooling, weakens cold pools, and limits convective intensity. A key insight is the “basin confinement effect,” whereby the Taipei Basin’s topography traps cold pool outflows and sea-breeze inflow, enhancing sustained convergence and reducing entrainment rate, ultimately promoting extreme rainfall over the basin. These findings highlight how topography can fundamentally

doi:10.6342/NTU202504233

modulate the response of convection to mid-level moisture, underscoring the importance of considering orographic processes when forecasting short-duration rainfall extremes.

Chapter 3 leveraged high-quality polarimetric radar observations and multi-Doppler wind retrievals to examine the kinematic and microphysical characteristics of ATSs during TAHOPE/PRECIP IOP 2. Two convective episodes were analyzed, with Episode 1 exhibiting multiple cell merger (MCM) associated with terrain-induced convergence, while Episode 2 featured weaker, isolated cells. The multiple cell merger process was marked by a broadening of the enhanced ZDR region (>8 km at 5.5 km AMSL), which preceded updraft intensification and the onset of heavy rainfall. This relationship was also supported by two additional ATS cases during TAHOPE/PRECIP analyzed in this study, both of which exhibited similar widening of the ZDR region coinciding with subsequent increases in updraft strength and precipitation intensity. These findings suggest that the width of ZDR columns provides a valuable diagnostic of convective organization and storm severity in mountainous environments, particularly when combined with knowledge of cell merger processes. Furthermore, cell separation distances observed in the MCM events were larger than those in previous weakly-forced ATS studies (e.g., Miao and Yang 2018; Wu et al. 2021; Jung and Jou 2023), indicating that terrain-driven low-level convergence may facilitate cell mergers over greater distances in complex terrain. The results demonstrate the potential of ZDR column width as an indicator of updraft dynamics and rainfall intensity in orographic thunderstorms.

Chapter 4 focused on the formation of MAULs in relation to extreme orographic rainfall during TAHOPE/PRECIP IOP 2 using cloud-resolving simulations. It was found that terrain interaction with southwesterly monsoonal flow creates enhanced moisture

doi:10.6342/NTU202504233

flux convergence downstream of the mountains, where wake flow, sea breeze, and upslope winds combine to transport moisture over the SMR. The layer-lifting inflow along the mountain slope promotes the development of deep MAULs reaching ~5 km altitude. In contrast, simulations without terrain produced only shallow, parcel-based ascent and limited MAUL formation. A threshold-like relationship emerged between MAUL volume and next-hour rainfall intensity, suggesting that MAUL diagnostics could serve as precursors for extreme precipitation risk. These findings complement recent studies on MAUL by directly connecting terrain-enhanced moistening and MAUL development to extreme rainfall, providing new insights into the processes sustaining MAULs in subtropical mountainous environments.

In contrast to the weakly forced ATS extreme rainfall event (i.e., 20150614), the strong synoptic environment of TAHOPE/PRECIP IOP 2 featured southwesterly monsoonal flow and a surface front near the northern coast of Taiwan. Midlevel air was relatively moist (RH >70%), accompanied by weaker cold pool (not shown), consistent with findings from Miao and Yang (2022). The weak cold pool was unable to push the sea breeze offshore, resulting in persistent low-level convergence over the SMR and extreme rainfall in the mountainous region (Miao and Yang 2020). Under these conditions, the sea breeze and upslope winds continuously ascended along the mountain slopes, transporting moisture upslope. Previous studies on mountain flooding events have also highlighted that multiscale moisture transport contributes critically to orographic flash floods (Maddox et al. 1978; Caracena et al. 1979; Rasmussen and Houze 2012).

However, what has not been explored previously is that layer lifting along mountain slopes can lead to deep and sustained moist absolutely unstable layers (MAULs), which precondition the environment for extreme orographic rainfall. This

doi:10.6342/NTU202504233

study's findings emphasize that terrain not only provides dynamic forcing but can also modulate the thermodynamic structure of the convective environment.

Collectively, this dissertation demonstrates that the interplay of synoptic forcing, mesoscale terrain-induced circulations, and storm-scale processes must be considered to understand and predict ATS behavior. The contrasting evolutions of ATSs under weak and strong synoptic environments highlight that terrain impacts depend on the broader synoptic context and environmental moisture profiles. These findings underscore the importance of integrating multiscale interactions when assessing extreme precipitation risks over complex terrain.

Moreover, this dissertation provides several insights that may contribute to improving the forecasting of ATSs over complex terrain. The numerical experiments highlight the critical role of midlevel RH in modulating cold pool dynamics and convective organization, especially under weak synoptic forcing. Additionally, polarimetric radar analyses suggest that the horizontal extent of ZDR columns can serve as a useful diagnostic indicator of convective intensification, providing potential value for nowcasting efforts. The findings from cloud-resolving simulations also indicate that the volume of MAULs may be used as precursors for identifying environments conducive to extreme precipitation, particularly under strong synoptic forcing. Together, these multiscale insights underscore the importance of integrating observations and simulations to enhance forecasting capabilities for short-duration extreme rainfall in mountainous regions.

Building upon the findings of this dissertation, future research should leverage the dense observations collected during the TAHOPE/PRECIP field campaign, including intensive soundings and rain gauge networks, to systematically investigate the frequency of MAUL occurrence during the warm season and its relationship with heavy

doi:10.6342/NTU202504233

rainfall events. Additionally, high-resolution analyses and forecasts from MPAS or WRF during the campaign period can be used to examine the horizontal and vertical structures of MAULs and their influence on convective evolution. Conducting statistical analyses across multiple events will help clarify the generality of MAUL-related processes under diverse thermodynamic and synoptic environments. Sensitivity experiments should also systematically assess how variations in moisture profiles and terrain geometry affect MAUL formation and associated precipitation. Furthermore, expanding investigations to other extreme rainfall contexts, such as typhoon rainbands or mei-yu frontal systems, could elucidate the broader significance of MAUL dynamics in East Asian heavy rainfall events. These efforts will improve predictive capabilities for extreme precipitation in complex terrain, ultimately enhancing disaster preparedness and resilience in regions prone to flash floods.

doi:10.6342/NTU202504233

REFERENCE

Banacos, P. C., and D. M. Schultz, 2005: The use of moisture flux convergence in forecasting convective initiation: Historical and operational perspectives. Wea. Forecasting, 20, 351–366, doi:10.1175/WAF858.1.

Bell, Michael, Michael Dixon, Wen-Chau Lee, Brenda Javornik, Jennifer DeHart, Ting-Yu Cha, and Alex DesRosiers. (2022). nsf-lrose/lrose-topaz: lrose-topaz stable final release 20220222 (lrose-topaz-2022022). Zenodo. https://doi.org/10.5281/zenodo.6909479.

Bell, M. M., M. T. Montgomery, and K. A. Emanuel, 2012: Air–sea enthalpy and momentum exchange at major hurricane wind speeds observed during CBLAST. *J. Atmos. Sci.*, **69**, 3197–3222.

Bodine, D. J., and K. L. Rasmussen, 2017: Evolution of Mesoscale Convective System Organizational Structure and Convective Line Propagation. *Mon. Wea. Rev.*, **145**, 3419–3440.

Bringi, V. N., K. Knupp, A. Detwiler, L. Liu, I. J. Caylor, and R. A. Black, 1997: Evolution of a Florida thunderstorm during the Convection and Precipitation/Electrification Experiment: The case of 9 August 1991. *Mon. Wea. Rev.*, **125**, 2131–2160.

Brown, R. G., and C. Zhang, 1997: Variability of midtropospheric moisture and its effects on cloud-top height distribution during TOGA COARE. *J. Atmos. Sci.,* **54**, 2760–2774.

doi:10.6342/NTU202504233

Browning, K. A., and F. H. Ludlum, 1962: Airflow in convective storms. *Quart. J. Roy. Meteor. Soc.*, **88,** 117–135.

Bryan, G. H., & Fritsch, J. M. (2000). Moist absolute instability: The sixth static stability state. *Bulletin of the American Meteorological Society*, **81**(6), 1207–1230.

Bryan, G. H., and M. D. Parker, 2010: Observations of a squall line and its near environment using high-frequency Rawinsonde launches during VORTEX2, *Mon. Wea. Rev.*, **138**, 4076–4097, doi:10.1175/2010MWR3359.1.

Caracena, F., R. A. Maddox, L. R. Hoxit, and C. F. Chappell, 1979*:* Mesoanalysis of the Big Thompson Storm. *Mon. Wea. Rev.*, ***107***, 1–17.

Carey, L. D., and S. A. Rutledge, 2000: The relationship between precipitation and lightning in tropical island convection: A C-band polarimetric radar study. *Mon. Wea. Rev.*, **128**, 2687–2710.

Cha, T., and M. M. Bell, 2023: Three-dimensional variational multi-Doppler wind retrieval over complex terrain. *J. Atmos. Oceanic Technol.*, **40**, 1381–1405, https://doi.org/10.1175/JTECH-D-23-0019.1.

Chang, P., and Coauthors, 2021: An Operational Multi-Radar Multi-Sensor QPE System in Taiwan. *Bull. Amer. Meteor. Soc.*, **102**, E555–E577, https://doi.org/10.1175/BAMS-D-20-0043.1.

Chang, W., W. Lee, and Y. Liou, 2015: The kinematic and microphysical characteristics and associated precipitation efficiency of subtropical convection during SoWMEX/TiMREX. *Mon. Wea. Rev.*, **143**, 317–340, https://doi.org/10.1175/MWR-D-14-00081.1.

doi:10.6342/NTU202504233

Chen, C., and C. Liu, 2014: The definition of urban stormwater tolerance threshold and its conceptual estimation: an example from Taiwan. *Nat. Hazards,* 73, 173–190. https://doi.org/10.1007/s11069-013-0645-7

Chen, G. T.-J., H.-C. Chou, T. C. Chang, and C. S. Liu, 2001: Frontal and non-frontal convection over northern Taiwan in mei-yu season (in Chinese with English abstract). *Atmos. Sci.*, **29**, 37–52.

Chen, G., K. Zhao, L. Wen, M. Wang, H. Huang, M. Wang, Z. Yang, G. Zhang, P. Zhang, and W.-C. Lee, 2019: Microphysical Characteristics of Three Convective Events with Intense Rainfall Observed by Polarimetric Radar and Disdrometer in Eastern China. *Remote Sensing*, **11**, 2004, https://doi.org/10.3390/rs11172004.

Chen, J., T. Tsai, M. Tzeng, C. Liao, H. Kuo, and J. Hong, 2022: Microphysical Perturbation Experiments and Ensemble Forecasts on Summertime Heavy Rainfall over Northern Taiwan. *Wea. Forecasting*, **37**, 1641–1659.

Chen, P.-Y., and C.-M. Wu., 2025: Identifying Cold Pool Scales Over Complex Topography Using TaiwanVVM Simulations. *Journal of the Meteorological Society of Japan,* **103**, 453–468.

Chen, T.-C., J. Tsay, and E. S. Takle, 2016: A forecast advisory for afternoon thunderstorm occurrence in the Taipei basin during summer developed from diagnostic analysis. *Wea. Forecasting*, **31**, 531–552.

Chen, T.-C., S.-Y. Wang, and M.-C. Yen, 2007: Enhancement of afternoon thunderstorm activity by urbanization in a valley: Taipei. *J. Appl. Meteor. Climatol.*, **46**, 1324–1340.

Chen, X., F. Zhang, and K. Zhao, 2017: Influence of monsoonal wind speed and moisture content on intensity and diurnal variations of the Mei-Yu season

doi:10.6342/NTU202504233

coastal rainfall over South China. *J. Atmos. Sci.,* **74**, 2835–2856, https://doi.org/10.1175/JAS-D-17-0081.1.

Choi, H.-Y., Ha, J.-H., Lee, D.-K., & Kuo, Y.-H. (2011). Analysis and simulation of mesoscale convective systems accompanying heavy rainfall: The goyang case. *Asia-Pacific Journal of Atmospheric Sciences*, **47**(3), 265–279.

Clyne, J., and M. Rast, 2005: A prototype discovery environment for analyzing and visualizing terascale turbulent fluid flow simulations, *Proceedings of Visualization and Data Analysis*, 284–294.

Clyne, J., P. Mininni, A. Norton, and M. Rast, 2007: Interactive desktop analysis of high-resolution simulations: Application to turbulent plume dynamics and current sheet formation, *New Journal of Physics*, **9**, 301.

Cornejo, I. C., A. K. Rowe, K. L. Rasmussen, and J. C. DeHart, 2024: Orographic controls on extreme precipitation associated with a Mei-Yu front. *Mon. Wea. Rev.*, **152**, 531–551, https://doi.org/10.1175/MWR-D-23-0170.1.

Dee, D. P., and Coauthors, 2011: The ERA-Interim reanalysis: Configuration and performance of the data assimilation system. *Quart. J. Roy. Meteor. Soc.*, **137**, 553–597, https://doi.org/10.1002/qj.828.

DeHart, J., Dixon, M., Javornik, B., Bell, M., Cha, T.-Y., DesRosiers, A., & Lee, W.-C. (2024). nsf-lrose/lrose-releases: lrose-jade-20230814 (lrose-jade-20230814). [Software] Zenodo. https://doi.org/10.5281/zenodo.11479603.

Doswell, C. A., H. E. Brooks, and R. A. Maddox, 1996: Flash flood forecasting: An ingredients-based methodology. *Wea. Forecasting*, **11**, 560–581.

Du, Y., G. Chen, B. Han, L. Bai, and M. Li, 2020: Convection initiation and growth at the coast of south China. Part II: Effects of the terrain, coastline, and cold

doi:10.6342/NTU202504233

pools. *Mon. Wea. Rev.*, **148**, 3871–3892, https://doi.org/10.1175/MWR-D-20-0090.1.

Dudhia, J., 1989: Numerical study of convection observed during the winter monsoon experiment using a mesoscale two-dimensional model. *J. Atmos. Sci.*, **46**, 3077–3107.

Emanuel, K. A., 1994: *Atmospheric Convection*. Oxford University Press, 580 pp.

Fawbush, E. J., and R. C. Miller, 1954: The types of airmasses in which North American tornadoes form. *Bull. Amer. Meteor. Soc.*, **35**, 154–165.

Feng, Z., S. Hagos, A. K. Rowe, C. D. Burleyson, M. N. Martini, and S. P. de Szoeke, 2015: Mechanisms of convective cloud organization by cold pools over tropical warm ocean during the AMIE/DYNAMO field campaign. *J. Adv. Model. Earth Syst.*, **7**, 357–381.

Foerster, A.M.; Bell, M.M. Thermodynamic retrieval in rapidly rotating vortices from multiple-Doppler radar data. *J. Atmos. Ocean. Technol.* **2017**, *34*, 2353–2374.

Foster, D. S., 1958: Thunderstorm gusts compared with computed downdraft speeds. *Mon. Wea. Rev.*, **86**, 91–94.

French, M. M., and D. M. Kingfield, 2021: Tornado Formation and Intensity Prediction Using Polarimetric Radar Estimates of Updraft Area. *Wea. Forecasting*, **36**, 2211–2231, https://doi.org/10.1175/WAF-D-21-0087.1.

Gilmore, M. S., and L. J. Wicker, 1998: The influence of midtropospheric dryness on supercell morphology and evolution. *Mon. Wea. Rev.*, **126**, 943–958

Glenn, I. B., and S. K. Krueger, 2017: Connections matter: Updraft merging in organized tropical deep convection. *Geophys. Res. Lett.*, **44**, 7087–7094.

doi:10.6342/NTU202504233

Heikenfeld, M., Marinescu, P. J., Christensen, M., Watson-Parris, D., Senf, F., van den Heever, S. C., and Stier, P.: tobac 1.2: towards a flexible framework for tracking and analysis of clouds in diverse datasets, *Geosci. Model Dev.*, **12**, 4551–4570, https://doi.org/10.5194/gmd-12-4551-2019, 2019.

Helmus, J. J., and S. M. Collis, 2016: The Python ARM radar toolkit (Py-ART), a library for working with weather radar data in the Python programming language. *J. Open Res. Softw.*, **4**, e25, https://doi.org/10.5334/jors.119.

Hohenegger, C. and Bretherton, C. S.: Simulating deep convection with a shallow convection scheme, Atmos. Chem. Phys., 11, 10389–10406, https://doi.org/10.5194/acp-11-10389-2011, 2011.

Hong, S.-Y., and H.-L. Pan, 1996: Nonlocal boundary layer vertical diffusion in a medium-range forecast model. *Mon. Wea. Rev.*, **124**, 2322–2339.

Houze, R. A., Jr., 2014: *Cloud Dynamics*, 2nd Ed., Elsevier/Academic Press, Oxford, 432 pp.

Houze, R. A. Jr., 2012: Orographic effects on precipitating clouds, *Rev. Geophys.*, **50**, RG1001, doi:10.1029/2011RG000365.

Hua, S., Xu, X., & Chen, B. (2020). Influence of multiscale orography on the initiation and maintenance of a precipitating convective system in North China: A case study. *Journal of Geophysical Research: Atmospheres*, 125, e2019JD031731.

Huang, Y., Liu, Y., Liu, Y., Li, H., and J. C. Knievel, 2019: Mechanisms for a record-breaking rainfall in the coastal metropolitan city of Guangzhou, China: Observation analysis and nested very large eddy simulation with the WRF model. *J. of Geophys. Res. Atmos*, **124**, 1370–1391, https://doi.org/10.1029/2018JD029668

doi:10.6342/NTU202504233

Illingworth, A. J., W. Goddard, and S. Cherry, 1987: Polarization radar studies of precipitation development in convective storms. *Quart. J. Roy. Meteor. Soc.*, **113**, 469–489.

James, R. P., and P. M. Markowski, 2010: A numerical investigation of the effects of dry air aloft on deep convection. *Mon. Wea. Rev.*, **138**, 140–161, https://doi.org/10.1175/2009MWR3018.1.

James, R. P., Fritsch, J. M., & Markowski, P. M. (2005). Environmental distinctions between cellular and slabular convective lines. *Monthly Weather Review*, **133**, 2669–2691.

Johns, R. H., and C. A. Doswell III, 1992: Severe local storms forecasting. *Wea. Forecasting*, **7**, 588–612.

Johnson, R. H., and J. F. Breach, 1991: Diagnosed characteristics of precipitation systems over Taiwan during the May-June 1987 TAMEX. *Mon. Wea. Rev.*, **119**, 2540–2557.

Jou, B. J.-D., 1994: Mountain-originated mesoscale precipitation system in northern Taiwan: A case study of 21 June 1991. *Terr. Atmos. Oceanic Sci.*, **5**, 169–197.

Jou, B. J.-D., Y.-C. Kao, R.-G. R. Hsiu, C.-J. U. Jung, J. R. Lee, and H. C. Kuo, 2016: Observational characteristics and forecast challenge of Taipei flash flood afternoon thunderstorm: Case study of 14 June 2015 (in Chinese with English abstract). *Atmos. Sci.*, **44**, 57–82.

Jung, C., and B. J. Jou, 2023: Bulk microphysical characteristics of a heavy-rain complex thunderstorm system in the Taipei basin. *Mon. Wea. Rev.*, **151**, 877–896, https://doi.org/10.1175/MWR-D-22-0078.1.

doi:10.6342/NTU202504233

Kain, J. S., and J. M. Fritsch, 1993: Convective parameterization for mesoscale models: The Kain-Fritsch scheme. *The Representation of Cumulus Convection in Numerical Models*, *Meteor. Monogr.,* No. 46*,* Amer. Meteor. Soc., 165–177.

Kain, J. S., and J. M. Fritsch, 1990: A one dimensional entraining/detraining plume model and its application in convective parameterization. *J. Atmos. Sci.*, **47 ,** 2784–2802.

Kerns, B. W. J., Y.-L. Chen, and M.-Y. Chang, 2010: The diurnal cycle of winds, rain, and clouds over Taiwan during the Mei-yu, summer, and autumn rainfall regimes. *Mon. Wea. Rev.*, **138**, 497–516.

Khairoutdinov MF, Randall D. 2006. High-resolution simulation of shallow to deep convection transition over land. *J. Atmos. Sci.,* **63**, 3421–3436.

Khairoutdinov, M. F., S. K. Krueger, C.-H. Moeng, P. A. Bogenschutz, D. Randall, 2009: Large-eddy simulation of maritime deep tropical convection. *J. Adv. Model Earth Syst*. 1: Art. 15, DOI: 10.3894/JAMES.2009.1.15.

Kirshbaum, D.J.; Adler, B.; Kalthoff, N.; Barthlott, C.; Serafin, S. Moist Orographic Convection: Physical Mechanisms and Links to Surface-Exchange Processes. *Atmosphere* **2018**, *9*, 80. https://doi.org/10.3390/atmos9030080

Klaus, V., H. Rieder, and R. Kaltenböck, 2023: Insights in Hailstorm Dynamics through Polarimetric High-Resolution X-Band and Operational C-Band Radar: A Case Study for Vienna, Austria. *Mon. Wea. Rev.*, **151**, 913–929, https://doi.org/10.1175/MWR-D-22-0185.1.

Kuang, Z., and C. S. Bretherton, 2006: A mass-flux scheme view of a high-resolution simulation of a transition from shallow to deep cumulus convection. *J. Atmos. Sci.*, **63**, 1895–1909.

doi:10.6342/NTU202504233

Kumjian, M. R., A. P. Khain, N. Benmoshe, E. Ilotoviz, A. V. Ryzhkov, and V. T. J. Phillips, 2014: The anatomy and physics of ZDR columns: Investigating a polarimetric radar signature with a spectral bin microphysical model. *J. Appl. Meteor. Climatol.*, **53**, 1820–1843.

Kumjian, M. R., and A. V. Ryzhkov, 2008: Polarimetric Signatures in Supercell Thunderstorms. *J. Appl. Meteorol. Climatol.*, **47**, 1940–1961.

Kumjian, M. R., and A. V. Ryzhkov, 2012: The impact of size sorting on the polarimetric radar variables. *J. Atmos. Sci.*, **69**, 2042–2060.

Kumjian, M. R., and O. P. Prat, 2014: The impact of raindrop collisional processes on the polarimetric radar variables. *J. Atmos. Sci.*, **71**, 3052–3067. https://doi.org/10.1175/JAS-D-13-0357.1

Kumjian, M. R., O. P. Prat, K. J. Reimel, M. van Lier-Walqui, and H. C. Morrison, 2022: Dual-Polarization Radar Fingerprints of Precipitation Physics: A Review. *Remote Sensing*, **14**, 3706.

Kuo, K.-T., and C.-M. Wu, 2019: The precipitation hotspots of afternoon thunderstorms over the Taipei basin: Idealized numerical simulations. J. Meteor. Soc. Japan, 97, 501–517, https://doi.org/10.2151/jmsj.2019-031.

Kurowski, M. J., K. Suselj, W. W. Grabowski, and J. Teixeira, 2018: Shallow-to-deep transition of continental moist convection: Cold pools, surface fluxes, and mesoscale organization. *J. Atmos. Sci.*, **75**, 4071–4090, https://doi.org/10.1175/JAS-D-18-0031.1.

Kuster, C. M., J. C. Snyder, T. J. Schuur, T. T. Lindley, P. L. Heinselman, J. C. Furtado, J. W. Brogden, and R. Toomey, 2019: Rapid-update radar observations of ZDR column depth and its use in the warning decision process. *Wea. Forecasting*, **34**, 1173–1188, https://doi.org/10.1175/WAF-D-19-0024.1.

doi:10.6342/NTU202504233

Lee, M.-T., P.-L. Lin, W.-Y. Chang, B. K. Seela, and J. Janapati, 2019: Microphysical characteristics and types of precipitation for different seasons over North Taiwan. *J. Meteor. Soc. Japan*, **97**, 841–865, https://doi.org/10.2151/jmsj.2019-048.

Li, H., Y. Huang, S. Hu, N. Wu, X. Liu, and H. Xiao, 2021: Roles of terrain, surface roughness, and cold pool outflows in an extreme rainfall event over the coastal region of South China. *J. Geophys. Res. Atmos.* **126**, e2021JD035556. https://doi.org/10.1029/2021JD035556

Lim, K.-S. S., and S.-Y. Hong, 2010: Development of an effective double-moment cloud microphysics scheme with prognostic cloud condensation nuclei (CCN) for weather and climate models. *Mon. Wea. Rev.*, **138**, 1587–1612.

Lin, P.-F., P.-L. Chang, B. J.-D. Jou, J. W. Wilson, and R. D. Roberts, 2011: Warm season afternoon thunderstorm characteristics under weak synoptic-scale forcing over Taiwan island. Wea. Forecasting, 26, 44-60.

Lin, P.-F., P.-L. Chang, B. J.-D. Jou, J. W. Wilson, and R. D. Roberts, 2012: Objective predication of warm season afternoon thunderstorms in northern Taiwan using a fuzzy logic approach. Wea. Forecasting, 27, 1178-1197.

Loney, M. L., D. S. Zrnić, J. M. Straka, and A. V. Ryzhkov, 2002: Enhanced polarimetric radar signatures above the melting level in a supercell storm. *J. Appl. Meteor.*, **41**, 1179–1194.

Maddox, R. A., L. R. Hoxit, C. F. Chappell, and F. Caracena, 1978*:* Comparison of meteorological aspects of the Big Thompson flood and Rapid City flash floods. *Mon. Wea. Rev.*, ***106***, 375–389.

doi:10.6342/NTU202504233

Mechem, D. B., Houze, R. A., Jr., & Chen, S. S. (2002). Layer inflow into precipitating convection over the western tropical Pacific. *Quarterly Journal of the Royal Meteorological Society*, **128**(584), 1997–2030.

Medina, S., R. A. Houze Jr., A. Kumar, and D. Niyogi, 2010: Summer monsoon convection in the Himalayan region: Terrain and land cover effects. *Quart. J. Roy. Meteor. Soc.*, **136**, 593–616.

Miao, J.-E., and M.-J. Yang, 2018: Cell merger and heavy rainfall of the severe afternoon thunderstorm event at Taipei on 14 June 2015. *Atmos. Sci.*, **46**, 427–453 (in Chinese with English abstract). https://doi.org/10.3966/025400022018124604004

Miao, J.-E., and M.-J. Yang, 2020: A modeling study of the severe afternoon thunderstorm event at Taipei on 14 June 2015: The roles of sea breeze, microphysics, and terrain. *J. Meteor. Soc. Japan*, **98**, 129–152, https://doi.org/10.2151/jmsj.2020-008.

Miao, J.-E., and M.-J. Yang, 2022: The impacts of midlevel moisture on the structure, evolution, and precipitation of afternoon thunderstorms: A real-case modeling study at Taipei on 14 June 2015. *J. Atmos. Sci.*, **79**, 1837–1857, https://doi.org/10.1175/JAS-D-21-0257.1.

Miao, J.-E., M.-J. Yang, K. L. Rasmussen, M. M. Bell, H.-C. Kuo, and T.-Y. Cha, 2025: Microphysical and Kinematical Characteristics of Merged and Isolated Convective Cells over the Complex Terrain of the Taipei Basin. *J. Geophys. Res. Atmos.*, conditionally accepted with minor revision.

Mlawer E. J., S. J. Taubman, P. D. Brown, M. J. Iocono, and S. A. Clough, 1997: Radiative transfer for inhomogeneous atmospheres: RRTM, a validated

doi:10.6342/NTU202504233

correlated-k model for the longwave. *J. Geophys. Res. Atmos.*, **102**, 16663–16682.

Morrison, H., M. van Lier-Walqui, A. M. Fridlind, W. W. Grabowski, J. Y. Harrington, and C. Hoose, 2020: Confronting the challenge of modeling cloud and precipitation microphysics. *J. Adv. Model. Earth Sys.*, **12**, e2019MS001689. https://doi.org/10.1029/2019MS001689

Moseley, C., C. Hohenegger, P. Berg, and J. O. Haerter, 2016: Intensification of convective extremes driven by cloud–cloud interaction. *Nat. Geosci.*, **9**, 748–752, https://doi.org/10.1038/ngeo2789.

Nair, U. S., M. R. Hjelmfelt, and Pielke R. A. Sr., 1997*:* Numerical simulation of the 9–10 June 1972 Black Hills Storm using CSU RAMS. *Mon. Wea. Rev.*, ***125***, 1753–1766.

Naka, N., & Takemi, T. (2023). Characteristics of the environmental conditions for the occurrence of recent extreme rainfall events in northern Kyushu, Japan. *Scientific Online Letters on the Atmosphere*, **19A**(Special_Edition), 9–19.

NCAR/EOL S-Pol Team. 2023. PRECIP: NCAR S-Pol radar moments data. Version 1.0. [Dataset] UCAR/NCAR - Earth Observing Laboratory. https://doi.org/10.26023/QA4M-CDHH-MY0Z. Accessed 12 Aug 2024.

Parsons, D. B., J.-L. Redelsperger, and K. Yoneyama, 2000: The evolution of the tropical western Pacific atmosphere-ocean system following the arrival of a dry intrusion. *Q.J.R. Meteorol. Soc.*, **126**, 517–548, doi:10.1002/qj.49712656307

Pauley, P. M., and X. Wu, 1990: The Theoretical, Discrete, and Actual Response of the Barnes Objective Analysis Scheme for One- and Two-Dimensional Fields. *Mon. Wea. Rev.*, **118**, 1145–1164.

doi:10.6342/NTU202504233

Picca, J., and A. Ryzhkov, 2012: A dual-wavelength polarimetric analysis of the 16 May 2010 Oklahoma city extreme hailstorm. *Mon. Wea. Rev.*, **140**, 1385–1403, https://doi.org/10.1175/MWR-D-11-00112.1.

PRECIP, 2022: Prediction of rainfall extremes campaign in the Pacific. Accessed 21 July 2024, http://precip.org/.

Rasmussen, K. L., and R. A. Houze Jr., 2011: Orogenic convection in subtropical South America as seen by the TRMM satellite. *Mon. Wea. Rev.*, **139**, 2399–2420.

Rasmussen, K. L., and R. A. Houze Jr., 2012: A flash flooding storm at the steep edge of high terrain: Disaster in the Himalayas. *Bull. Amer. Meteor. Soc.*, ***93***, 1713–1724, doi:10.1175/BAMS-D-11-00236.1.

Rasmussen, K. L., and R. A. Houze, 2016: Convective Initiation near the Andes in Subtropical South America. *Mon. Wea. Rev.*, **144**, 2351–2374.

Raymond, D. J., and A. M. Blyth, 1986: A stochastic mixing model for nonprecipitating cumulus clouds. *J. Atmos. Sci.*, **43 ,** 2708–2718.

Richardson, Y. P., K. K. Droegemeier, and R. P. Davies-Jones, 2007: The influence of horizontal environmental variability on numerically simulated convective storms. Part I: Variations in vertical shear, *Mon. Wea. Rev.,* **135,** 3429–3455.

Rocque, M. N., and K. L. Rasmussen, 2022: The Impact of Topography on the Environment and Life Cycle of Weakly and Strongly Forced MCSs during RELAMPAGO. *Mon. Wea. Rev.*, **150**, 2317–2338.

Rolph, G., A. Stein, and B. Stunder, 2017: Real-time environmental applications and display system: READY. *Environmental Modelling & Software*, **95**, 210–228, https://doi.org/10.1016/j.envsoft.2017.06.025

doi:10.6342/NTU202504233

Romatschke, U., and R. A. Houze Jr., 2010: Extreme summer convection in South America. *J. Climate*, ***23***, 3761–3791, doi:10.1175/2010JCLI3465.1.

Rotunno, R., J. B. Klemp, and M. L. Weisman, 1988: A theory for strong, long-lived squall line. *J. Atmos. Sci.*, **45**, 463–485.

Ryzhkov, A. V., and D. S. Zrnic, 2007: Depolarization in ice crystals and its effect on radar polarimetric measurements. *J. Atmos. Ocean. Tech.*, **24**, 1256–1267.

Ryzhkov, A. V., and D. S. Zrnić, 2019: *Radar Polarimetry for Weather Observations*. 1st ed. Springer, 486 pp.

Schumacher, R. S., and J. M. Peters, 2017: Near-surface thermodynamic sensitivities in simulated extreme-rain-producing mesoscale convective systems, *Mon. Wea. Rev.*, **145**, 2177–2200.

Schumacher, R. S., and R. H. Johnson, 2008: Mesoscale Processes Contributing to Extreme Rainfall in a Midlatitude Warm-Season Flash Flood. *Mon. Wea. Rev.*, **136**, 3964–3986, https://doi.org/10.1175/2008MWR2471.1.

Segall, J. H., M. M. French, D. M. Kingfield, S. D. Loeffler, and M. R. Kumjian, 2022: Storm-Scale Polarimetric Radar Signatures Associated with Tornado Dissipation in Supercells. *Wea. Forecasting*, **37**, 3–21, https://doi.org/10.1175/WAF-D-21-0067.1.

Shusse, Y., and K. Tsuboki, 2006: Dimension characteristics and precipitation efficiency of cumulonimbus clouds in the region far south from the mei-yu front over the eastern Asian continent. *Mon. Wea. Rev.*, **134**, 1942–1953.

Skamarock, W. C., J. B. Klemp, J. Dudhia, D. O. Gill, D. M. Barker, M. G. Duda, X.-Y. Huang, W. Wang, and J. G. Powers, 2008: A description of the Advanced Research WRF version 3. *NCAR Tech. Note* NCAR/TN-4751STR, 113 pp.

doi:10.6342/NTU202504233

Skamarock, W. C., Klemp, J. B., Dudhia, J., Gill, D. O., Liu, Z., Berner, J., et al. (2019). A description of the advanced research WRF model version 4. NCAR Technical Note NCAR/TN-556+STR.145.

Snyder, J. C., A. V. Ryzhkov, M. R. Kumjian, A. Khain, and J. C. Picca, 2015: A *Z*DR column detection algorithm to examine convective storm updrafts. *Wea. Forecasting*, **30**, 1819–1844, doi:10.1175/WAF-D-15-0068.1.

Stalker, J. R., and K. R. Knupp, 2003: Cell merger potential in multicell thunderstorms of weakly sheared environments: Cell separation distance versus planetary boundary layer depth. *Mon. Wea. Rev.*, **131**, 1678–1695.

Stein, A. F., R. R. Draxler, G. D. Rolph, B. J. B. Stunder, M. D. Cohen, and F. Ngan, 2015: NOAA's HYSPLIT atmospheric transport and dispersion modeling system, *Bull. Amer. Meteor. Soc.*, **96,** 2059–2077, http://dx.doi.org/10.1175/BAMS-D-14-00110.1

TAHOPE, 2022: Taiwan-area heavy rain observation and prediction experiment. Accessed 21 July 2024, https://rain.as.ntu.edu.tw/TAHOPE/TAHOPE-home.html.

Takemi, T., & Unuma, T. (2020). Environmental factors for the development of heavy rainfall in the eastern part of Japan during Typhoon Hagibis (2019). *SOLA*, **16**, 30–36.

Takemi, T., O. Hirayama, and C. Liu, 2004: Factors responsible for the vertical development of tropical oceanic cumulus convection, *Geophys. Res. Lett.*, **31**, L11109, doi:10.1029/2004GL020225.

Tam, F. I.-H., M.-J. Yang, and W.-C. Lee, 2022: Polarimetric size sorting signatures in the convective regions of mesoscale convective systems in PECAN: Implications on kinematics, thermodynamics, and precipitation pathways. *J.*

doi:10.6342/NTU202504233

Geophys. Res. Atmos., **127**, e2021JD035822. https://doi.org/10.1029/2021JD035822

Tao, W.-K., and J. Simpson, 1989: A further study of cumulus interactions and mergers: Three-dimensional simulations with trajectory analyses. *J. Atmos. Sci.*, **46**, 2974–3004.

tobac Community, Brunner, K., Freeman, S. W., Jones, W. K., Kukulies, J., Senf, F., Bruning, E., Stier, P., van den Heever, S. C., Heikenfeld, M., Marinescu, P. J., Collis, S. M., Lettl, K., Pfeifer, N., Raut, B. A., Zhang, X., and Sokolowsky, G. A., 2023: tobac – Tracking and Object-based Analysis of Clouds. [Software] Zenodo. https://doi.org/10.5281/zenodo.8164675.

Tompkins, A. M., 2001: Organization of tropical convection in low vertical wind shears: The role of cold pools. *J. Atmos. Sci.*, **58**, 1650–1672.

T-PARCII, 2022: Tropical cyclones-Pacific Asian research campaign for Improvement of intensity estimations/forecasts. Accessed 21 July 2024, http://rain.hyarc.nagoya-u.ac.jp/~tsuboki/kibanS2/index_kibanS_eng.html.

Tsuji, H., Takayabu, Y. N., Shibuya, R., Kamahori, H., & Yokoyama, C. (2021). The role of free-tropospheric moisture convergence for summertime heavy rainfall in western Japan. *Geophysical Research Letters*, 48, e2021GL095030.

Tsujino, S., H.-C. Kuo, H. Yu, B.-F. Chen, and K. Tsuboki, 2021: Effects of mid-level moisture and environmental flow on the development of afternoon thunderstorms in Taipei. Terr. Atmos. Ocean. Sci., 32, 497-518.

Tuttle, J. D., V. N. Bringi, H. D. Orville, and F. J. Kopp, 1989: Multiparameter radar study of a microburst: Comparison with model results. *J. Atmos. Sci.*, **46**, 601–620.

doi:10.6342/NTU202504233

Van Den Broeke, M. S., 2017: Polarimetric Radar Metrics Related to Tornado Life Cycles and Intensity in Supercell Storms. *Mon. Wea. Rev.*, **145**, 3671–3686, https://doi.org/10.1175/MWR-D-16-0453.1.

Van Den Broeke, M. S., 2020: A preliminary polarimetric radar comparison of pretornadic and nontornadic supercell storms. *Mon. Wea. Rev.*, **148**, 1567–1584, https://doi.org/10.1175/MWR-D-19-0296.1.

Vivekanandan, J., S. M. Ellis, R. Oye, D. S. Zrnic, A. V. Ryzhkov, and J. Straka, 1999: Cloud microphysics retrieval using S-band dual-polarization radar measurements. *Bull. Amer. Meteor. Soc.*, **80**, 381–388.

Wang, S., and A. H. Sobel, 2017: Factors controlling rain on small tropical islands: Diurnal cycle, large-scale wind speed, and topography. *J. Atmos. Sci.*, **74**, 3515–3532.

Westcott, N., 1984: A historical perspective on cloud mergers. Bull. Amer. Meteor. Soc., 65, 219-226.

Wilson, M. B., and M. S. Van Den Broeke, 2021: Using the Supercell Polarimetric Observation Research Kit (SPORK) to examine a large sample of pretornadic and nontornadic supercells. Electronic J. Severe Storms Meteor., 17(2), 1–38.

Wu, Y.-J., Y.-C. Liou, Y.-C. Liou, S.-L. Tai, S.-F. Chang, and J. Sun, 2021: Precipitation processes of a thunderstorm occurred on 19 August 2014 in northern Taiwan documented by using a high resolution 4DVar data assimilation system. *J. Meteor. Soc. Japan*, **99**, 1023–1044.

Xu, W., E. J. Zipser, Y. Chen, C. Liu, Y. Liou, W. Lee, and B. J.-D. Jou, 2012: An orography-associated extreme rainfall event during TiMREX: Initiation, storm evolution, and maintenance. *Mon. Wea. Rev.*, **140**, 2555–2574, https://doi.org/10.1175/MWR-D-11-00208.1.

doi:10.6342/NTU202504233

Yang, M.-J., and R. A. Houze, Jr., 1995: Sensitivity of squall-line rear inflow to ice microphysics and environmental humidity. *Mon. Wea. Rev.*, **123**, 3175–3193.

Yang, S., Y. Chang, H. Cheng, K. Lin, Y. Tsai, J. Hong, and Y. Li, 2024: Improving afternoon thunderstorm prediction over complex terrain with the assimilation of dense ground-based observations: Four cases in the Taipei basin. *Wea. Forecasting*, **39**, 541–561, https://doi.org/10.1175/WAF-D-23-0149.1.

Yu, S., Y. Luo, C. Wu, D. Zheng, X. Liu, and W. Xu, 2022: Convective and microphysical characteristics of extreme precipitation revealed by multisource observations over the Pearl River Delta at monsoon coast. *Geophys. Res. Lett.*, **49**, e2021GL097043. https://doi.org/10.1029/2021GL097043

Yuter, S. E., and R. A. Houze Jr., 1995: Three-dimensional kinematic and microphysical evolution of Florida cumulonimbus. Part II: Frequency distributions of vertical velocity, reflectivity, and differential reflectivity. *Mon. Wea. Rev.*, **123**, 1941–1963.

Zhang, M., K. L. Rasmussen, Z. Meng, and Y. Huang, 2022: Impacts of Coastal Terrain on Warm-Sector Heavy-Rain-Producing MCSs in Southern China. *Mon. Wea. Rev.*, **150**, 603–624.

Zou, X., Cordeira, J. M., Bartlett, S. M., Kawzenuk, B., Roj, S., Castellano, C., et al. (2023). Mesoscale and synoptic scale analysis of narrow cold frontal rainband during a landfalling atmospheric river in California during January 2021. *Journal of Geophysical Research: Atmospheres*, **128**, e2023JD039426. **https://doi.org/10.1029/2023JD039426**.

doi:10.6342/NTU202504233

APPENDIX Additional cases of ATS: 23/24 June 2022

This supplementary section presents two additional cases of severe afternoon thunderstorms (ATSs) during the TAHOPE/PRECIP field campaign. These cases provide further evidence of the evolution of ZDR columns and their broadening during MCM. The findings support the value of ZDR column width as a diagnostic metric for severe convective storms in Taiwan.

The analysis of both cases indicates a consistent convective evolution, highlighting the role of multiple cell merger (MCM) in storm intensification. In each event, individual convective cells merged, leading to the formation of a more extensive convective system (Figs. A1 and A5). This process coincided with the merging of individual ZDR columns (Figs. A2 and A6). Following the MCM, there was a notable increase in graupel and hail within the storm (Figs. A3 and A7). The enhanced presence of these ice-phase particles further supports the hypothesis that the merged ZDR columns may serve as a potential indicator of storm intensification. Time series analysis (Figs. A4 and A8) across both cases reveals that a wide (>8 km) enhanced ZDR region at 5.5 km AMSL coincided with the occurrence of the MCM. Afterward, the observed maximum vertical velocity increased significantly.

Rainfall time series (Fig. A9) across the three cases indicated the link between MCM and precipitation enhancement. A substantial increase in 10-minute rainfall accumulation followed the MCM and wide (>8 km) enhanced ZDR region, with peak precipitation occurring ~30–45 minutes later. The maximum rainfall intensity exceeded 140 mm/h, with the 23 June case reaching ~200 mm/h.

doi:10.6342/NTU202504233

These findings suggest that MCM, along with the broadening of enhanced ZDR region (>8 km), tends to precede intense updrafts and heavy rainfall. The consistency of these findings with IOP 2 study suggests that wide, merged ZDR columns may be relevant to severe storms over complex terrain in Taiwan, highlighting their potential utility as indicators of convective organization.

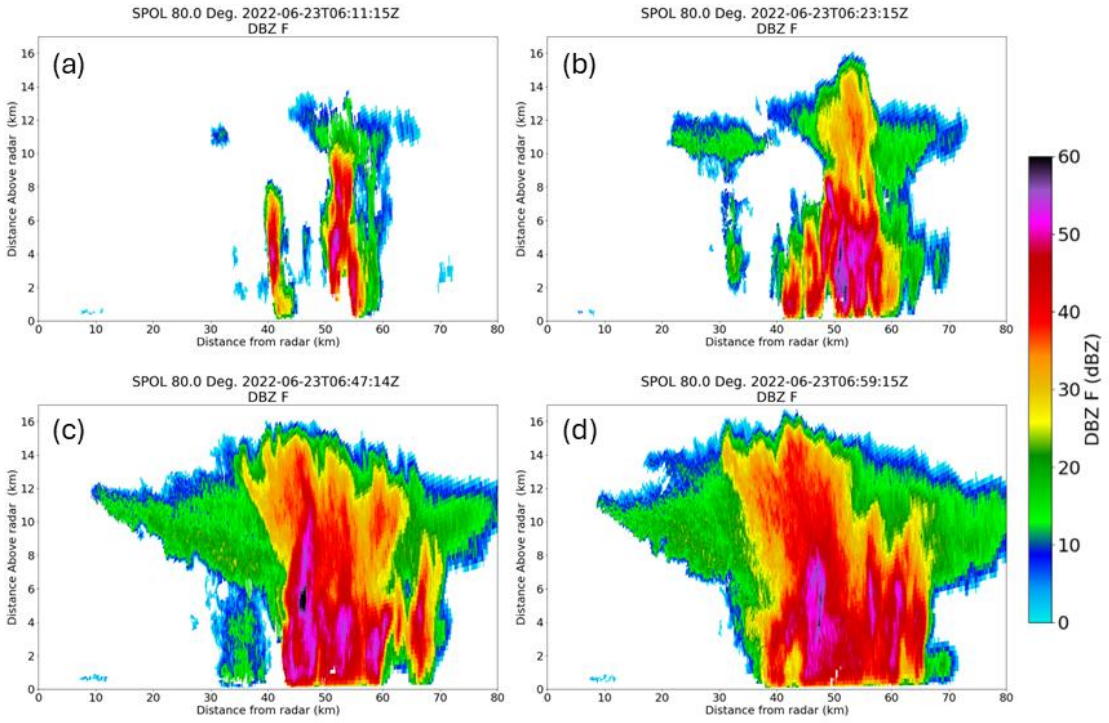

Figure A1. S-Pol range height indicator (azimuth angle 80°) of ZH on 23 June 2022: (a) 1411, (b) 1423, (c) 1447, and (d) 1459 LST.

doi:10.6342/NTU202504233

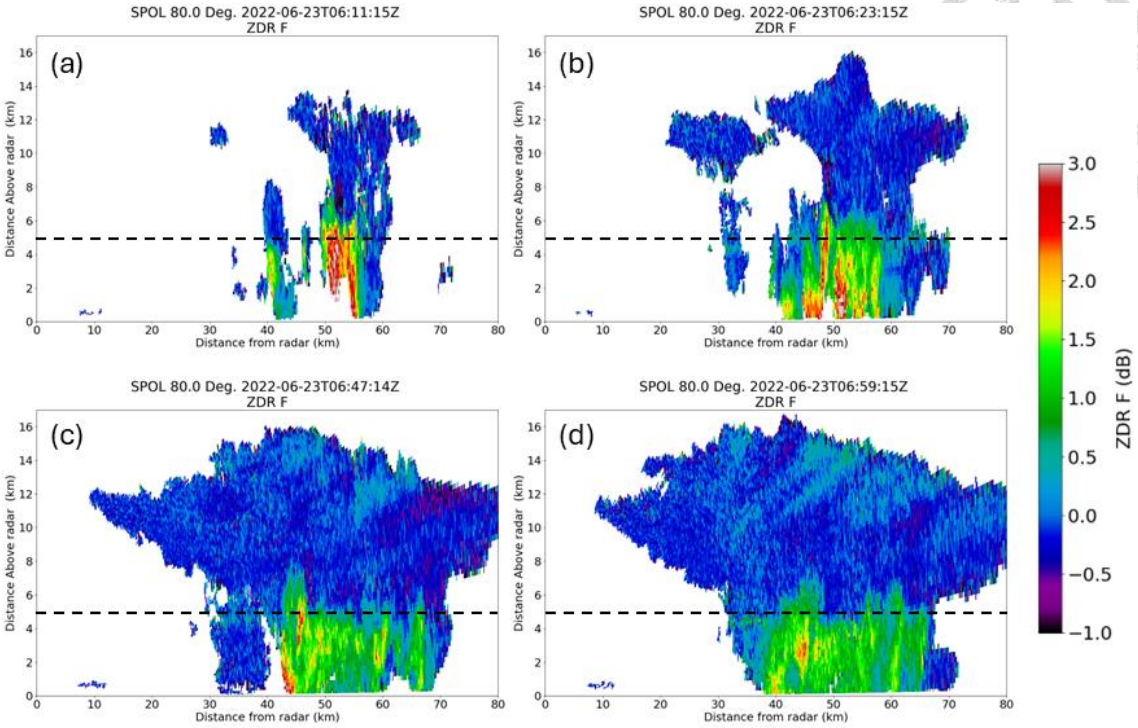

Figure A2. As Fig. A1, but for ZDR.

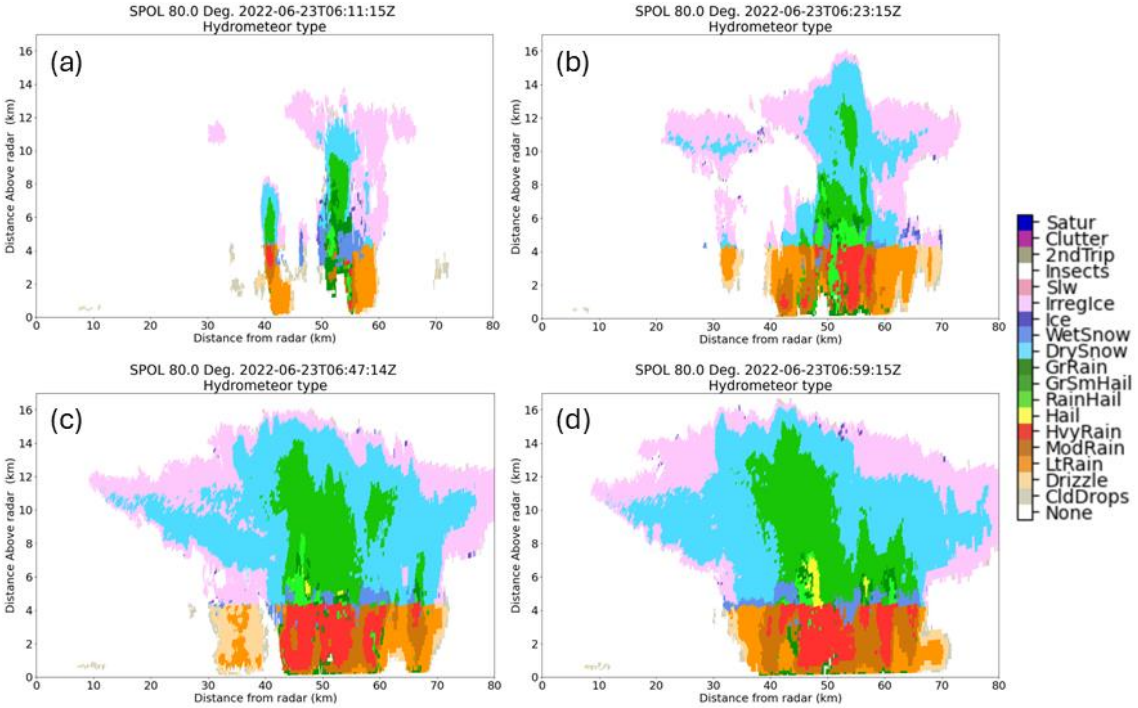

Figure A3. As Fig. A1, but for PID.

doi:10.6342/NTU202504233

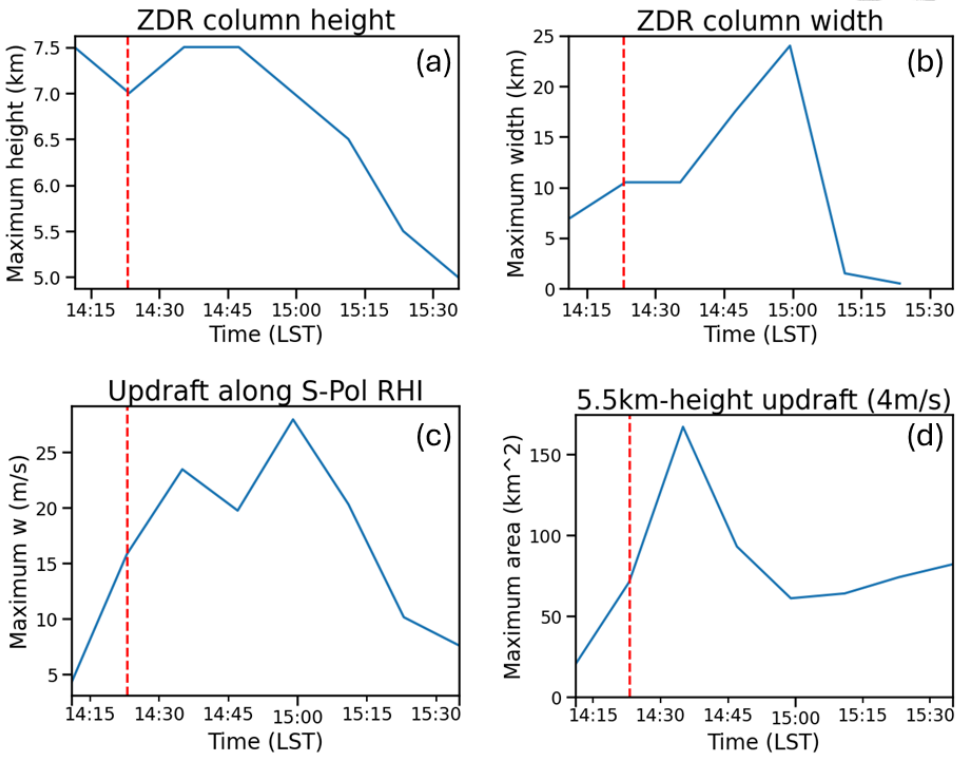

Figure A4. Evolution during 23 June case: (a) maximum height and (b) maximum width of the ZDR columns along the S-Pol 80° RHI. (c) maximum retrieved vertical velocity w of the updrafts along the S-Pol 80° RHI. (d) The maximum connected area of updrafts (w > 4 m/s) which is calculated at the 5.5 km AMSL. The maximum width of ZDR columns is calculated at the 5.5 km AMSL. The time of multiple cell merger is labeled as the red dashed lines.

doi:10.6342/NTU202504233

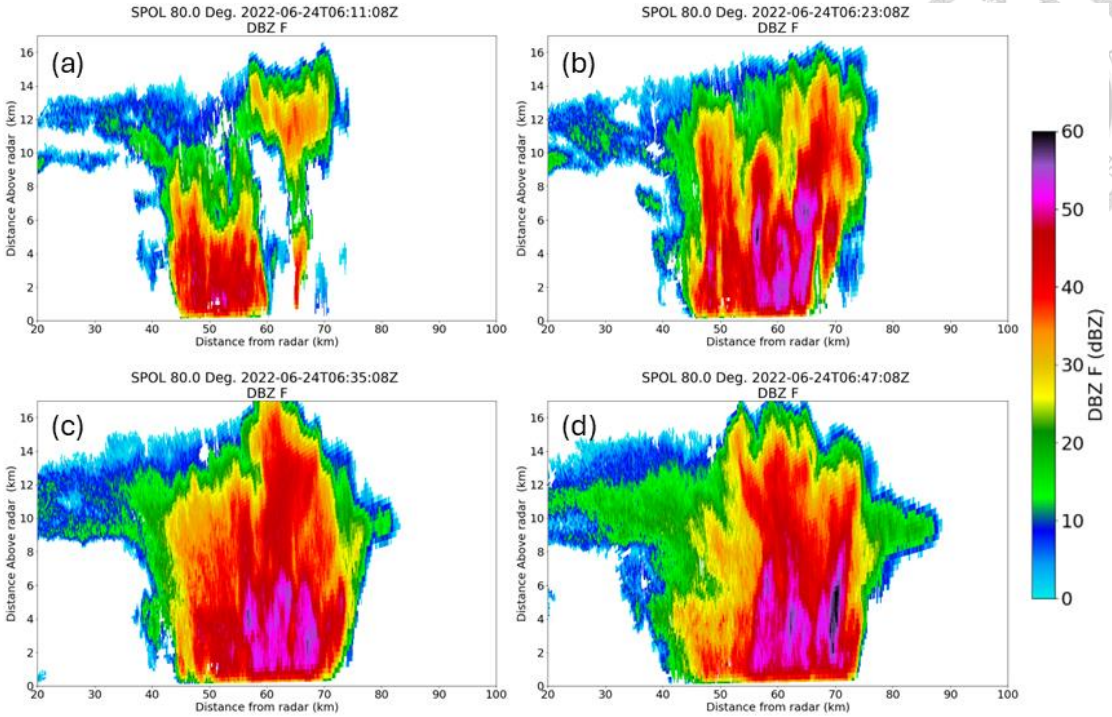

Figure A5. S-Pol range height indicator (azimuth angle 80°) of ZH on 24 June 2022: (a) 1411, (b) 1423, (c) 1435, and (d) 1447 LST.

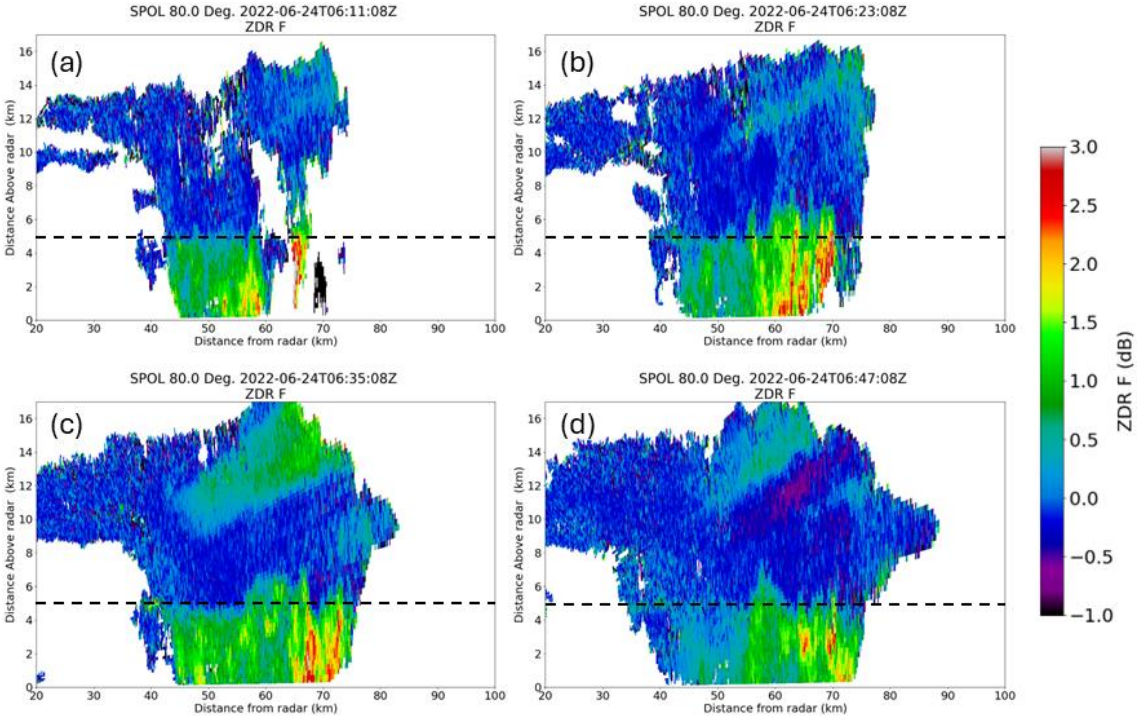

Figure A6. As Fig. A5 but for ZDR.

doi:10.6342/NTU202504233

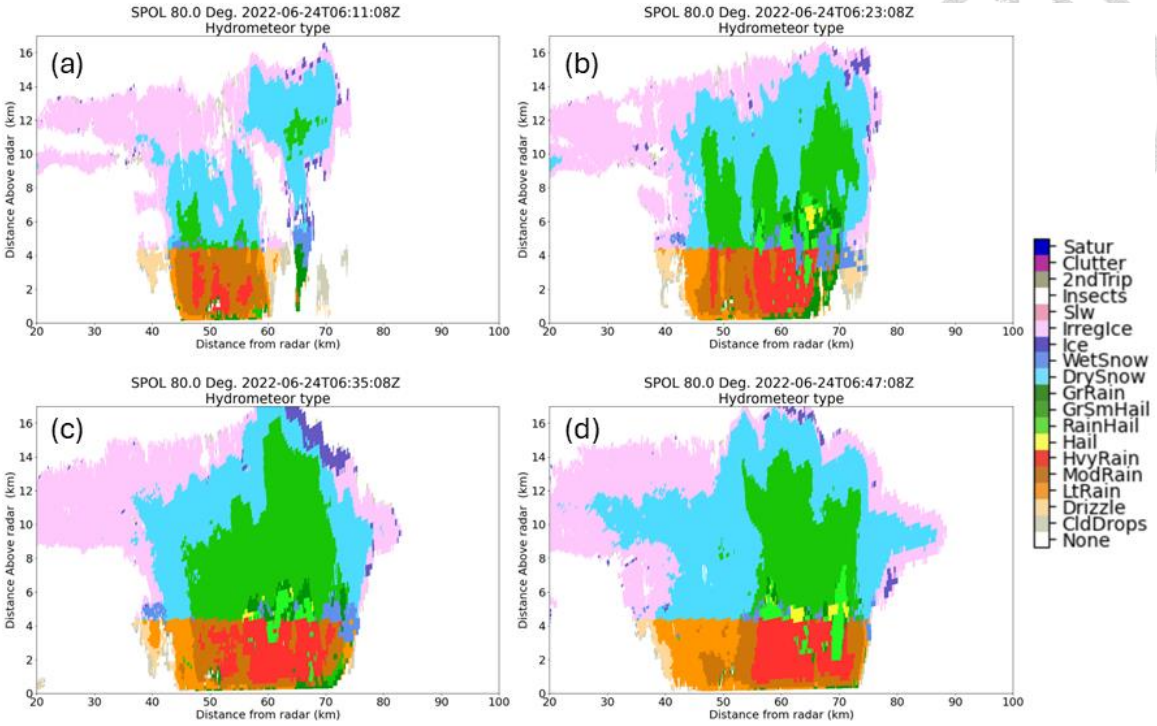

Figure A7. As Fig. A5, but for PID.

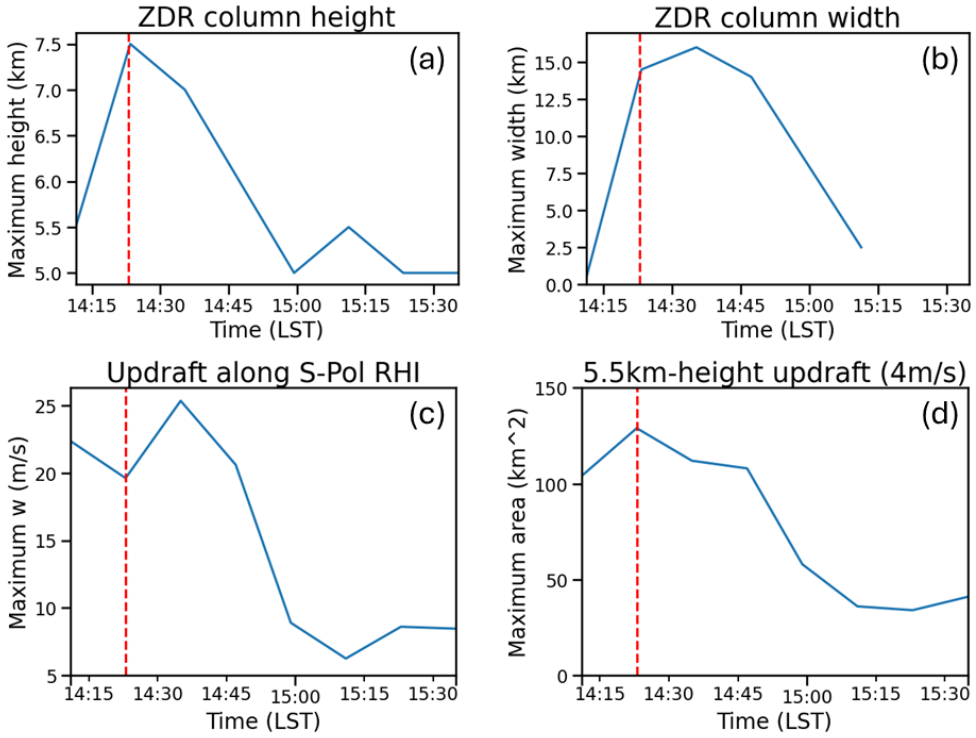

Figure A8. As Fig. A4, but for 24 June case.

doi:10.6342/NTU202504233

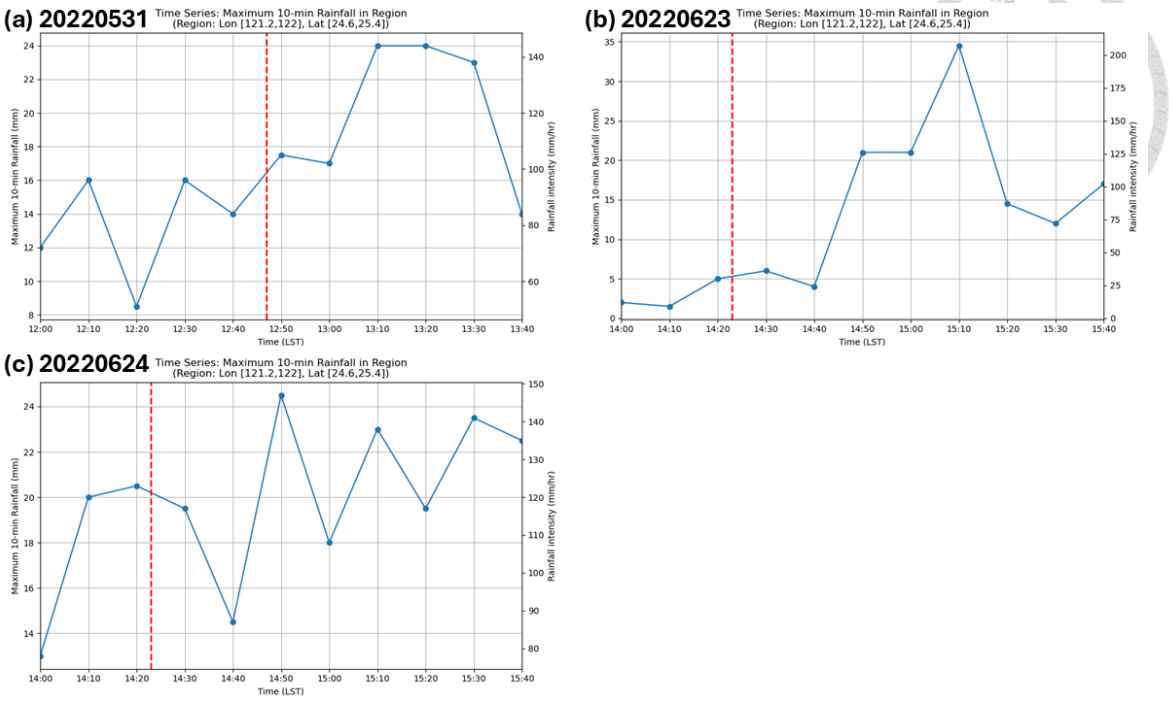

Figure A9. Time series of the maximum 10-minute accumulated rainfall (mm) in the study region for the three analyzed cases: (a) 31 May 2022, (b) 23 June 2022, and (c) 24 June 2022. The red dashed line indicates the time of the MCM in each case.

doi:10.6342/NTU202504233